UNIVERSITÀ DEGLI STUDI DI PADOVA

DIPARTIMENTO DI INGEGNERIA INDUSTRIALE DII
CORSO DI LAUREA MAGISTRALE IN INGEGNERIA DELL'ENERGIA ELETTRICA

TESI DI LAUREA MAGISTRALE

Transient model of an automotive multiphase induction machine with phase and pole changing capability

Relatore: Prof. Silverio Bolognani

Supervisor: Prof. Oskar Wallmark
KTH - Royal Institute of Technology, Stockholm, Sweden

Laureando: Andrea Pisani
1179279

ANNO ACCADEMICO: 2019-20

ABSTRACT

This thesis presents the derivation of two transient models of a multiphase induction motor for automotive purposes. The motor under analysis is a *Gramme type* winding based on the German patent of Intelligent Stator Cage Drive (ISCAD) machine, whose peculiar aspect is the possibility to operate a dynamic change of poles and phases maintaining relatively low currents. Two models are described; the first is based on analytical considerations about the electromagnetic and algebraic nature of the problem. The second focuses on the extraction of lumped information from a Finite Element (FE) analysis of the machine. The result of both models is the derivation of parameters through which a system of ordinary differential equations is set up in order to predict electrical and mechanical quantities of the motor. Both methods are compared to independent FE simulations and parameters are verified in their capability to predict magnetic fluxes. Ultimately, models are compared to a FE reference in terms of electrical and mechanical results for different supplying configurations and pole transitions.

CONTENTS

1 INTRODUCTION 1
  1.1 Background 1
  1.2 Thesis structure 4
2 WICSC MACHINE 7
  2.1 Geometry 8
  2.2 Materials 9
  2.3 Set-up configuration 11

I TRANSIENT MODEL ANALYTICAL DERIVATION

3 INTRODUCTION 15
  3.1 Method overview 15
  3.2 Parameters' nature 16
4 RESISTANCE DERIVATION 19
  4.1 Stator coil resistance 19
  4.2 Rotor bar resistance 19
5 STATOR FLUX LINKAGE DUE TO STATOR CURRENTS: L_s 23
  5.1 Air-gap magnetic field induced by stator currents 23
  5.2 Magnetic flux linked to stator coils 26
    5.2.1 Relation between air-gap magnetic flux and stator currents 26
    5.2.2 Relation between air-gap magnetic flux and flux in the stator yoke 26
    5.2.3 Relation between currents and flux in the stator yoke: L_s 27
6 ROTOR FLUX LINKAGE DUE TO ROTOR CURRENT: L_r 29
  6.1 Air-gap magnetic field induced by rotor currents 29
  6.2 Magnetic flux linked by rotor bars 30
    6.2.1 Relation between air-gap magnetic flux and stator currents 30
    6.2.2 Relation between air-gap and rotor lamination magnetic flux 30
    6.2.3 Relation between currents and flux in the stator yoke: L_s 32
7 CONNECTION BETWEEN ROTOR AND STATOR: MUTUAL MATRICES 33
  7.1 Stator flux linkage due to rotor currents: $L_{mut,s-r}(\theta_r)$ 33
    7.1.1 Introduction 33
    7.1.2 Derivation 34
    7.1.3 Air-gap flux derivation 36
  7.2 Rotor flux linkage due to stator currents: $L_{mut,r-s}(\theta_r)$ 37
8 TRANSIENT MODEL 39
  8.1 Mutual matrices derivative 39

8.2 Matrix model 42

II ANALYTICAL MODEL DERIVED FROM FINITE ELEMENT ANALYSIS

9 PARAMETER DERIVATION BY FINITE ELEMENT ANALYSIS 47
9.1 Finite Element model 47
9.1.1 Model description 47
9.2 Stator flux linkage due to stator current: L_s 49
9.2.1 Quantities definition 49
9.2.2 L_s computation 50
9.2.3 Results 51
9.3 Rotor flux linkage due to rotor current: L_r 52
9.3.1 Quantities definition 52
9.3.2 L_r computation 52
9.3.3 Results 53
9.4 Stator flux linkage due to rotor current: L_{sr} 54
9.5 Rotor flux linkage due to stator current: L_{rs} 57
10 TRANSIENT MODEL 59
10.1 Matrix derivative 59
10.2 FEA equation 60

III VALIDATION OF ANALYTICAL METHOD

11 METHODS COMPARISON FOR MATRIX DERIVATION 63
11.1 Stator self connection: L_s 63
11.2 Rotor self connection: L_r 63
11.3 Mutual connection rotor flux due to stator currents: L_{rs} 65
11.3.1 Two-coils supplying configuration 69
11.3.2 Two-poles supplying configuration 70
11.4 Mutual connection stator flux due to rotor currents: L_{sr} 71
11.4.1 Two-coils supplying configuration 73
11.4.2 Two-poles supplying configuration 74
12 ELECTRICAL AND MECHANICAL VALIDATION OF TRANSIENT MODELS 77
12.1 Electrical derivation 77
12.2 Mechanical torque 77
12.3 Simulations 78
12.3.1 Linear materials 79
12.3.2 Pole transition 80
12.3.3 Non-linear materials 89
12.4 Conclusions 92

Appendix

A NUMERICAL DERIVATIVE 95
B AIR-GAP TO YOKE FLUX RELATION 97

B.1 Equivalent electrical circuit method 97
B.2 Netlist 98
B.3 Tableau analysis 98
B.4 At-the-limit solution 99
B.5 Graph-theory-based approach 101
  B.5.1 Equivalent simplified circuit graph 101
B.6 The pseudo-inverse 103

BIBLIOGRAPHY 107

LIST OF FIGURES

Figure 2.1 Rendering of the Wound Independently-Controlled Stator Coil (WICSC) machine without the rotor. 7

Figure 2.2 Complete 2D representation of the machine. 9

Figure 2.3 Schematic representation of the set-up. 11

Figure 4.1 Comparison between equivalent rotor bar resistance for different number of poles. 21

Figure 5.1 Machine configuration with $Q_s = 4$. 23

Figure 5.2 Line integral paths considered, machine configuration with $Q_s = 4$. 24

Figure 6.1 Rotor configuration with $Q_s = 4$. 29

Figure 6.2 Schematic representation of air-gap and rotor bar fluxes. 31

Figure 7.1 Rotor configuration with $Q_s = 4$. 33

Figure 7.2 Rotor configuration with $Q_s = 4$. 34

Figure 7.3 Two scenarios for the relative position of rotor bars and stator coils. 36

Figure 8.1 Connection between current in stator coil 1 and flux in rotor bar 1 over rotor position. 40

Figure 8.2 Connection between stator coil 1 current and rotor bar 15 flux over rotor position, and its angular derivative. 41

Figure 8.3 Comparison between Fourier's series expansion and Gauss-filtering of $L_{rs_{1,1}}$ and its time-derivative. 41

Figure 9.1 Detail of the rotor bar with the artificial opening and the stator slot. 49

Figure 9.2 Elements to consider for the flux linkage. 50

Figure 9.3 Stator slots flux linkages induced by current in stator coil 1. 51

Figure 9.4 A_z contour lines induced by current in stator slot 1. 52

Figure 9.5 Rotor bars flux linkages induced by current in rotor bar 1. 54

Figure 9.6 A_z contour lines induced by current in rotor bar 1. 55

Figure 9.7 $L_{sr_{1,1}}$ versus θ_r. 56

Figure 9.8 $L_{rs_{1,1}}$ versus θ_r. 57

Figure 10.1 Connection between rotor bar 15 and stator coil 1, its derivative and Gauss'filtering of the derivative. 60

Figure 11.1 Comparison of different methods in terms of stator coil flux linkage predictions. 64
Figure 11.2 Comparison of different methods in terms of rotor bar flux linkage predictions. 66
Figure 11.3 Smooth step function. 67
Figure 11.4 Rotor bar 1 magnetic flux linkage comparison for different methods. Below a smaller time window is set to appreciate differences. 68
Figure 11.5 Rotor bar 1 induced voltages comparison for different methods. Below a smaller time window is set to appreciate differences. 69
Figure 11.6 Rotor bar 1 induced magnetic fluxes comparison for different methods. Below a smaller time window is set to appreciate differences. 70
Figure 11.7 Rotor bar 1 induced voltages comparison for different methods, sinusoidally spaced currents. Below a smaller time window is set to appreciate differences. 71
Figure 11.8 Stator coil 1 magnetic flux linkage comparison for different methods. Below a smaller time window is set to appreciate differences. 72
Figure 11.9 Stator coil 1 voltage comparison for different methods. Below a smaller time window is set to appreciate differences. 73
Figure 11.10 Stator coil 1 magnetic flux linkage comparison for different methods. Below a smaller time window is set to appreciate differences. Sinusoidal case. 74
Figure 11.11 Stator coil 1 voltage comparison for different methods. Below a smaller time window is set to appreciate differences. Sinusoidal case. 75
Figure 12.1 Electrical and mechanical comparison of models, linear materials, 2-poles, $s = 100\,\%$. 81
Figure 12.2 Electrical and mechanical comparison of models, linear materials, 2-poles, $s = 0\,\%$. 82
Figure 12.3 Electrical and mechanical comparison of models, linear materials, 2-poles, $s = 25\,\%$. 83
Figure 12.4 Electrical and mechanical comparison of models, linear materials, 2-poles, $s = 2.5\,\%$. 84
Figure 12.5 Electrical and mechanical comparison of models, linear materials, 4-poles, $s = 2.5\,\%$. 85
Figure 12.6 Electrical and mechanical comparison of models, linear materials, 12-poles, $s = 2.5\,\%$. 86
Figure 12.7 Electrical and mechanical comparison of models, linear materials, pole transition, $s = 2.5\,\%$. 87

Figure 12.8 Electrical and mechanical comparison of models, linear materials, pole transition $s = 2.5\,\%$. 88
Figure 12.9 $B-H$ curve of lamination material used for non-linear simulations. 89
Figure 12.10 Electrical and mechanical comparison of models, non-linear materials, $s = 25\,\%$. 90
Figure 12.11 Electrical and mechanical comparison of models, non-linear materials, $s = 2.5\,\%$. 91
Figure B.1 Equivalent circuit for $Q_s = 4$. 98
Figure B.2 Equivalent simplified circuit graph for $Q_s = 4$. 101

LIST OF TABLES

Table 2.1 Main aspects of the WICSC machine. 10
Table 2.2 Assumed material properties of WICSC machine FE model. 10
Table B.1 Netlist of the equivalent circuit. 99

ACRONYMS

NASA	National Aeronautics and Space Administration
NOAA	National Oceanic and Atmospheric Administration
EV	Electric Vehicle
BEV	Battery Electric Vehicle
IM	Induction Motor
SM	Synchronous Motor
SRM	Switch Reluctance Motor
PMSM	Permanent-Magnet Synchronous Motor
IPM	Interior Permanent Magnet
SynRM	Synchronous Reluctance Motor
PMAREL	Synchronous Permanent-Magnet Assisted Reluctance Motor
HV	High Voltage
ISCAD	Intelligent Stator Cage Drive
FE	Finite Element

FEM Finite Element Method

WICSC Wound Independently-Controlled Stator Coil

FEA Finite Element Analysis

ADC Analog Digital Converter

FMC FPGA Mezzanine Card

FPGA Field Programmable Gate Array

DAE Differential Algebraic Equation

ODE Ordinary Differential Equation

KCL Kirchhoff Current Law

KVL Kirchhoff Voltage Law

NOMENCLATURE

$\mathbf{B}_\delta$	Air-gap magnetic flux density vector	$\mathrm{A\,m^{-1}}$
α_{sk}	Rotor skew angle	rad
α_{Cu}	Copper temperature coefficient	$\mathrm{K^{-1}}$
δ	Air-gap length	m
μ_r	Relative permeability	-
ω_m	Rotor mechanical speed	$\mathrm{rad\,s^{-1}}$
ρ	Electric charge density	$\mathrm{C\,m^{-3}}$
ρ_{Al}	Alumimum resistivity	$\Omega\,\mathrm{m}$
$\rho_{\mathrm{Cu},x^\circ\mathrm{C}}$	Copper resistivity at x°C	$\Omega\,\mathrm{m}$
σ	Electrical conductivity	$\mathrm{S\,m^{-1}}$
τ_{r2}	Rotor tooth pitch in the middle of the air-gap	m
θ_r	First rotor bar position with respect to the stator	rad
$\theta_r^{'}$	Coordinate system integral with the rotor	rad
θ_{rb_k}	Position of rotor bar k-th	rad
θ_{sc_j}	Position of stator coil j-th	rad
θ_m	Coordinate system integral with the stator	rad
θ_{r0}	Initial relative position of the first rotor with respect to the first stator coil	rad
$\Phi_{\delta,j}$	Magnetic flux in the air-gap for coil/bar j	$\mathrm{V\,m}$

Φ_j	Magnetic flux in the stator yoke/rotor lamination for coil/bar j	$\mathrm{V\,m}$
$\boldsymbol{\Psi}_\mathbf{r}$	Rotor bar flux linkage	$\mathrm{V\,s}$
$\boldsymbol{\Psi}_\mathbf{s}$	Stator coil flux linkage vector	$\mathrm{V\,s}$
$\boldsymbol{\Theta}_\mathbf{rs}$	Angular connection between air-gap magnetic field density due to stator current and air-gap magnetic flux	rad
$\boldsymbol{\Theta}_\mathbf{sr}$	Angular connection between air-gap magnetic field density due to rotor current and air-gap magnetic flux	rad
$\mathbf{B}$	Magnetic flux density vector field	T
$\mathbf{D}$	Electric displacement vector field	$\mathrm{C\,m^{-2}}$
$\mathbf{E}$	Electric field density vector field	$\mathrm{V\,m^{-1}}$
$\mathbf{H}$	Magnetic field intensity vector field	$\mathrm{A\,m^{-1}}$
$\mathbf{i_r}$	Rotor bar current vector	A
$\mathbf{i_s}$	Stator coil current vector	A
$\mathbf{J}$	Current density vector field	$\mathrm{A\,m^{-2}}$
$\mathbf{L}_r$	Rotor bar self inductance	H
$\mathbf{L}_s$	Stator slot self inductance	H
$\mathbf{L}_{mut,r-s}$	Mutual inductance resulting in rotor flux due to stator current	H
$\mathbf{L}_{mut,s-r}$	Mutual inductance resulting in stator flux due to rotor current	H
$\mathbf{M}_3$	Matrix connection between air-gap and stator yoke/rotor lamination fluxes	
$\mathbf{M}_{i,\mathbf{H}}$	Matrix connection between currents and air-gap magnetic field	$\mathrm{m^{-1}}$
$\mathbf{V_r}$	Rotor bar voltage vectior	V
$\mathbf{V_s}$	Stator coil voltage vector	V
b	Equivalent bar width	m
d	Equivalent bar depth	m
d_{be}	Rotor end-ring depth	m
f_m	Mechanical frequency	Hz

f_s	Synchronous frequency	Hz
f_{slip}	Slip frequency, or rotor electrical frequency	Hz
$H_{\delta,j}$	Air-gap magnetic field between coil/bar j and $j+1$	$A\,m^{-1}$
i_b	Rotor bar current	A
$i_e r$	Rotor end-ring current	A
J_b	Rotor bar current density	$A\,m^{-2}$
J_{er}	End-ring current density	$A\,m^{-2}$
l_1	Rotor bar length considering ducts	m
L_a	Active length	m
l_b	Length of one rotor bar	m
l_{be}	Rotor bar extension on one side	m
L_{hs}	Stator housing length	m
L_{sb}	Stator back length	m
n_s	Number of turns per slot	-
n_{ps}	Stator conductor parallel strands	-
p	Number of poles	-
Q_r	Number of rotor bars	-
Q_s	Number of stator slots	-
R_b	Rotor bar resistance	Ω
R_r	Equivalent rotor bar resistance including two short-circuit ring elements	Ω
r_r	Rotor outer radius	m
R_s	Stator coil resistance	Ω
R_{al}	Stator coil resistance for the active lenght portion	Ω
R_{er}	Rotor end-ring resistance	Ω
R_{ew}	Stator coil resistance for the end winding portion	Ω
r_{shaft}	Shaft radius	m
r_{str}	Stator strand radius	m
R_{turn}	Stator coil resistance per one turn	Ω

$r_{s,in}$	Stator inner radius	m
s	Slip value	-
S_b	Rotor bar cross-sectional area	m^2
S_{cond}	Stator conductor total cross-sectional area	m^2
S_{er}	Rotor end-ring cross-sectional area	A
S_{str}	Strand cross-sectional area	m^2
T_m	Mechanical torque	$N\,m$
t_{be}	Rotor end-ring width	m
W_{co}	Co-energy	$V\,A\,s$
w_{so}	Stator-slot opening width	m

1

INTRODUCTION

1.1 BACKGROUND

According to analyses carried out by National Aeronautics and Space Administration (NASA) and the National Oceanic and Atmospheric Administration (NOAA), the past decade was the hottest decade ever registered and 2019 saw the second warmest global surface temperatures since mankind started to keep records of such data, in 1880 [1, 2].

It is widely recognized that the transport sector plays a primary role in terms of air pollution worldwide, and recently, concerns about local air quality find road traffic exhausts a crucial impacting factor [3–5]. Therefore, modern societies are needed to find effective solutions to well-known problems such as global warming and air pollution.

In this context, the deployment of electric vehicles can be a valid solution to decrease greenhouse-gas emissions, fossil-fuels consumptions as well as local exhaust gases and particulate pollution that have a not negligible impact on living beings' life.

ELECTRIC MOTORS IN THE AUTOMOTIVE SECTOR Focusing on electric mobility, and in particular on Battery Electric Vehicles (BEVs) motors, different solutions are available nowadays. It is possible to enclose such technologies in three macro-categories: Asynchronous Motors or Induction Motors (IMs), Synchronous Motors (SMs) , especially Permanent-Magnet Synchronous Motors (PMSMs) and Switch Reluctance Motors (SRMs) [6].

The SM provide the best performance [6, 7]. In fact, these machines are characterized by the higher torque, torque density, efficiency and the lower weight and size. Among PMSMs, widely used in Electric Vehicle (EV) applications are the Interior Permanent Magnet (IPM) motors which are based on rare-earth permanent magnets embedded in the rotor. Nevertheless, the high cost of such materials, the limited supply and the environmental impact of their extraction make IPM motors not perfectly suitable for large use. Synchronous Reluctance Motors (SynRMs) are therefore becoming more and more appealing in this term, since they allow for no usage of rare-earth metals (or lower in case of Synchronous Permanent-Magnet Assisted Reluctance Motors (PMARELs)), high torque density, high capability of overload and robust construction [6, 7].

SRMs on their side can operate at very high speeds, even though in this operation mechanical losses are high due to aerodynamics drag and viscosity losses [6]. They have a good power density, satisfactory efficiency and low production costs, but the main drawbacks are high torque ripple and acoustic noise, and efforts to reduce such aspects are a trade-off in terms of cost and efficiency.

IMs are widely used in industrial operations mainly because of their ability to start under load without an inverter, which makes them directly compatible with conventional utility power [8].

For what regards their EV application, the main drawback is that high rotor heat is generated, making rotor cooling easier in the PMSMs. Compared to them, IMs have a lower energy efficiency. When it comes to high-performance, IMs may be the choice. In fact, while the strength of the magnetic field produced by permanent magnets cannot be changed easily, it can be achieved in IMs by controlling the V/f ratio. This means that at light loads, magnetic losses are reduced. Furthermore, if in a DC brushless machine magnetic losses grow as machine size grows, the same does not apply for IMs, allowing for a competitive or even better average performance [8]. Ultimately, IMs are less expensive and easier to protect.

MULTI-PHASE MACHINES Recently, multi-phase machines have started to make their appearance as candidates for EV applications.

The term *multi-phase* commonly refers to machines with more than three phases; standard three-phase machines have been universally adopted more than a century ago for their capabilities of starting under load and not producing a twice line-frequency pulsating torque like one or two phases machines. As more and more motors started to be connected to power electronic converters rather than to the direct three-phase supplies, a wide range of possibilities became possible, multi-phase machines with them [9]. Their main advantages are briefly explained below.

- Stator excitation in a multi-phase machine induced magnetic field density in the air-gap with a lower spacial harmonics content, resulting in higher efficiency [9, 10]. In fact, as the number of phases increases, the order of magnetomotive-force spacial harmonics also increases.

- Resulting from the same reasons described in the first point, multi-phase machines have lower torque ripple. Moreover, higher torque density and less acoustic noise contribute to their virtues. Studies proved that it is possible to inject optimal values of third harmonics in order to improve the output torque [11].

- Another important benefit of multi-phase machines is fault tolerance, which in practice finds its expression in quicker fault detection and post-fault operations, thanks to phase redundancy. Therefore, reliability and stability are improved even with not excessive performance degradation [10].

For such features, multi-phase machines have been deployed in applications which require the capability to operate in case of fault and the advantage to perform with large flexibility at low acoustic impact, such as in maritime or aeronautic applications. For instance, two general Electric 20 *MW* 15-phases IMs are adopted to power a Type 45 destroyer, and the new Royal Navy's Queen Elizabeth Class Aircraft Carrier relies on a twin arrangement of the solution adopted in the destroyer.

ISCAD EVs requirements in terms of electrical machines regards various aspects such as high torque density, operation speed, efficiency, low rotor losses and thermal stress.

This is the reason why designers often focus on distributed windings with high number of coils per pole. The main advantage is the achievement of high quality magnetomotive force and air-gap flux density, comporting lower rotor losses, rotor heating and vibrations. On the other hand, such configurations have drawbacks that can not be neglected.

Firstly, they are complex and require high manual work and sophisticated automation systems; this leads to high costs.

Secondly, such windings have a low slotting fill factor (around 0.5) and large end-winding portions which contribute to additional losses.

Thirdly, they have a fixed number of poles for their nature, meaning they rely only on one specific maximum efficiency point and therefore their efficiency decreases under conditions of partial load [12].

Lastly, conventional motors are defined to operate in a voltage range between 300 and 800 V and, since these values are above the protection limit of 60 V, their applications in EVs makes the latter a High Voltage (HV) vehicle. As a consequence, proper safety requirements are necessary.

Dajaku and Gerling recently proposed and patented a novel stator cage winding for electrical machines [13]. The traction drive has been named ISCAD and it introduces concepts that deviate from conventional drives, which will be briefly introduced below.

- The stator consists of conductor bars in each slot, short-circuited at one axial end as it normally happens in a squirrel cage rotor. On the other stator side, the conductors are connected to the supply converters. This design allows for very high fill factors. Instead of conventional copper, such bars can be in aluminium which is lighter and less expensive. The manufacturing is easier and overall economically convenient if compared to normal windings. Furthermore, the end winding is extremely compact.

- The resulting machine can be considered multi-phase and multi-pole. In fact, each conductor can be seen as a phase winding itself, even if supplying one conductor will always result in current in all the others, so the normal concept of phase has to be reformulated. Changing the number of pole-pairs offers the possibility of working in the best efficiency points of the torque-speed map. In fact, at low speed - high torque operations, the machine can be controlled to operate with high number of pole-pairs; at high speed - low torque conditions, iron, skin and proximity losses are dominant and therefore the number of pole-pairs can be reduced [13].

- ISCAD machine works with low voltage (48 V), so it is intrinsically electrically safe [12]. In fact, the number of turns is one and induced voltages are at minimum. This aspect beneficially impacts the battery design in the EV, because a significant reduction of cells connected in series is possible.
- It can be proved through a FE thermal analysis that ISCAD machine design shows high thermal capability compared with conventional reference machine. The main reason lies in the low thermal resistance between the stator bars and core, and also in the low loss density [13].

WICSC Nevertheless, ISCAD machine presents an inherent disadvantage: the low-voltage operation implies high currents on the stator side, which results in high currents in the supplier (order of 15 kA [14]). For this reason, converters and battery configuration need to be designed ad-hoc since they are not compatible with standard EV high-voltage battery systems [4].

In order to decrease the high current ratings that ISCAD machine requires, a different type of stator winding is needed. Bitsi, Wallmark, and Bosga proposed in [4] a Gramme-type winding in which multi-turn stator coils are independently controlled. This work is based on this concept.

1.2 THESIS STRUCTURE

In chapter 2, a more detailed introduction about WICSC machine is given, for what concerns its main characteristics, geometry and materials. Moreover, brief considerations about a possible drive system are made, in order to portray the full picture in which this machine will operate.

The core of this work is then presented and declined in two different approaches, each of them in a separate part.

The first part deals with the purely analytical-derived transient model. This is based exclusively on analytical equations of different nature (magnetic, electrical circuits and algebraic theory) through which parameters are derived in order to predict the electrical and magnetic behaviour of the machine. In this approach, assumptions are made in order to simplify the dissertation. Chapter 5 and chapter 6 are dedicated to two self parameters, one connecting stator fluxes with stator currents and one considering the same for the rotor. Chapter 7 regards connection on both way between rotor and stator, with more emphasis on rotor currents inducing stator fluxes. Chapter 8 is then centred on matrix derivation, numerical issues and matrix-model set-up.

The second part deals with an analytical transient model derived by means of Finite Element Method (FEM). The idea is to perform different FE simulations by means of COMSOL Multiphysics® to extract parameters to fully describe electrically the machine. This way will be named *FE analytical approach*. Once this is done, ideally FE simulation - which are long and computational demanding - give qualitatively the same results of the FE analytical approach which is instead much faster an overall easier to use.

The third and final part gives a comparison in terms of flux and voltage for the two different models, considering an independent FE simulation as a reference. A second chapter shows final complete simulations to predict electrical currents and mechanical torque given a certain supplying configuration.

2

WICSC MACHINE

As already introduced, the WICSC machine has been proposed by Bitsi, Wallmark, and Bosga in [4]. In this section, such configuration will be explained more in depth.

The key aspect that characterises this machine, from which its name arises, is that each stator coils is wound independently from the others. Figure 2.1 shows a rendering of the machine, in two different views. It is possible to notice conductors in the external part of the stator.

Some considerations can be made:

- First, this design configuration opens up possibilities not available for standard machines, such as the pole and phase changing.
- Second, the external coils do not play an active role; they contribute in terms of losses and are needed as return conductors. On one hand, they represent an additional cost in term of efficiency and manufacturing, but on the other, it is the only way to build an ISCAD machine with a number of turns higher than one, thus reducing the current in favour of higher voltages. These coils will be neglected soon in the following dissertation.
- In principle, supplying only one stator coil would result only in a leakage field penetrating the air-gap, especially if the iron is assumed with high relative permeability. Due to that, at least two stator slots with opposite currents are needed to induce a traditional magnetic flux density in the rotor; to be able to have such opposite currents, special voltage control is required rather than just supplying opposite voltages, to compensate practical

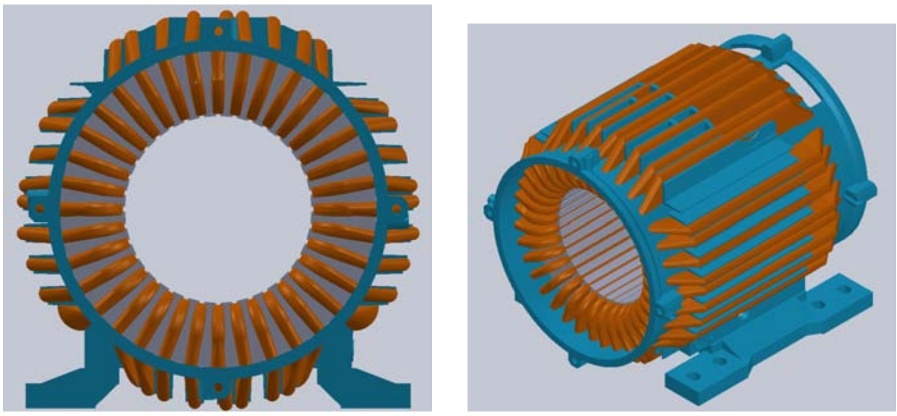

(a) Axial view of the WICSC machine. **(b)** Isometric view of the WICSC machine.

Figure 2.1: Rendering of the WICSC machine without the rotor.

differences between stator coils. One simple solution could be to short-circuit the negative terminals by means of a short-circuit ring.

- More in general, supplying configurations resulting in stator slot currents with non-zero sum should be avoided, since they only contribute to magnetize the stator yoke.
- The concept of phase has to be reconsidered: one stator slot by itself does not end up in one phase since the magnetic field induced in the air-gap could be considered only as a leakage field. In principle, slots belong to the same phase not physically, since they are not physically connected in series, but only electrically, provided a suitable voltage control.
- The machine can be operated neglecting the concept of phases and operating just with different number of poles, as ISCAD machine does.
- For what regards the DC supply, a converter with Q_s terminals is needed; to achieve this, twelve 3-phase inverters are needed, connected to the same DC bus; another solution could be to design one converter with a number of legs equal to the stator slots [4]. The former option is adopted, even if this does not have a direct impact on this work.
- This type of winding is expensive since it requires complex and time-consuming handwork and the quantity of material is roughly twice as in a normal machine. Ultimately, thermal heat dissipation can be affected by such a winding configuration, although this aspect will not be investigated in this work.

2.1 GEOMETRY

The machine is a squirrel cage induction motor. Figure 2.2 shows the complete geometry of the machine.

In particular, from the centre moving outwards, it is possible to notice: shaft, rotor lamination, rotor bars, air-gap, stator-slot wedge, stator slots (divided into two parts), stator yoke lamination, housing to fit the external part of the coils, external coils, external air.

Considering the stator side, there are Q_s slots, in which copper conductors are wound. Within each slot, there are n_s turns. The stator conductor, with a total cross-sectional area S_{cond}, is assumed to be made up of n_{ps} parallel strands each of cross-sectional area S_{str}. Stator slots have a trapezoidal shape and a wedge on the bottom. Then, a slot opening is present resulting in air-gap slot effects. The air-gap length is named δ. Other salient aspects are the stator inner radius $r_{s,in}$ and stator-slot opening width w_{so}, which is useful to compute

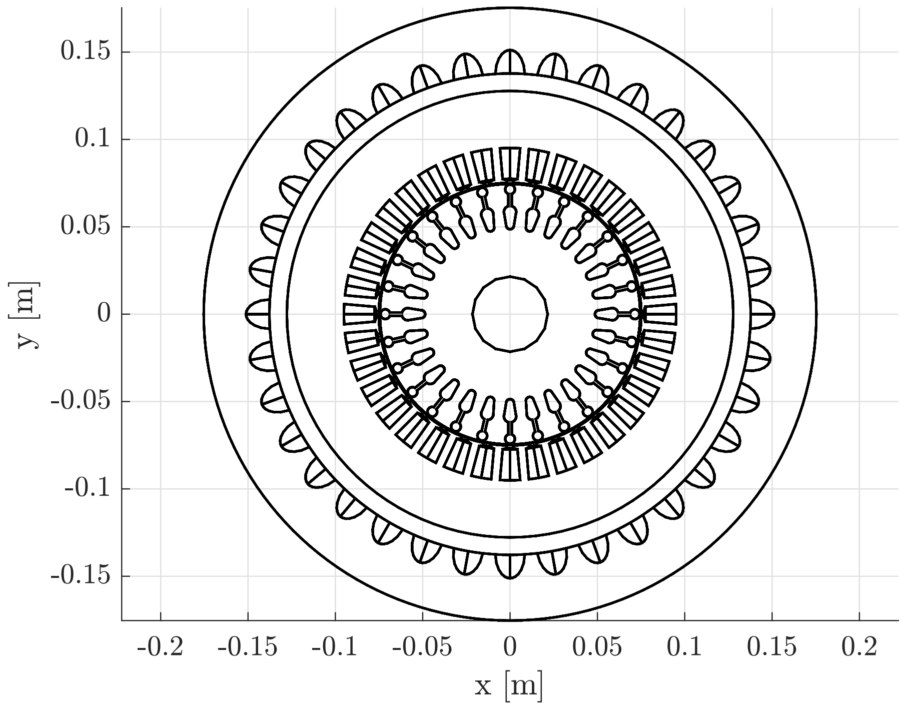

Figure 2.2: Complete 2D representation of the machine.

stator Carter's factor so that an equivalent increased air-gap is used to account for slot openings.

On the rotor side, a deep bar single squirrel cage rotor is found, and the number of bars is set to Q_r. A short-circuit ring is present to connect bars at both endings. The rotor outer radius is set to $r_r = r_{s,in} - \delta$. Finally, there is the shaft whose radius is r_{shaft}; in the z direction, the machine has an axial length set to L_a. In table 2.1, machine geometrical main aspects are summarised.

The convention that will be used is the following: considering fig. 2.2, stator slot 1 is located in the positive x plane at $y = 0$ (at *3 o'clock*), with the respective return current externally aligned. Then, coils have an increasing index j, $j = 1, 2, \dots, Q_s$ moving counter-clockwise, along what is defined as positive tangential direction. The same convention applies for rotor bars, i.e. rotor bar 1 is displaced at *3 o'clock*, and their index k increases by moving counter-clockwise: $k = 1, 2, \dots, Q_r$.

2.2 MATERIALS

Materials are kept as simple as it is possible at this first level of analysis, not to encounter issues related to saturations which does not allow scaling values linearly.

The multiphase machine is defined with the following material properties, that will be useful to define materials in the FE model.

Table 2.1: Main aspects of the WICSC machine.

Name	Symbol	Value	Unit
Number of stator slots	Q_s	36	
Number of rotor bars	Q_r	28	
Number of turns per slot	n_s	18	
Air-gap length	δ	0.6	mm
Active length	L_a	211	mm
Stator inner radius	$r_{s,in}$	75.1	mm
Stator-slot opening width	w_{so}	3.65	mm
Rotor outer radius	r_r	74.5	mm
Shaft radius	r_{shaft}	21.5	mm

- Linearity is assumed in the model, as mentioned above. The relative permeability is assumed to be constant ($\mu_r = 10000$) and saturation effects are not considered. In the final chapter, some simulations will be shown for non-linear materials and proper $B - H$ curve adopted will be given.
- Electrical conductivity of non-conductive materials σ is set to $10\,\mathrm{H\,m^{-1}}$ to avoid numerical issues.
- Stator conductors are made of copper, while rotor bar in aluminium.

The list of materials can be summarised in table 2.2.

Table 2.2: Assumed material properties of WICSC machine FE model.

Part	Material	μ_r	σ [S m^{-1}]
Surrounding material	Air	1	10
Housing		1	10
Stator yoke lamination	Iron	10×10^3	10
Stator slot coil	Copper	1	48×10^6
Stator slot wedge	Air	1	10
Air-gap	Air	1	10
Rotor core lamination	Iron	10×10^3	10
Rotor bar	Aluminium	1	26×10^6
Rotor bar opening	Air	1	10
Shaft		1	10

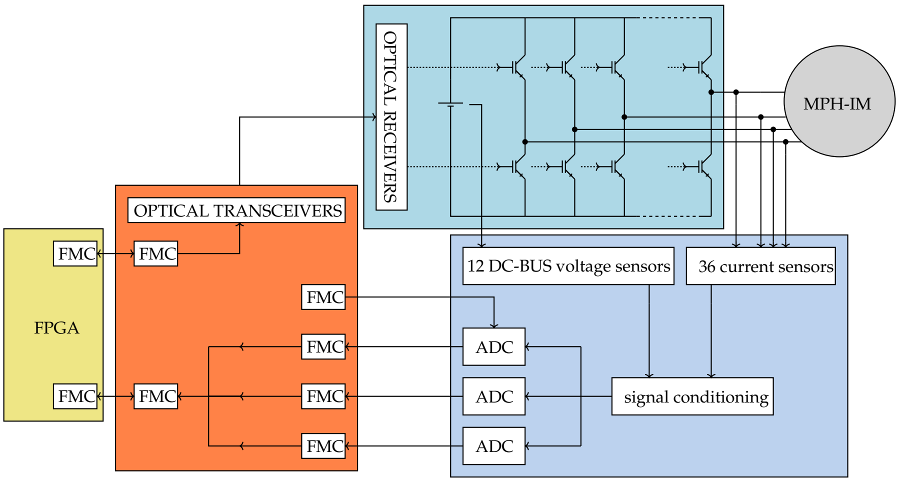
OPTICAL RECEIVERS
MPH-IM
OPTICAL TRANSCEIVERS
FMC
FMC
FPGA
FMC
FMC
FMC
FMC
FMC
FMC
12 DC-BUS voltage sensors
36 current sensors
ADC
ADC
ADC
signal conditioning

Figure 2.3: Schematic representation of the set-up.

2.3 SET-UP CONFIGURATION

The motor model is part of a more complex configuration where hardware and software parts are designed to test the real machine.

Figure 2.3 shows a schematic representation of the set-up. The multi-phase IM (denoted as MPH-IM) is supplied by a Q_s-legs inverter, recalling that $Q_s = 36$. Such a converter consists of twelve 3-phase inverters connected to a DC-BUS. Therefore, it is requested to measure all 36 currents, one per slot, and one DC-BUS voltage value per inverter.

Such signals are conditioned to proper range value to be sampled by Analog Digital Converters (ADCs). Data is then transferred by means of FPGA Mezzanine Card (FMC) connectors to the Field Programmable Gate Array (FPGA) which is executing the control algorithms. This logic computes optical signal commands which are sent and transformed into voltages to drive inverter'gates.

Part I

TRANSIENT MODEL ANALYTICAL DERIVATION

INTRODUCTION

3

3.1 METHOD OVERVIEW

This part describes an analytical model designed to predict the dynamic behaviour of a generic induction motor whose stator slots can be supplied and controlled independently. In this first derivation, it relies on assumptions about ideal behaviour of materials, lack of effects due to the third dimension and lack of losses and leakages.

The underlying idea is to combine the well-known Maxwell's equations and the magnetic equivalences of circuit theory - Kirchhoff Current Laws (KCLs) and Kirchhoff Voltage Laws (KVLs) - to fully describe the electrical and magnetic behaviour of the electrical machine model.

In the first place, Ampère's law is used in order to derive the magnetic flux density in the air-gap induced by a generic set of stator and rotor currents[1] that are configured as primary inputs of the system.

In the second place, air-gap magnetic fluxes are computed, with regards to both stator and rotor. This step takes into account the rotor rotation over time, and therefore its position results in another input of the system.

Thirdly, air-gap magnetic fluxes are combined to describe magnetic fluxes in the stator yoke and the rotor lamination, and those result in flux linking respectively stator coils and rotor bars.

Based on these steps, a linear-matrix relationship between flux linkages and currents is derived. It can be expressed as (3.1), where superposition of effects is assumed. The next section explains the nature of such parameters, while the following chapters derive each of them. Briefly, four parameters are considered:

- $\mathbf{L_s}$: it represents the stator self-connection, i.e. how stator coil currents result in stator flux linkages. This inductance matrix is independent on the rotor position.

- $\mathbf{L_{mut,s-r}}(\theta_r)$: it establishes the link between rotor bar currents and stator coil flux linkages. Such a matrix depends on the rotor position.

- $\mathbf{L_{mut,r-s}}(\theta_r)$: it relates stator coil currents with rotor bar flux linkages. Also this inductance matrix is a function of the rotor position.

---

[1] Conditions on the supplying currents will be given later.

- $\mathbf{L_r}$: it gives the rotor self-connection. As for the stator, this inductance matrix does not change over the rotor position.

$$\begin{cases} \boldsymbol{\Psi}_\mathbf{s} = \mathbf{L_s i_s} + \mathbf{L_{mut,s-r}}(\theta_r)\mathbf{i_r} \\ \boldsymbol{\Psi}_\mathbf{r} = \mathbf{L_{mut,r-s}}(\theta_r)\mathbf{i_s} + \mathbf{L_r i_r} \end{cases} \tag{3.1}$$

Furthermore, stator coil and rotor bar resistance[2] are derived analytically, neglecting end-windings and non-uniform distribution of currents.

Therefore, the following set of equations can be written:

$$\begin{cases} \mathbf{V_s} = R_s\mathbf{i_s} + \dfrac{d\boldsymbol{\Psi}_\mathbf{s}(\mathbf{i_s}, \mathbf{i_r})}{dt} \\ 0 = R_r\mathbf{i_r} + \dfrac{d\boldsymbol{\Psi}_\mathbf{r}(\mathbf{i_s}, \mathbf{i_r})}{dt} \end{cases} \tag{3.2}$$

Equation (3.2) can be solved directly to compute voltages given currents as input. It can also be solved for currents, configuring stator coil voltages as input, as it is in reality. Following the latter way, a Differential Algebraic Equation (DAE) is defined and solved by means of a numerical algorithm. In fact, by substituting (3.1) into (3.2), (3.3) can be written.

$$\begin{bmatrix} \mathbf{V_s} \\ \mathbf{V_r} \end{bmatrix} = \begin{bmatrix} \mathbf{R_s} & \frac{d\mathbf{L_{mut,s-r}}}{dt} \\ \frac{d\mathbf{L_{mut,r-s}}}{dt} & \mathbf{R_r} \end{bmatrix} \begin{bmatrix} \mathbf{i_s} \\ \mathbf{i_r} \end{bmatrix} + \begin{bmatrix} \mathbf{L_s} & \mathbf{L_{mut,s-r}} \\ \mathbf{L_{mut,r-s}} & \mathbf{L_r} \end{bmatrix} \begin{bmatrix} \frac{d\mathbf{i_s}}{dt} \\ \frac{d\mathbf{i_r}}{dt} \end{bmatrix} \tag{3.3}$$

Therefore, the ultimate scope is to derive stator and rotor currents as a function of rotor position over time and stator coil voltages, supplied as driving quantities.

This part is structured as follows: first, resistances are found under the aforementioned hypothesis. Second, four matrices defining eq. (3.1) are derived independently. These parameters will be validated in the next parts of this work by comparing them to a FE equivalent simulation in Comsol Multiphysics[3] which is assumed to be the reference benchmark.

3.2 PARAMETERS' NATURE

It must be stated that parameters in eq. (3.1) cannot be considered inductances in the classical and physical meaning, since they are not related to the geometry and magnetic quantities of the machine. In fact, they are not self-consistent.

To explain this concept, consider a simplified model of a standard electrical machine. When a single-phase winding is considered, there are always at least two slots supplied with opposite currents, i.e. they are physically connected in series, and this occurs in every occasion.

---

[2] Including short-circuit rings.

[3] Comsol Multiphysics® is a registered trademark of Comsol AB, Stockholm, Sweden.

For the WICSC machine, this does not hold by itself. In fact, every slot is in principle independent. To solve this issue, all stator coils are star-connected, and therefore there will always be a returning current even if a single coil is supplied. In the theoretical dissertation, this results in the unavoidable assumption that currents in stator slots must result in zero-sum. As it will be explained throughout this part, such an assumption is essential to respect the solenoidal nature of magnetic field density when stator core material is ideal.

4 RESISTANCE DERIVATION

4.1 STATOR COIL RESISTANCE

The first parameter to derive is the stator coil resistance.

There are n_s turns per slot; the conductor is made up of n_{ps} parallel elementary strands, each of area S_{str}. By defining L_{sb} as the width of the stator yoke and L_{hs} as the width of the housing portion, stator coil resistance is computed by considering n_s series of one-turn resistance, which is made up of a component along the z dimension, R_{al} and resistance portion in the $x-y$ plane, for the width of the stator yoke and the housing (R_{ew}).

Therefore, by assuming an operating temperature of 80 °C, it is possible to express the total slot resistance as:

$$\begin{aligned} R_s &= n_s R_{turn} && (4.1) \\ &= n_s 2\,(R_{al} + R_{ew}) && (4.2) \\ &= 2n_s \left(\rho_{Cu,80\,^\circ C} \frac{L_a}{S_{cond}} + \rho_{Cu,80\,^\circ C} \frac{L_{sb} + L_{hs}}{S_{cond}} \right) && (4.3) \end{aligned}$$

where:

- $\rho_{Cu,80\,^\circ C} = \rho_{Cu,20\,^\circ C}(1 + \alpha_{Cu}\Delta T)$, where:
  - $\rho_{Cu,20\,^\circ C} = 1.68 \times 10^{-8}\,\Omega\,m$
  - $\alpha_{Cu} = 3.9 \times 10^{-3}\,K^{-1}$
  - $\Delta T = 60\,K$.
- $S_{cond} = n_{ps} S_{str} = n_{ps} \pi r_{str}^2$

Since in the FE model the end winding is not modeled, this component is neglected also in the analytical derivation, in order to match FE results.

Ultimately, the value of each stator coil resistance is:

$$R_s = 23.95\,m\Omega \qquad (4.4)$$

4.2 ROTOR BAR RESISTANCE

The equivalent rotor resistance R_r is computed by accounting for the actual rotor bar resistance and the short circuit ring portion. First, we declare the following elements:

- p: number of poles.
- l_b: length of one rotor bar.
- b: equivalent bar width.
- d: equivalent bar depth.
- l_1: length considering ducts.
- l_{be}: rotor bar extension on one side.
- t_{be}: end-ring width.
- d_{be}: end-ring depth.
- α_{sk}: skew angle.
- τ_{r2}: tooth pitch at the middle of the air-gap.

Then, it can be derived [15] that the equivalent rotor bar resistance including the portion of end-ring is:

$$R_r = R_b + \frac{R_{er}}{2\sin^2\left(\frac{p\pi}{2Q_r}\right)} \tag{4.5}$$

where:

$$R_b = \rho_{Al}\frac{l_b}{bd} \tag{4.6}$$

$$l_b = \frac{l_1 + 2l_{be} + 2\frac{1}{3}t_{be}}{\cos\alpha_{sk}} \tag{4.7}$$

$$R_{er} = \rho_{Al}\frac{\tau_{r2}}{t_{be}d_{be}} = \rho_{Al}\frac{\frac{\pi D_{outerRotor}}{Q_r}}{t_{be}d_{be}} \tag{4.8}$$

In the first place, the equivalent rotor bar resistance depends on the number of poles: fig. 4.1 shows how $R_{r,eq}$ changes for different number of poles with respect to the 2-poles configuration.

In the second place, it is worth to notice that the term $1/3t_{be}$ in (4.7) considers the portion of rotor bar over the end-ring. It is an equivalent extension of the rotor bar that takes into account that the current bends from the bar into the end-ring over the distance t_{be}.

Moreover, the end-ring section is assumed to be squared and its area such that the end-ring current density (J_{er}) is equal to the rotor bar current density (J_b). This results in:

$$J_b = J_{er} \rightarrow \frac{i_b}{S_b} = \frac{i_{er}}{S_{er}} \tag{4.9}$$

that can be further expressed by recalling that [15, 16]:

$$i_{er} = \frac{i_b}{2\sin\left(\frac{\pi p}{2Q_r}\right)} \tag{4.10}$$

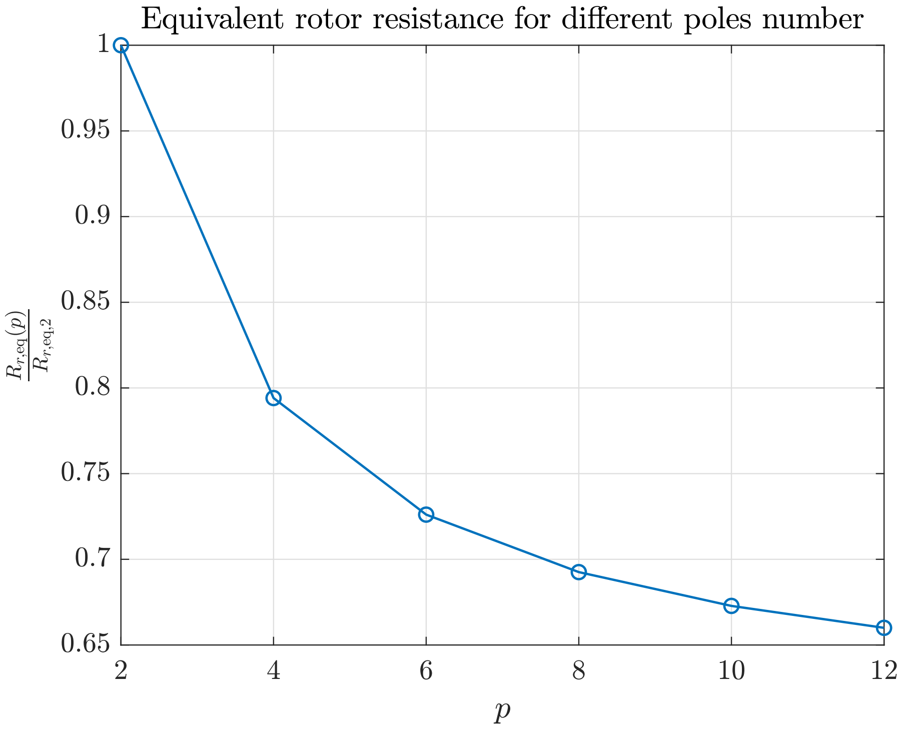

Figure 4.1: Comparison between equivalent rotor bar resistance for different number of poles.

so that:

$$S_{er} = \frac{S_b}{2\sin\left(\frac{\pi p}{2Q_r}\right)} \tag{4.11}$$

Therefore, the numeric values for $p = 2$ are reported below.

$$R_b = 7.4 \times 10^{-5}\,\Omega \tag{4.12}$$

$$R_{er} = 1.31 \times 10^{-6}\,\Omega \tag{4.13}$$

$$R_r = 1.26 \times 10^{-4}\,\Omega \tag{4.14}$$

5

STATOR FLUX LINKAGE DUE TO STATOR CURRENTS: L_s

In this chapter, it is explained how the analytical approach is carried out in order to obtain $\mathbf{L_s}$. This parameter links the stator current $\mathbf{i_s}$ with the flux linkage in the stator yoke $\mathbf{\Psi_s}$, or in matrix notation:

$$\mathbf{\Psi_s} = \mathbf{L_s}\mathbf{i_s} \tag{5.1}$$

This flux has tangential orientation and it is passing through an ideal surface defined by stator slots and the corresponding external coil.

Since no other currents nor fluxes are considered apart from stator-related ones, a simplified notation is assumed throughout this chapter, i.e. being x a generic quantity, $x = x_s = x^s$.

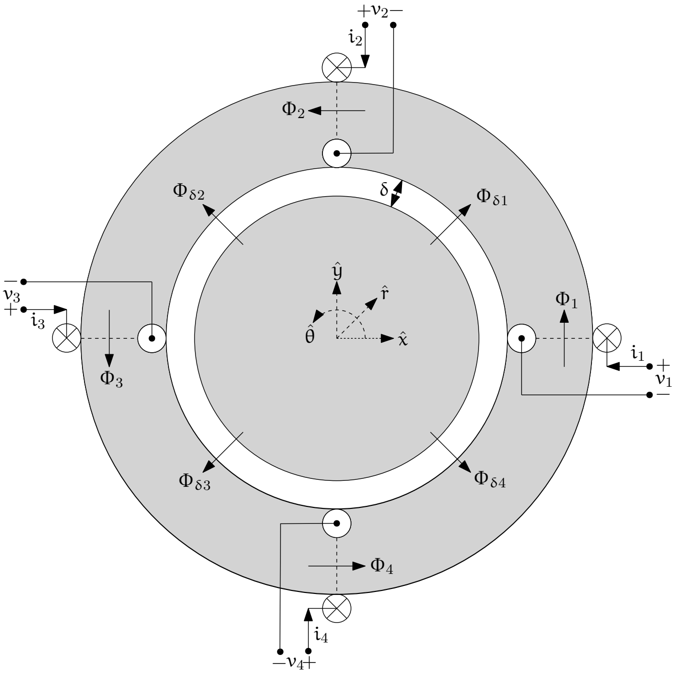

Figure 5.1: Machine configuration with $Q_s = 4$.

5.1 AIR-GAP MAGNETIC FIELD INDUCED BY STATOR CURRENTS

Consider the simplified illustration of the multiphase induction machine in fig. 5.1. For this analysis we consider a smooth stator and rotor surface, i.e. slot opening effects are neglected. The air-gap is denoted by δ, while $\Phi^s_{\delta,j} = \Phi_{\delta,j}$ represents the radial magnetic flux in the air-gap between coil j and coil $j+1$. Finally, $\Phi_j^s = \Phi_j$ indicated the magnetic flux in the stator yoke, and therefore $\Psi_j^s = \Psi_j$ is the flux linking to coil j.

Now we postulate the low-frequency approximation of Maxwell's equations in differential form as:

$$\nabla \times \mathbf{H} = \mathbf{J} \tag{5.2}$$

$$\nabla \times \mathbf{E} = -\frac{d\mathbf{B}}{dt} \tag{5.3}$$

$$\nabla \cdot \mathbf{B} = 0 \tag{5.4}$$

$$\nabla \cdot \mathbf{D} = \rho \tag{5.5}$$

Equation (5.2) - also known as Ampère's law - can be expressed on integral form as:

$$\iint_S \nabla \times \mathbf{H} \cdot \hat{\mathbf{n}}\, dS = \iint_S \mathbf{J} \cdot \hat{\mathbf{n}}\, dS \tag{5.6}$$

and it can be further arranged - by means of Stokes'theorem - as

$$\oint_{\partial S} \mathbf{H} \cdot \hat{\mathbf{r}}\, dr = \iint_S \mathbf{J} \cdot \hat{\mathbf{n}}\, dS \tag{5.7}$$

where S stands for the surface defined by the closed path ∂S and $\hat{\mathbf{l}}$, the tangential versor, and $\hat{\mathbf{n}}$, the normal versor, are related by the right-hand rule.

If we now evaluate this integral first along the path 1234 of fig. 5.2, then on the other path $1'2'3'4'$ and so forth, and by means of eq. (5.4), it is possible to write the following system of equations which is valid for a generic machine with Q_s stator coils:

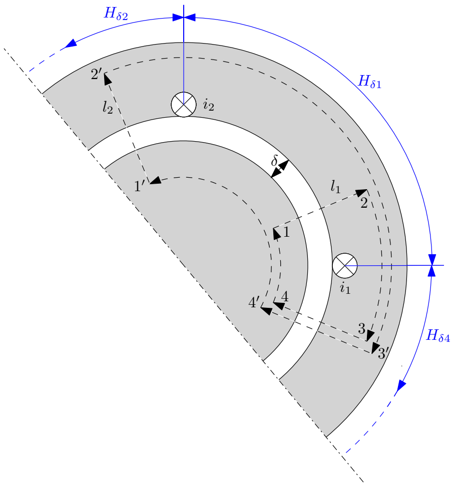

Figure 5.2: Line integral paths considered, machine configuration with $Q_s = 4$.

$$\begin{cases} H_{\delta,1} = H_{\delta,Q_s} - \frac{n_s}{\delta} i_1 \\ H_{\delta,2} = H_{\delta,Q_s} - \frac{n_s}{\delta}(i_1 + i_2) \\ \vdots \\ H_{\delta,Q_s} = H_{\delta,Q_s} - \frac{n_s}{\delta}(i_1 + i_2 + \ldots + i_{Q_s}) \\ \sum_{j=1}^{Q_s} H_{\delta,j} = 0 \end{cases} \tag{5.8}$$

where:

- $H_{\delta,Q_S} = H_{\delta,Q_s} - \frac{n_s}{\delta} \sum_{j=1}^{Q_s} i_j$ implies that $\sum_{j=1}^{Q_s} i_j = 0$, i.e. the system of input currents must have zero-sum. Therefore, this is the reason of the *WICSC-balanced currents* hypothesis, which is assumed in the following discussion.
- $\sum_{j=1}^{Q_s} H_{\delta,j} = 0$ is derived from Maxwell's equation (5.4):

  $$\nabla \cdot \mathbf{B} = 0.$$

  This equation can be further expressed in the following manner:

  $$\begin{aligned} 0 &= \frac{n_s}{\delta}\left\{Q_s i_1 + (Q_s - 1) i_2 + \ldots + \left[Q_s - (Q_s - 1) i_{Q_s}\right]\right\} + Q_s H_{Q_s} \\ &= \frac{n_s}{\delta} \sum_{j=1}^{Q_s} i_j \left[Q_s - (j-1)\right] + Q_s H_{Q_s} \end{aligned} \tag{5.9}$$

  so that:

  $$H_{Q_s} = \frac{n_s}{Q_s \delta} \sum_{j=1}^{Q_s} i_j \left[Q_s - (j-1)\right] \tag{5.10}$$

The system can be written in a matrix form as follows:

$$\begin{bmatrix} 1 & 0 & 0 & \cdots & 0 & -1 \\ 0 & 1 & 0 & \cdots & 0 & -1 \\ 0 & 0 & 1 & \cdots & 0 & -1 \\ \vdots & \vdots & & & \ddots & \\ 0 & 0 & 0 & \cdots & 0 & 1 \end{bmatrix} \begin{bmatrix} H_{\delta,1} \\ H_{\delta,2} \\ H_{\delta,3} \\ \vdots \\ H_{\delta,Q_s} \end{bmatrix} =$$

$$= -\frac{n_s}{\delta} \begin{bmatrix} 1 & 0 & 0 & \cdots & 0 & 0 \\ 1 & 1 & 0 & \cdots & 0 & 0 \\ 1 & 1 & 1 & \cdots & 0 & 0 \\ 1 & 1 & 1 & \cdots & 1 & 0 \\ -1 & -\frac{Q_s-1}{Q_s} & -\frac{Q_s-2}{Q_s} & \cdots & -\frac{Q_s-(Q_s-2)}{Q_s} & -\frac{Q_s-(Q_s-1)}{Q_s} \end{bmatrix} \begin{bmatrix} i_1 \\ i_2 \\ i_3 \\ \vdots \\ i_{Q_s} \end{bmatrix} \tag{5.11}$$

which in compact notation results in:

$$\mathbf{M_1 H_\delta} = -\frac{n_s}{\delta} \mathbf{M_2 i} \tag{5.12}$$

Since $\det(\mathbf{M_1}) \neq 0$, $\mathbf{M_1}$ can be inverted. If we introduce $\mathbf{M_{i,H}} \triangleq -\frac{n_s}{\delta}\mathbf{M_1}^{-1}\mathbf{M_2}$, (5.12) can be written as:

$$\mathbf{H}_\delta = \mathbf{M_{i,H}}\mathbf{i} \tag{5.13}$$

5.2 MAGNETIC FLUX LINKED TO STATOR COILS

The goal is to compute the stator coil magnetic flux linkage directly from input currents. To do that, we write an equation in matrix form:

$$\boldsymbol{\Psi} = \mathbf{Li} \tag{5.14}$$

5.2.1 *Relation between air-gap magnetic flux and stator currents*

In the first place, we need to derive an expression for air-gap magnetic flux. We know that:

$$\begin{aligned} \Phi_\delta &= \iint_S \mathbf{B}_\delta \cdot \hat{\mathbf{n}}\, dS = B_\delta S_{\text{air-gap}} = B_\delta L_a \frac{2\pi}{Q_s} r_{s,in} \\ &= \mu_0 H_\delta L_a \frac{2\pi}{Q_s} r_{s,in} \end{aligned} \tag{5.15}$$

which, by using (5.13) and imposing

$$k \triangleq \mu_0 L_a \frac{2\pi}{Q_s} r_{s,in} \tag{5.16}$$

can be written in matrix form as:

$$\boldsymbol{\Phi}_\delta = k\mathbf{M_{i,H}} \cdot \mathbf{i} \tag{5.17}$$

5.2.2 *Relation between air-gap magnetic flux and flux in the stator yoke*

In the second place, we need to find the matrix relation between air-gap flux and flux in the stator back. Such a relation can be represented by:

$$\boldsymbol{\Phi} = \mathbf{M_3}\boldsymbol{\Phi}_\delta \tag{5.18}$$

In order to do that, we start by imposing the following conditions, considering fig. 5.1:

$$\begin{cases} \Phi_{\delta,1} = \Phi_2 - \Phi_1 \\ \Phi_{\delta,2} = \Phi_3 - \Phi_2 \\ \Phi_{\delta,3} = \Phi_4 - \Phi_3 \\ \Phi_{\delta,4} = \Phi_5 - \Phi_4 \\ \vdots \\ \Phi_{\delta,Q_s-1} = \Phi_{Q_s} - \Phi_{Q_s-1} \\ \Phi_{\delta,Q_s} = \Phi_1 - \Phi_{Q_s} \end{cases} \tag{5.19}$$

They result in a singular matrix that cannot be inverted. In appendix B it is shown how the connection between air-gap and stator yoke fluxes can be achieved and, in particular, theorem B.6.1 provides the final equation to derive yoke fluxes from air-gap fluxes[1].

In this way, matrix $\mathbf{M_3}$ is obtained.

5.2.3 *Relation between currents and flux in the stator yoke:* L_s

Taking advantage of previous sections, starting by using 5.2.1, recalling (5.17)

$$\boldsymbol{\Psi} = n_s \boldsymbol{\Phi} = n_s \mathbf{M_3} k \mathbf{M_{i,H}} \cdot \mathbf{i} \tag{5.20}$$

$$= n_s \mathbf{M_3} \mu_0 L_a \frac{2\pi}{Q_s} r_{s,in} \left(-\frac{n_s}{\delta}\right) \mathbf{M_1}^{-1} \mathbf{M_2} \cdot \mathbf{i} \tag{5.21}$$

so that ultimately:

$$\mathbf{L_s} \triangleq n_s \mu_0 L_a \frac{2\pi}{Q_s} r_{s,in} \left(-\frac{n_s}{\delta}\right) \mathbf{M_3} \mathbf{M_1}^{-1} \mathbf{M_2} \tag{5.22}$$

---

[1] Other conditions are needed and legit, as described in appendix B.

6

ROTOR FLUX LINKAGE DUE TO ROTOR CURRENT: L_r

In this chapter, it is explained how the analytical approach is carried out in order to obtain $\mathbf{L_r}$. This parameter links rotor bar currents $\mathbf{i_r}$ with flux linkage in the rotor lamination $\mathbf{\Psi_r}$, which will be defined precisely later on. In matrix notation:

$$\mathbf{\Psi_r} = \mathbf{L_r}\mathbf{i_r} \tag{6.1}$$

Since no other currents nor fluxes are considered apart from rotor-related ones, a simplified notation is assumed throughout this chapter, i.e. being x a generic quantity, $x = x_r = x^r$. Most of the elements have already been introduced in the previous chapter with respect to $\mathbf{L_s}$, therefore this section does not go into details since this would be a mere repetition of what already done. However, differences will be highlighted.

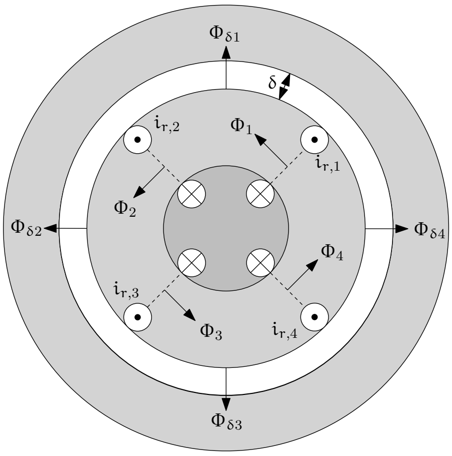

Figure 6.1: Rotor configuration with $Q_s = 4$.

6.1 AIR-GAP MAGNETIC FIELD INDUCED BY ROTOR CURRENTS

Following the same approach used in chapter 5, it is possible to adopt the same reasoning described in section 5.1 with the only difference that there are no rotor turns, i.e. $n_r = 1$ and therefore flux and flux linkage is the same.

By accepting this, it is possible to write relation (5.12) valid for the rotor currents:

$$\mathbf{M_1}\mathbf{H_\delta} = -\frac{1}{\delta}\mathbf{M_2}\mathbf{i} \tag{6.2}$$

where $\mathbf{M_1}$ and $\mathbf{M_2}$ come from (5.11) considering Q_r instead of Q_s. Since $\det(\mathbf{M_1}) \neq 0$, $\mathbf{M_1}$ can be inverted. If we introduce $\mathbf{M_{i,H}} \triangleq -\frac{1}{\delta}\mathbf{M_1}^{-1}\mathbf{M_2}$, (6.2) can be written as:

$$\mathbf{H}_\delta = \mathbf{M_{i,H}}\mathbf{i} \tag{6.3}$$

6.2 MAGNETIC FLUX LINKED BY ROTOR BARS

The goal is to compute rotor bar magnetic flux linkage directly from input rotor currents. To do that, we write an equation in matrix form:

$$\mathbf{\Psi} = \mathbf{L}\mathbf{i} \tag{6.4}$$

6.2.1 *Relation between air-gap magnetic flux and stator currents*

In the first place, we need to derive an expression for air-gap magnetic flux. We know that:

$$\begin{aligned} \Phi_\delta &= \iint_S \mathbf{B}_\delta(\mathbf{i_r}) \cdot \hat{\mathbf{n}}\, dS = B_\delta S_{\text{air-gap}} = B_\delta L_a \frac{2\pi}{Q_s}(r_{s,in} - \delta) \\ &= \mu_0 H_\delta L_a \frac{2\pi}{Q_s}(r_{s,in} - \delta) \end{aligned} \tag{6.5}$$

which, by using (6.2) and imposing

$$k \triangleq \mu_0 L_a \frac{2\pi}{Q_s}(r_{s,in} - \delta) \tag{6.6}$$

can be written in matrix form as:

$$\mathbf{\Phi}_\delta = k\mathbf{M_{i,H}} \cdot \mathbf{i} \tag{6.7}$$

6.2.2 *Relation between air-gap and rotor lamination magnetic flux*

In the second place, a matrix relation between air-gap flux and flux in the rotor lamination needs to be found. Such a relation can be represented by:

$$\mathbf{\Phi} = \mathbf{M}\mathbf{\Phi}_\delta \tag{6.8}$$

Rotor lamination flux $\mathbf{\Phi}$ is properly introduced below.

ROTOR LAMINATION FLUX DEFINITION Consider the schematic drawing of fig. 6.2. It represents two rotor bars, with their resistance, two portions of end-rings connecting them on both sides. Letters consider the cut-plane at $z = -L_a/2$, ones with the prime symbol at $z = L_a/2$. We refer to C and D and the corresponding C′ and D′ to the shaft points radially aligned with A,A′,B,B′. The following equations can be written:

$$-\frac{d\Phi_j}{dt} = R_{bar} i_{b,j} \tag{6.9}$$

$$\frac{d\Phi_{j+1}}{dt} = R_{bar} i_{b,j+1} \tag{6.10}$$

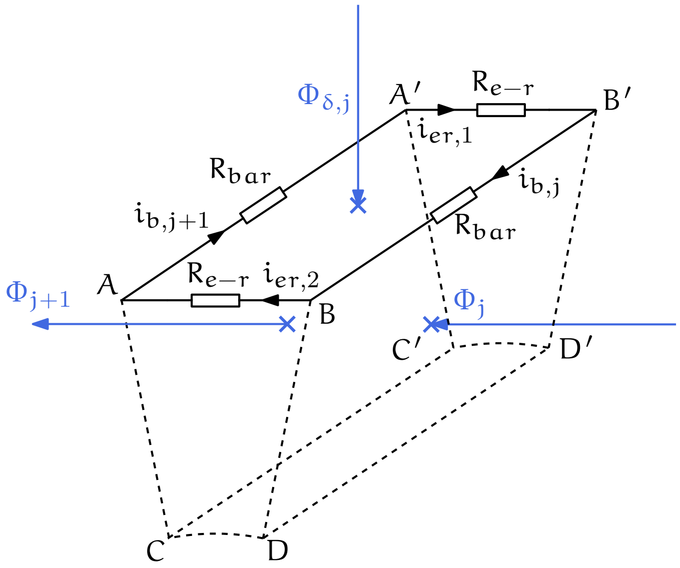

Figure 6.2: Schematic representation of air-gap and rotor bar fluxes.

In this work, it is assumed that the path $AA'C'C$ define a closed loop and Φ_{j+1} is the flux linking this loop; the same applies for Φ_j with regards to $BB'D'D$. Therefore, this means that fictitious ideal conductors are introduced inside the shaft and they are ideally short-circuited to each bar so that a proper loop is defined. As a result, $\mathbf{\Phi}$ is not the air-gap magnetic flux vector, but it rather contains tangential fluxes passing in the rotor lamination portion between a rotor bar and the shaft.

ROTOR LAMINATION FLUX DERIVATION In order to derive (6.8), we start by imposing the following conditions, considering fig. 6.1:

$$\begin{cases} \Phi_{\delta,1} = \Phi_1 - \Phi_2 \\ \Phi_{\delta,2} = \Phi_2 - \Phi_3 \\ \Phi_{\delta,3} = \Phi_3 - \Phi_4 \\ \Phi_{\delta,4} = \Phi_4 - \Phi_5 \\ \vdots \\ \Phi_{\delta,Q_s-1} = \Phi_{Qs-1} - \Phi_{Q_s} \\ \Phi_{\delta,Q_s} = \Phi_{Q_s} - \Phi_1 \end{cases} \tag{6.11}$$

They result, as it happened for the equivalent matrix with respects to $\mathbf{L_s}$, in a singular matrix that cannot be inverted. In appendix B it is shown how the connection between air-gap and stator yoke fluxes can be achieved and, in particular, theorem B.6.1 provides the final equation to derive yoke fluxes from air-gap fluxes[1].

---

[1] Other conditions are needed and legit, as described in appendix B.

What is needed here is the same matrix but with opposite sign since the flux conventions are different. For convenience, matrix that will be used in rotor equations will be referred as $-\mathbf{M}_3$, so that:

$$\mathbf{\Phi} = -\mathbf{M}_3 \mathbf{\Phi}_\delta \tag{6.12}$$

6.2.3 *Relation between currents and flux in the stator yoke:* L_s

Taking advantage of previous sections, starting by using (6.8), recalling (6.7)

$$\mathbf{\Psi} = \mathbf{\Phi} = -\mathbf{M}_3 k \mathbf{M}_{\mathbf{i},\mathbf{H}} \cdot \mathbf{i} \tag{6.13}$$

$$= -\mathbf{M}_3 \mu_0 L_a \frac{2\pi}{Q_s} (r_{s,in} - \delta) \left(-\frac{1}{\delta}\right) \mathbf{M_1}^{-1} \mathbf{M_2} \cdot \mathbf{i} \tag{6.14}$$

so that ultimately:

$$\mathbf{L_r} \triangleq -\mu_0 L_a \frac{2\pi}{Q_s} (r_{s,in} - \delta) \left(-\frac{1}{\delta}\right) \mathbf{M}_3 \mathbf{M_1}^{-1} \mathbf{M_2} \tag{6.15}$$

7

CONNECTION BETWEEN ROTOR AND STATOR: MUTUAL MATRICES

Below two sections explain how connection matrices are derived. First, a connection between stator flux linkage induced by rotor currents is explained, and second the other way is briefly introduced, since it relies on the same theoretical approach.

7.1 STATOR FLUX LINKAGE DUE TO ROTOR CURRENTS: $L_{mut,s-r}(\theta_r)$

7.1.1 *Introduction*

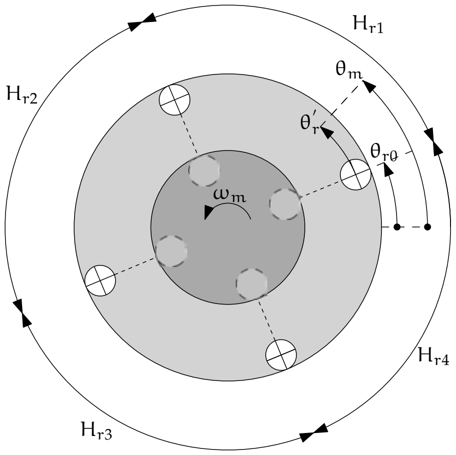

Figure 7.1: Rotor configuration with $Q_s = 4$.

This section describes how the connection between rotor bar currents and stator flux linkages is achieved, i.e. how $\mathbf{L}_{\mathbf{mut,s-r}}(\theta_r)$ is obtained. This matrix - that changes with the rotor position θ_r - links the magnetic flux in the stator yoke $\mathbf{\Psi_s}(\mathbf{i_r})$ with the inducing rotor currents $\mathbf{i_r}$.

$$\mathbf{\Psi_s} = \mathbf{L}_{\mathbf{mut,s-r}}(\theta_r)\mathbf{i_r} \tag{7.1}$$

Because only rotor currents'effects are considered, the formal expression of flux dependencies on them is omitted throughout this chapter.

Therefore, a set of rotor currents $i_{r,j}$, $j = 1, 2, \dots, Q_r$ is given as input. It induces a magnetic flux density through the air-gap $\mathbf{B}_\delta$ which is assumed to be radial and whose magnitude is assumed to vary only along the tangential coordinate (i.e. $\mathbf{B}_\delta = B_\delta(\theta)\mathbf{\hat{r}}$). Then, the air-gap magnetic flux density through the Q_s stator coils $\mathbf{\Phi}_\delta^\mathbf{s}$ is derived and ultimately the flux linking the stator coils $\mathbf{\Psi}_\mathbf{s}^\mathbf{s}$ is obtained.

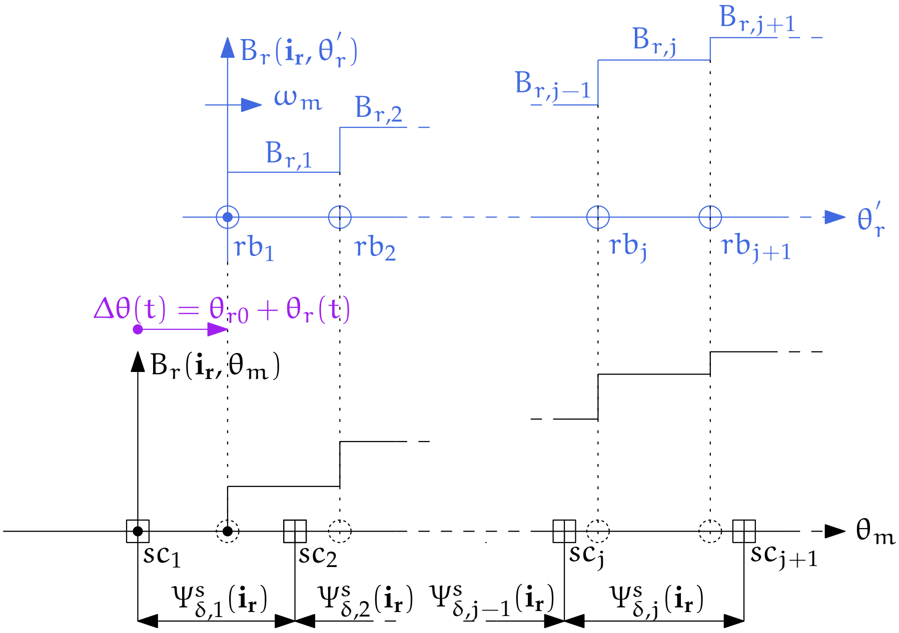
$B_r(\mathbf{i_r}, \theta'_r)$
ω_m
$B_{r,1}$
$B_{r,2}$
$B_{r,j-1}$
$B_{r,j}$
$B_{r,j+1}$
θ'_r
rb_1
rb_2
rb_j
rb_{j+1}
$\Delta\theta(t) = \theta_{r0} + \theta_r(t)$
$B_r(\mathbf{i_r}, \theta_m)$
θ_m
sc_1
sc_2
sc_j
sc_{j+1}
$\Psi^s_{\delta,1}(\mathbf{i_r})$
$\Psi^s_{\delta,2}(\mathbf{i_r})$
$\Psi^s_{\delta,j-1}(\mathbf{i_r})$
$\Psi^s_{\delta,j}(\mathbf{i_r})$

Figure 7.2: Rotor configuration with $Q_s = 4$.

Referring to fig. 7.1, we introduce the following quantities:

- θ'_r: coordinate system integral with the rotor (i.e. rotating with respect to the stator). Its origin corresponds to the first rotor bar.
- θ_{r0}: relative position of the first rotor with respect to the first stator coil at time zero. This parameter is set to zero, i.e. the first rotor bar and the first stator coil are aligned at the zero time.
- $\theta_r(t)$: position of the first rotor bar with respect to the stator in different time instants.
- θ_m: coordinate system integral with the stator, whose origin is set integral with the first stator coil, and which is standstill.
- $H^r_{r,j}(\theta'_r)$: constant value of air-gap magnetic field - induced by the $\mathbf{i_r}$ - between rotor bar j and $j+1$, $j = 1, 2, \dots, Q_r$.
- ω_m: mechanical speed of the rotor. In this dissertation this value can change instant by instant since the rotor position is used.

Furthermore, it is useful to distinguish between quantities referred to the stator and those referred to the rotor. Let X be a generic quantity, the former will be denoted as X^s, the latter as X^r.

7.1.2 *Derivation*

By taking advantage of the method explained in section 6.2.1, it is possible to write a linear matrix relationship between the input rotor currents and the magnetic flux density in the air-gap. Recalling that the second quantity is piecewise constant between two consecutive rotor bars, we can write:

$$\mathbf{H}^{\mathbf{r}}_{\delta} = \mathbf{H}_{\delta}\left(\theta_r^{'}\right) = \mathbf{M}_{\mathbf{i},\mathbf{H}}\mathbf{i}_{\mathbf{r}} \tag{7.2}$$

where $\mathbf{M}_{\mathbf{i},\mathbf{H}}$ is a $Q_r \times Q_r$ matrix identical to (6.3). In fig. 7.2, a simplified representation of such a physical quantity is given. The blue axis is referred to a rotor frame as described above; *rb$_j$* stands for *rotor bar j-th* while *sc$_k$* for *stator coil k-th*. It can be readily inferred that any quantity in the stator frame can be referred to the rotor frame simply by means of a translation in the tangential coordinate θ. More precisely,

$$\theta_m = \theta_r^{'} + \Delta\theta(t) \tag{7.3}$$

where $\Delta\theta(t) = \theta_{r0} + \theta_r(t)$ and $\theta_r(t) = \int_0^t \omega_m(\tau)d\tau = \omega_m t$ if the mechanical speed was constant.

The air-gap magnetic flux passing through two consecutive stator slots j and $j+1$ can be expressed as follows. If we define, for seek of simplicity in the notation:

$$C \triangleq L_a \frac{2\pi}{Q_s} r_{s,in} \tag{7.4}$$

$$\Phi^s_{\delta,k} = C\int_{\frac{2\pi}{Q_s}(j)}^{\frac{2\pi}{Q_s}(j+1)} B^s_{\delta,k}(\theta_m)d\theta_m = C\int_{\frac{2\pi}{Q_s}(j)}^{\frac{2\pi}{Q_s}(j+1)} B^r_{\delta,k}(\theta_r^{'} - \Delta\theta_{r,k})d\theta_r^{'} \tag{7.5}$$

$$= C\int_{\frac{2\pi}{Q_s}(j)-\Delta\theta_{r,k}}^{\frac{2\pi}{Q_s}(j+1)-\Delta\theta_{r,k}} B^r_{\delta,k}(\theta_r^{'})d\theta_r^{'} \tag{7.6}$$

that can be interpreted as follow: the flux could be obtained in two different but equivalent ways:

- integrating between fixed positions (i.e. integral with the stator) the magnetic flux density function that changes over time (due to the variation in the current) and over space (due to the rotor position moving).

- integrating between rotating positions (i.e. integral with the rotor) the magnetic flux density function that changes only over time.

The letter approach is adopted for seek of simplicity, since (7.2) readily gives the value of $\mathbf{H}^r$ - and therefore $\mathbf{B}^r$ - integral with the rotor.

The main challenge is to write (7.6) in a matrix form, so that it is a linear function of the rotor currents.

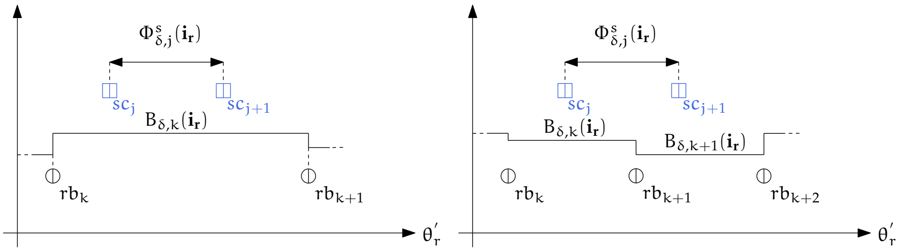
$\Phi^s_{\delta,j}(\mathbf{i}_r)$
sc_j
sc_{j+1}
$B_{\delta,k}(\mathbf{i}_r)$
$B_{\delta,k+1}(\mathbf{i}_r)$
rb_k
rb_{k+1}
rb_{k+2}
θ'_r

(a) Stator coils with no bar in between. **(b)** Stator coils with one bar in between.

Figure 7.3: Two scenarios for the relative position of rotor bars and stator coils.

7.1.3 *Air-gap flux derivation*

Figure 7.3 shows, for a specific time instant, the position of two consecutive stator coils and two rotor bars inducing magnetic field density. The magnetic field density is constant between two consecutive ones, therefore its flux simply becomes proportional to the product between the value of the magnetic field density and the angle along which the value is valid. In order to describe better this aspect, two cases are presented.

In fig. 7.3a we present the case in which there is no rotor bar in between two stator coils. In this simple yet realistic scenario, we can readily write that:

$$\Phi^s_{\delta,j} = C \cdot B^r_{\delta,k}\left(\theta_{sc_{j+1}} - \theta_{sc_j}\right) \tag{7.7}$$

Instead, in fig. 7.3b the other possible scenario where one rotor bar occurs between two consecutive stator coils is examined. In this case, we can write:

$$\Phi^s_{\delta,j} = C \cdot B^r_{\delta,k}\left(\theta_{rb_{k+1}} - \theta_{sc_j}\right) + C \cdot B^r_{\delta,k+1}\left(\theta_{sc_{j+1}} - \theta_{rb_{k+1}}\right) \tag{7.8}$$

In general, denote n as the number of bars included between two stator coils, considering the two stator coils for which the flux is computed. Equation (7.7) refers to the case $n = 2$, while (7.8) to the case $n = 3$. Such equations can be expressed in matrix form as follows: for (7.7):

$$\begin{bmatrix} \vdots \\ \Phi^s_{\delta,j} \\ \vdots \end{bmatrix} = C \begin{bmatrix} \vdots & & & & & \\ 0 & \cdots & 0 & \Delta\theta_{j,k} & 0 & \cdots 0 \\ \vdots & & & & & \end{bmatrix} \begin{bmatrix} \vdots \\ B^r_{\delta,k} \\ \vdots \end{bmatrix} \tag{7.9}$$

whereas for (7.8):

$$\begin{bmatrix} \vdots \\ \Phi^s_{\delta,j} \\ \vdots \end{bmatrix} = C \begin{bmatrix} \vdots & & & & & & \\ 0 & \cdots & 0 & \Delta\theta_{j,k} & \Delta\theta_{j,k+1} & 0 & \cdots 0 \\ \vdots & & & & & & \end{bmatrix} \begin{bmatrix} \vdots \\ B^r_{\delta,k} \\ B^r_{\delta,k+1} \\ \vdots \end{bmatrix} \tag{7.10}$$

where:

$$\Delta\theta_{j,k} = \begin{cases} \theta_{sc_{j+1}} - \theta_{sc_j} & \text{if } n = 2 \\ \theta_{rb_{k+1}} - \theta_{sc_j} & \text{if } n = 3 \end{cases} \tag{7.11}$$

$$\Delta\theta_{j,k+1} = \theta_{sc_{j+1}} - \theta_{rb_{k+1}} \tag{7.12}$$

Therefore, we can write in matrix form:

$$\boldsymbol{\Phi}^s_\delta = C\boldsymbol{\Theta}_{sr}(\theta_r)\mathbf{B}^r_\delta = \mu_0 C\boldsymbol{\Theta}_{sr}\mathbf{H}^r_\delta \tag{7.13}$$

and - recalling (5.18) with the current notation, $\boldsymbol{\Phi}^s = \mathbf{M}_3\boldsymbol{\Phi}^s_\delta$ and (7.2), $\mathbf{H}^r_\delta = \mathbf{M}_{i,H}\mathbf{i}_r$ - we can write:

$$\boldsymbol{\Phi}^s = \mu_0 C\mathbf{M}_3\boldsymbol{\Theta}_{sr}\mathbf{M}_{i,H} \cdot \mathbf{i}_r \tag{7.14}$$

Finally, we define

$$\mathbf{L}_{mut,s-r}(\theta_r) \triangleq \mu_0 C\mathbf{M}_3\boldsymbol{\Theta}_{sr}\mathbf{M}_{i,H} \tag{7.15}$$

as the mutual stator-rotor matrix that, right-multiplied by the vector of rotor currents in any specific time instant, gives the vector of magnetic fluxes linking the stator coils.

7.2 ROTOR FLUX LINKAGE DUE TO STATOR CURRENTS: $L_{mut,r-s}(\theta_r)$

This chapter wants to describe how the connection between stator currents and rotor flux linkages is achieved. The aim is to find a matrix - that changes with rotor position θ_r - $\mathbf{L}_{mut,r-s}(\theta_r)$ that left-multiplied by the vector of stator coil currents gives rotor flux linkages. In matrix notation:

$$\boldsymbol{\Psi}_r = \mathbf{L}_{mut,r-s}(\theta_r)\mathbf{i}_s \tag{7.16}$$

The procedure involves the following steps:

- First, given a set of stator currents $\mathbf{i}_s$, air-gap magnetic flux density has to be found and expressed as a linear combination of stator currents. This can be achieved by means of (5.13) that is reported here for convenience:

$$\mathbf{H}^s_\delta = \mathbf{M}_{i,H}\mathbf{i}_s \tag{7.17}$$

Note that x^s means that generic quantity is referred integral with the stator. Remember that $\mathbf{H}_\delta^\mathbf{s}$ is a step-wise function which has a constant value between two stator coils.

- Second, the connection between stator and rotor is needed. This is performed in the same fashion as explained in section 7.1.3 but considering to integrate in a stator frame, since (7.17) gives directly a stator-frame quantity. Therefore, rotor bars are considered to change position discretely instant by instant and extreme of integrations are updated at each time step. Such an expression, coming from (7.13), is the result:

$$\mathbf{\Phi}_\delta^\mathbf{r} = C\mathbf{\Theta}_\mathbf{rs}(\theta_r)\mathbf{B}_\delta^\mathbf{s} = \mu_0 C\mathbf{\Theta}_\mathbf{rs}\mathbf{H}_\delta^\mathbf{s} \tag{7.18}$$

- By recalling what already explained in section 6.2.2 regards the connection between air-gap rotor fluxes and rotor lamination flux linkages, we can write the following relation:

$$\mathbf{\Phi}^\mathbf{r} = -\mathbf{M}_3\mathbf{\Phi}_\delta^\mathbf{r} \tag{7.19}$$

- Finally, imposing $n_r = 1$ and substituting (7.17) and (7.18) in (7.19), the resulting expression is found:

$$\mathbf{\Phi}^\mathbf{r} = -\mathbf{M}_3\mu_0 C\mathbf{\Theta}_\mathbf{rs}\mathbf{M}_{\mathbf{i},\mathbf{H}}\mathbf{i}_\mathbf{s} \tag{7.20}$$

so that:

$$\mathbf{L}_{\mathbf{mut,r-s}} = -\mathbf{M}_3\mu_0 C\mathbf{\Theta}_\mathbf{rs}\mathbf{M}_{\mathbf{i},\mathbf{H}} \tag{7.21}$$

8

TRANSIENT MODEL

8.1 MUTUAL MATRICES DERIVATIVE

Once self and mutual connections are found, the last step is to perform time-derivative of mutual matrices. Preliminarily, it is important to investigate how these matrices behave over θ_r and over time.

FILTERING ACTION Figure 8.1 on top shows the connection between stator coil 1 and rotor bar 1 over one mechanical period. This function decreases but not uniformly: in fact, it is constant for some angles, then it decreases linearly and so on. This finds an explanation on the fact that for those angles in which the connection is constant, for instance, there might be no bar between two stator coils and therefore the flux is constant although the rotor keeps moving. Such a function is not differentiable everywhere since for some points the left and right derivative are finite but different in value.

Furthermore, this function is very similar to a jump-discontinuous function, in fact it resembles a saw tooth. For such type of function, Gibbs phenomenon occurs when the Fourier series is made. It consists of large oscillations of its Fourier series partial sum near the jump. This phenomenon presents an overshoot which does not die out as the harmonic order increases, but approaches a finite limit [17]. Then it could be reasonable that performing a Fourier's series expansion without counteracting the Gibbs phenomenon is not the best solution. Further down in this chapter, a qualitative comparison will be given.

Although several solutions are made available, it would be interesting to preserve the original shape of the function considered, smoothing out the noise. One ready method could be to adopt the low-pass Gaussian filter. Further information and direct implementation in MATLAB environment can be found in [18, 19].

Therefore, this approach is adopted. Below in fig. 8.1 it is possible to appreciate a detail of the plot on top. The original function is red-coloured whereas the blue-coloured line represents the Gauss-filtered original function with $\sigma = 10$. This parameter can be tuned ad-hoc and it is related on how strict the filtering action is.

DERIVATIVE In appendix A it is reported how numerical derivatives with truncation error on the second-order are obtained. Adopting such an approach, every matrix element is obtained. In fig. 8.2 two sub-graphs are presented: on top, $L_{rs_{15,1}}$ vs. θ_r is presented. Such an element connects current in stator coil 1 with rotor bar 15 flux. As

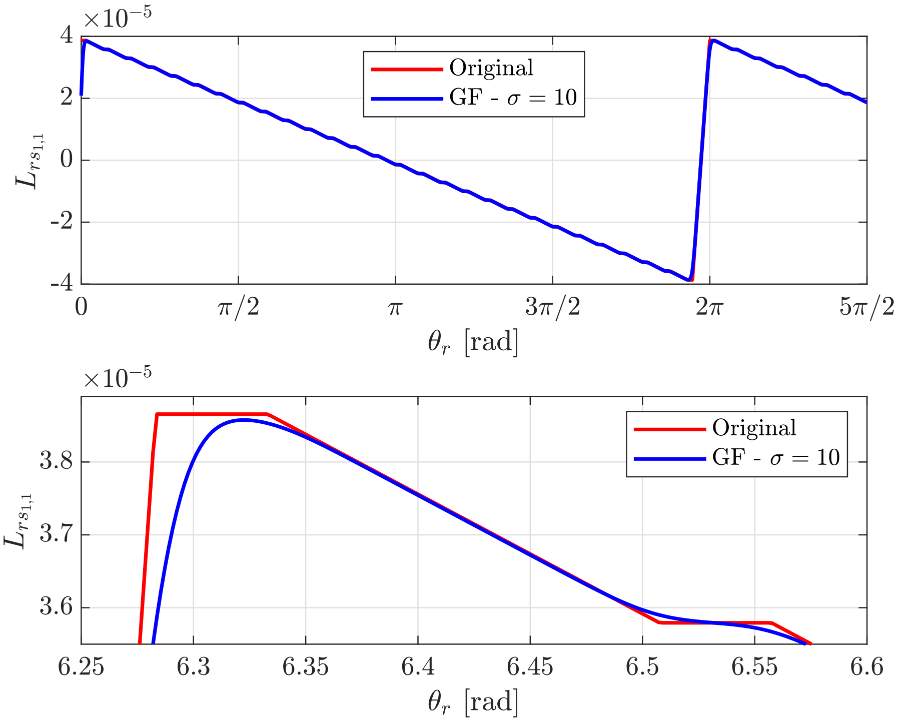

Figure 8.1: Connection between current in stator coil 1 and flux in rotor bar 1 over rotor position.

already explained, such a function is Gauss-filtered and then numerically derived. The derivative is shown in the sub-graph below. It is possible to notice the oscillations and the peak corresponding to the position where rotor bar 15 and stator coil 1 are aligned one in front of the other.

A second important aspect is how to go from spacial-derivative to time-derivative. The definition of mechanical angular speed ω_m is the following:

$$\omega_m = \frac{d\theta_r}{dt} \tag{8.1}$$

where θ is the rotor angular position. It is possible to write the following relation for a generic quantity x, without focusing on the mathematical implications:

$$\frac{dx}{dt} = \frac{\partial x}{\partial \theta_r}\frac{\partial \theta_r}{\partial t} \tag{8.2}$$

which means the following relation holds:

$$\frac{dx}{dt} = \omega_m \frac{dx}{d\theta} \tag{8.3}$$

and, since in our assumptions rotor position varies linearly over time, ω_m is a constant number and (8.3) becomes a simple multiplication.

In such a way, time-derivative of mutual matrices are obtained.

As a final consideration, a narrow time-interval of matrix element $L_{rs_{1,1}}$ is shown in fig. 8.3, where the relation $\theta_r = \omega_m t$ has been used

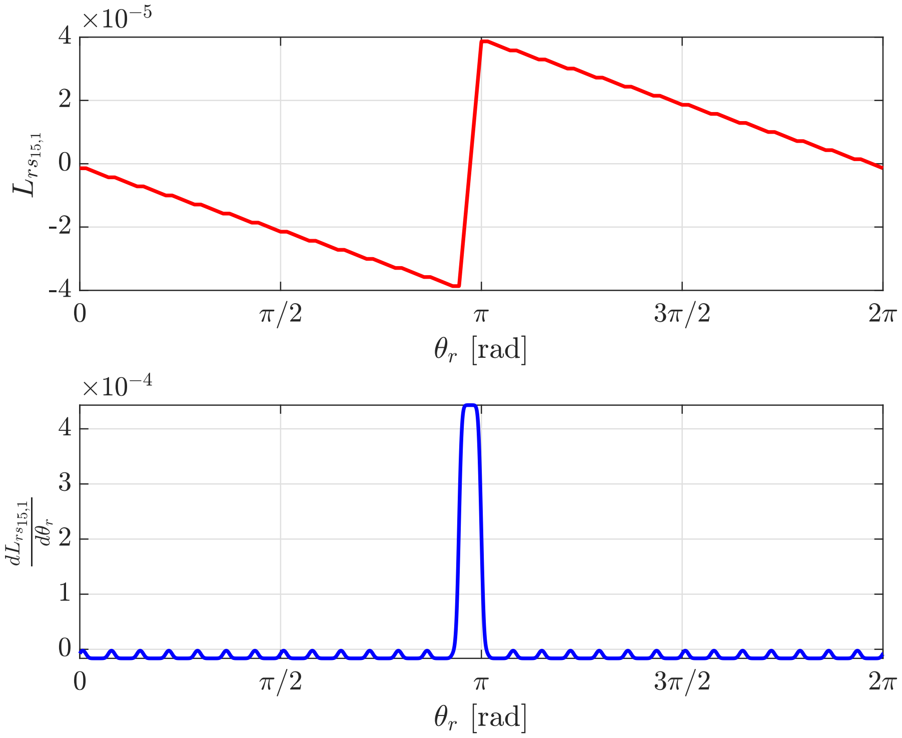

Figure 8.2: Connection between stator coil 1 current and rotor bar 15 flux over rotor position, and its angular derivative.

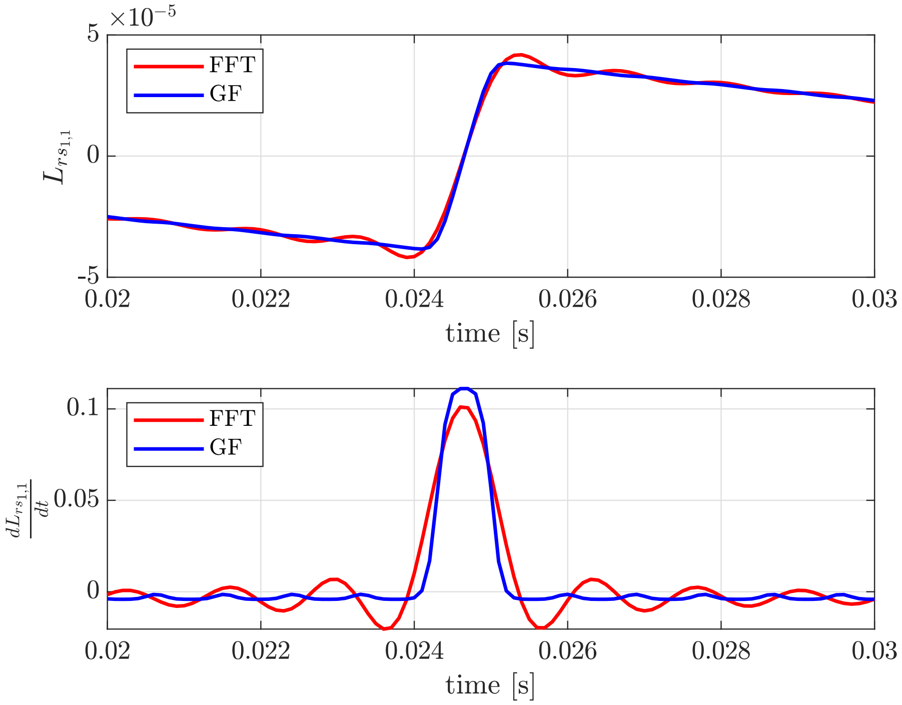

Figure 8.3: Comparison between Fourier's series expansion and Gauss-filtering of $L_{rs_{1,1}}$ and its time-derivative.

to translate angles into time values. It is also plotted a comparison between the Gauss-filtered function (denoted in the figure as GF) and the aforementioned Fourier's series expansion truncated on the $h = Q_r/2$.

8.2 MATRIX MODEL

Once matrix are derived and their derivatives computed, (8.4) can be written and solved both for currents and voltages. It is here reported.

$$\begin{bmatrix} \mathbf{V_s} \\ 0 \end{bmatrix} = \begin{bmatrix} \mathbf{R_s} & \frac{d\mathbf{L_{mut,s-r}}}{dt} \\ \frac{d\mathbf{L_{mut,r-s}}}{dt} & \mathbf{R_r} \end{bmatrix} \begin{bmatrix} \mathbf{i_s} \\ \mathbf{i_r} \end{bmatrix} + \begin{bmatrix} \mathbf{L_s} & \mathbf{L_{mut,s-r}} \\ \mathbf{L_{mut,r-s}} & \mathbf{L_r} \end{bmatrix} \begin{bmatrix} \frac{d\mathbf{i_s}}{dt} \\ \frac{d\mathbf{i_r}}{dt} \end{bmatrix} \tag{8.4}$$

Such a system of $Q_r + Q_s$ DAEs can be solved directly if currents are supplied.

If this system is solved for currents given voltages, as it is in reality since a motor is supplied with voltages and not currents, a numerical method is needed. In order to enhance solver rapidity, embedded Ordinary Differential Equations (ODEs) solvers found in MATLAB are not considered and the $\theta-$method is adopted [20].

This solver is centred on the approximation of an integral with the linear combination of the values the function has at the extreme of the time interval, weighted with the parameter θ.

By using the mean value theorem for definite integrals, we can write:

$$\int_{t_k}^{t_{k+1}} f(t)dt = (t_{k+1} - t_k) f(t^*) = \Delta t f(t^*) \tag{8.5}$$

which means that, if f is a continuous function within the interval, it exist one point t^* in the interval so that the integral is equal to the time interval multiplied by the function value at that point. Since no information is given about how to find such a point, the $\theta-$method assumes it is a linear combination of values at the extreme of the time interval:

$$\int_{t_k}^{t_{k+1}} f(t)dt \simeq \Delta t \left[\theta f(t_{k+1}) + (1-\theta) f(t_k)\right] \tag{8.6}$$

Therefore, if (10.1) is written in simplified form as:

$$M_1 x + M_2 \frac{dx}{dt} = s(t) \tag{8.7}$$

the method provides how to find the solution vector at time instant t_{k+1} given the solution at t_k:

$$\left[\theta M_{1_{k+1}} + \frac{M_{2_{avg}}}{\Delta t}\right] x_{k+1} = \left[-(1-\theta) M_{1_n} + \frac{M_{2_{avg}}}{\Delta t}\right] x_k + \\ + \theta s_{k+1} + (1-\theta) s_k \tag{8.8}$$

where $M1_k$ refers to $M1$ at time instant t_k and $M2_{\text{avg}}$ is the average of $M2$ between t_k and t_{k+1}.

It can be proved that, if $\theta \in [1/2, 1]$, the method is unconditionally asymptotic stable, therefore this parameter is chosen within this range.

Part II

ANALYTICAL MODEL DERIVED FROM FINITE ELEMENT ANALYSIS

9

PARAMETER DERIVATION BY FINITE ELEMENT ANALYSIS

9.1 FINITE ELEMENT MODEL

9.1.1 *Model description*

9.1.1.1 *Introduction and concept*

The goal is to use the Finite Element Analysis (FEA) in order to derive inductances through which system of equations in (9.1) can be solved, both for currents and voltages.

$$\begin{bmatrix} \mathbf{V_s} \\ \mathbf{V_r} \end{bmatrix} = \begin{bmatrix} \mathbf{R_s} & \frac{d\mathbf{L_{mut,s-r}}}{dt} \\ \frac{d\mathbf{L_{mut,r-s}}}{dt} & \mathbf{R_r} \end{bmatrix} \begin{bmatrix} \mathbf{i_s} \\ \mathbf{i_r} \end{bmatrix} + \begin{bmatrix} \mathbf{L_s} & \mathbf{L_{mut,s-r}} \\ \mathbf{L_{mut,r-s}} & \mathbf{L_r} \end{bmatrix} \begin{bmatrix} \frac{d\mathbf{i_s}}{dt} \\ \frac{d\mathbf{i_r}}{dt} \end{bmatrix} \tag{9.1}$$

In the classical analysis of electrical machines, a per-phase approach is used. It means that parameters can be derived by considering one phase at a time, and then - by superposition of effects - other phases are considered.

The underlying aspect of such an approach is that, when a phase is supplied with current, if we consider a circumference centred in the middle of the shaft and with a radius $r = r_{s,out} - r_{s,in}$ (i.e. passing in the middle of the stator yoke), and we extrude it in the z dimension for the length of the machine, we get a surface that encloses a zero net current. In fact, there are at least two slots belonging to the same phase and conducting opposite currents, because they are physically connected in series. Thus, Ampère's law can be applied considering iron ideal and neglecting its reluctance, and classical theory of electrical machines can be used.

Nevertheless, when it comes to the WICSC machine, the concept of phase has to be put apart, at a first stage. In this machine, slots are independently supplied with currents and by doing it one at a time, the condition above described is no longer valid. Therefore, the derivation of parameters that will be presented in this part depends on iron reluctance, and ultimately on leakages.

The approach used is the following: a single coil or bar is excited with unit current. In order to properly define flux paths, there has to be an opposite current defining a loop. The opposite current is therefore supplied in the external coil for the stator current, and in the shaft itself for the rotor one.

Given such electrical inputs, magnetic fluxes and magnetic flux linkages are computed in a FE environment (COMSOL Multiphysics®) either by integrating the magnetic flux density in the proper direction, or by difference of magnetic vector potential. By recalling the relationship between flux linkage and current:

$$\Psi = Li \tag{9.2}$$

and that a unit current is used, the inductance is obtained. Such considerations are done in matrix form.

The approach is carried out by assuming material linearity. As a consequence, superposition of effects, symmetry and value scaling is legit. Therefore, only one slot or bar is examined, and the full set of parameters is derived by means of geometrical symmetries considerations.

Once inductances are obtained, they do not depend on the value of current because of linearity, so the linear relationship between current and flux is obtained. This is clearly a limit of such an approach, since saturation is not taken into account.

Future improvements may try to address this aspect, mapping parameters for different values of input currents.

9.1.1.2 *Modification of the geometry*

As introduced above, linearity is a crucial hypothesis in this model.

Unfortunately, the squirrel cage rotor of WICSC machine involves interior deep bars. They are used - along with a double cage rotor - to enhance starting performances of induction motors.

In fact, at the motor start-up, rotor frequency is the same as the supply frequency. The bottom part of the bar is designed to have lower resistance and higher inductance than the top part. Therefore, the current density will be higher in the top part than in the bottom part. This results in an increase of the equivalent resistance and a decrease of the leakage inductance, and therefore the resulting starting torque is higher. As the rotor speeds up, the induced frequency decreases and the current density will move towards the upper part of the bar, characterized by lower resistance.

The drawback of such a design is the same that can be found in IPMs motors. When a rotor bar is excited with some current, the resulting magnetic flux finds a very low reluctance path around the bar itself, and therefore only a very small portion of flux penetrates the air-gap, a leakage portion. As the saturation increases, more and more flux will penetrate the air-gap allowing the normal behaviour of the machine. This aspect does not occur if linearity is considered. Therefore, a modification in the geometry has to be introduced.

For this motivation, the upper part of each rotor bar is decided to be opened, i.e. iron is removed in that region in favour of air, with a much higher reluctance.

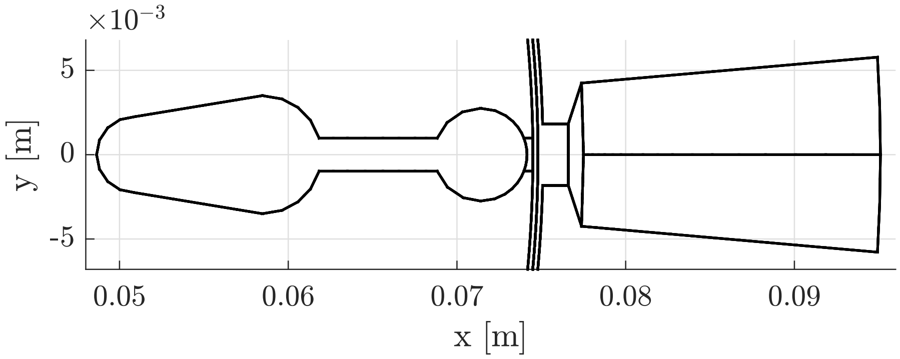

Figure 9.1: Detail of the rotor bar with the artificial opening and the stator slot.

This will only approximate the saturation effects in terms of air-gap flux penetration, and it is a simplification that is valid only in the initial stage of the model.

Future improvements will consider the real geometry with real materials. Figure 9.1 depicts a closer detail of the rotor deep bar with the artificial opening, whose width is assumed to be the same as the one of the rectangular part of the bar itself. It is also possible to note the stator slot width, the opening and the wedge.

9.2 STATOR FLUX LINKAGE DUE TO STATOR CURRENT: L_s

9.2.1 *Quantities definition*

We define $\mathbf{L_s}$ as the matrix that links the stator coil currents with the stator coil flux linkages induced by those currents:

$$\mathbf{\Psi_s} = \mathbf{L_s i_s} \tag{9.3}$$

Therefore, it is crucial to properly define such quantities.

$\mathbf{i_s}$ is a row vector with size $Q_s \times 1$ containing the instant values of currents in all the Q_s stator slots.

$\mathbf{\Psi_s}$ is a row vector with the same size as $\mathbf{i_s}$ containing the instant value of flux linking the different Q_s coils.

Recalling the definition of the magnetic vector potential, $\mathbf{B} = \nabla \times \mathbf{A}$, and considering that $\mathbf{A}$ has only z component in the two-dimensional problem, we can compute the magnetic flux as:

$$\Phi_s = \iint_S \mathbf{B}_\delta \cdot \hat{\mathbf{n}}\, dS = \oint_{\partial S} \mathbf{A} \cdot \hat{\mathbf{r}}\, dr = L_a \left(A_z(x_1, y_1) - A_z(x_2, y_2) \right) \tag{9.4}$$

and the flux linkage, which links the n_s turns, as:

$$\Psi_s = n_s \Phi_s \tag{9.5}$$

In WICSC machine, the magnetic flux of slot j-th is flowing between

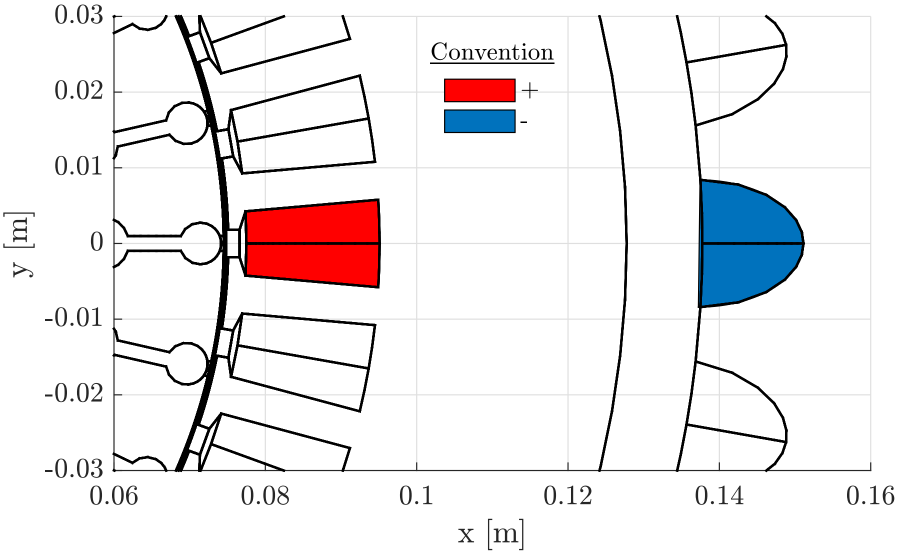

Figure 9.2: Elements to consider for the flux linkage.

the slot j-th itself and the external coil radially aligned. Equation (9.4) can be further expressed by considering the difference between the average values of A_z in the coil area. Figure 9.2 shows in red the slot area, conventionally associated with positive currents, and in blue the external return coil, with the convention of negative coil.

Based on these aspects, (9.4) can be expressed as:

$$\Phi_s = L_a \left(\frac{1}{S_+} \iint_{S_+} A_z \, dS - \frac{1}{S_-} \iint_{S_-} A_z \, dS \right) \tag{9.6}$$

where S_+ and S_- are respectively the red and blue area of fig. 9.2

9.2.2 L_s *computation*

Having introduced the electrical and magnetic quantities, in this section it is explained how the matrix $\mathbf{L_s}$ is built.

- In the first place, coil 1 is supplied with unit current. This means that stator slot 1 has a positive current (i.e. pointing outwards the paper) and the respective external coil the return and therefore negative current.
- Under this condition of excitation, stator flux linkages are computed for all Q_s stator coils by means of (9.5) and (9.6).
- In such a way, the first column of $\mathbf{L_s}$ is computed.
- In the second place, symmetry is used. This means that the flux linking coil j due to current in coil j has to be the same as the flux linking coil k due to current in coil k. The same reasoning applies for the mutual terms, since the flux linking coil i due to

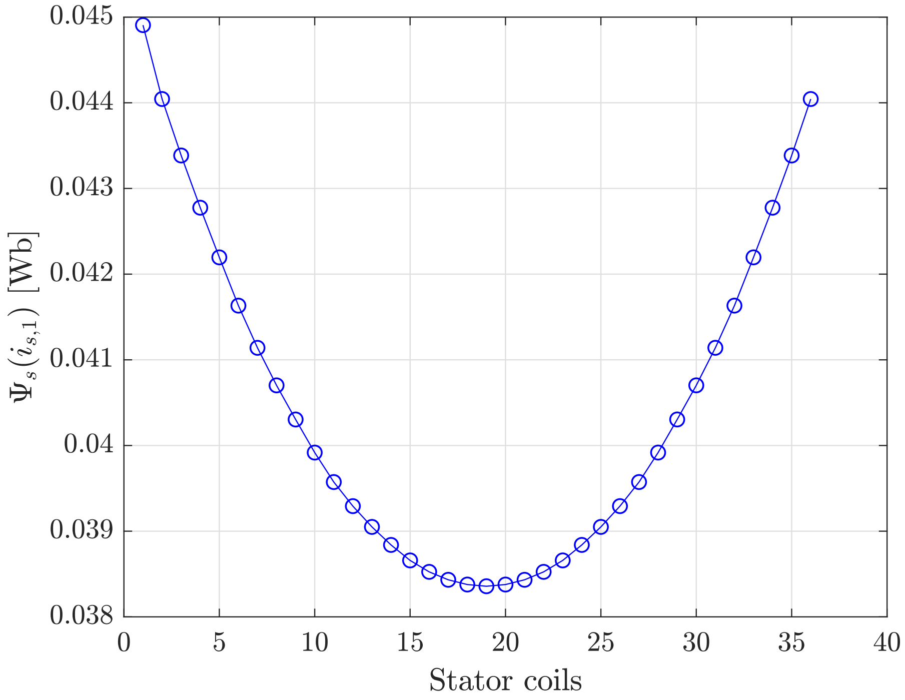

Figure 9.3: Stator slots flux linkages induced by current in stator coil 1.

current in coil $i-1$ is the same as the flux linking coil $i+1$ due to current in coil i. Furthermore, flux linking coil t due to current in coil s is the same as the flux linking coil s due to current in coil t. The result is that $\mathbf{L_s}$ has to be symmetrical, with identical elements on the diagonal, i.e it is a symmetrical Toeplitz matrix or diagonal-constant matrix.

- Based on the considerations of the previous point, the other columns on the matrix are built.

9.2.3 *Results*

Figure 9.3 shows the flux linkages - for the Q_s stator coils - induced by a unit current in stator coil 1, $i_{s,1}$. These values are therefore the first column and the first row of $\mathbf{L_s}$.

These absolute values are dependent of several aspects, including the relative permeability of stator iron. The lower this parameter is, the lower flux linkages are, given the same current.

Figure 9.4 shows the contour lines of the z component of the magnetic vector potential, A_z produced by the set of unit currents in coil 1, along with the conceptual representation of those currents.

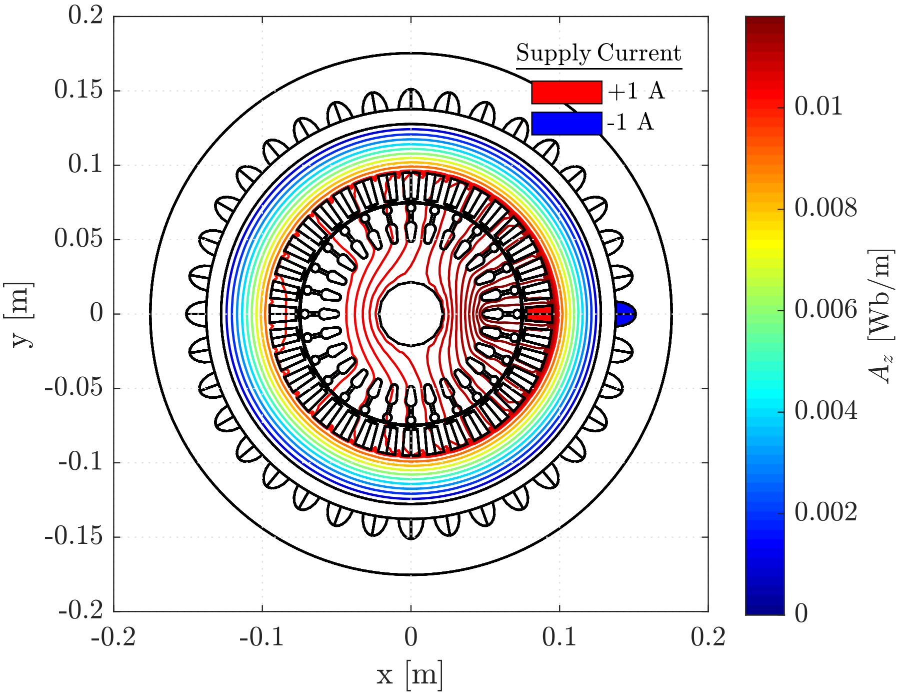

Figure 9.4: A_z contour lines induced by current in stator slot 1.

9.3 ROTOR FLUX LINKAGE DUE TO ROTOR CURRENT: L_r

9.3.1 *Quantities definition*

Following the same fashion of $\mathbf{L_s}$, $\mathbf{L_r}$ is defined as the matrix that gives a linear connection between rotor bar currents and induced rotor flux linkages, or in matrix notation:

$$\mathbf{\Psi_r} = \mathbf{L_r i_r} \tag{9.7}$$

Vector current $\mathbf{i_r}$ is a $Q_r \times 1$ matrix that contains the value of instantaneous currents for a specific time instant, $\mathbf{\Psi_r}$ has already been introduced in 6.2.2 and it is the tangential flux in the rotor lamination. To compute such a quantity, different approaches are adopted and they will be listed below.

9.3.2 L_r *computation*

The procedure adopted to extract $\mathbf{L_r}$ resembles the one described in the previous section.

- For what concern system inputs, rotor bar 1 is supplied with unit current. This is not sufficient to define a current loop, since there is a need for the supplied current to return. Therefore, it is assumed that the entire shaft conduces the return current, because considering only an inner portion of the shaft, surrounded by a magnetic insulating material, can affect flux paths.

- Under this excitation condition, rotor bars flux linkages are computed. This is carried out in three different ways.
    1. By means of the line integral of B_ϕ. First, a connection between the innermost part of each bar and the centre of the shaft is considered. Extruded in the z direction, a surface is defined and the flux linkage is the integral of magnetic flux density on that surface. Since a positive rotor bar current induces a counter-clockwise flux, thus negative according to the tangential reference system, a -1 is introduced to get a positive slot inductance.
    2. By means of (9.6) where S_+ is rotor bar 1, and S_- corresponds to the shaft. This definition has the right sign by itself.
    3. By means of direct output from FEA , since a coil is defined. It can be measured that the direct output from FEA is not a flux linkage but the value of average A_z in each rotor bar multiplied by the active length. Therefore, it is not considered in the next discussion.

  One could notice that, using methods of points 1 and 2, also the flux component that circulates in the rotor lamination and in the shaft (*DC component of rotor flux*) is accounted for. In fact, by using this approach, the result is shifted by a DC value. By removing it, part of flux penetrating the air-gap and leakages are found.

- In such a way, the first column of $\mathbf{L_r}$ is obtained.

- Based on what already explained for $\mathbf{L_s}$, symmetry is used and the other columns are obtained simply by translating the first.

9.3.3 *Results*

In the first place, a comparison of different methods to derive $\mathbf{\Psi_r}$ is given.

Figure 9.5 represents the other two ways: the red plot shows flux linkage values by means of difference of average value of A_z in the bar and the shaft. The blue line instead depicts the same quantity obtained by means of surface integral of magnetic flux density. In the sub-graph below, the relative error between these two aforementioned approaches is depicted. This function is defined as:

$$\text{error} = 1 \times 10^3 \frac{\left| L_a \int B_\phi dS - L_a \left[A_z(S_+) - A_z(S_-)\right] \right|}{L_a \int B_\phi dS} \tag{9.8}$$

and it is essentially negligible. Again, the absolute value of magnetic flux depends on several aspects, and the iron relative permeability is a crucial one. Nevertheless, the absolute value of $\mathbf{L_r}$ elements is not

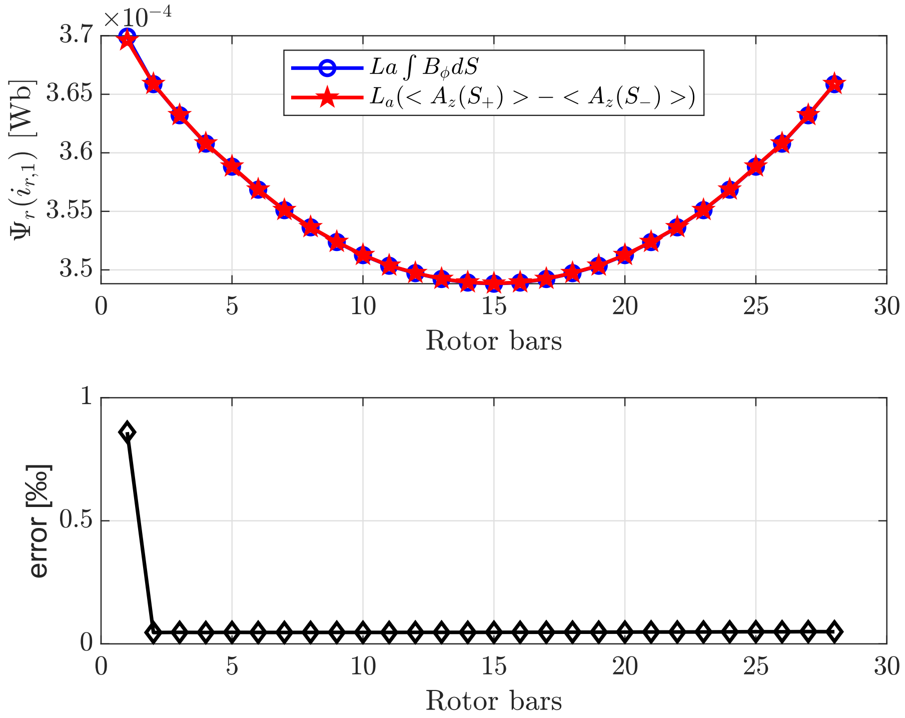

Figure 9.5: Rotor bars flux linkages induced by current in rotor bar 1.

important by itself since what matters is a linear combination of its rows with the column vector of instantaneous currents, whose sum is always zero for the operation assumption. This condition implies that any DC offset in $\mathbf{L_r}$ has no active role in determining $\mathbf{\Psi_r}$.

As a consequence, the effect of different iron relative permeabilities is mitigated, because what is important is differences of fluxes and not their absolute values.

In fig. 9.6, contour lines of A_z are shown. The supplied current is remarked in red (positive) and blue (negative).

9.4 STATOR FLUX LINKAGE DUE TO ROTOR CURRENT: L_{sr}

This matrix links stator coil flux linkages $\mathbf{\Psi_s}$ induced by rotor bar currents, $\mathbf{i_r}$. It represents then the connection between the rotor and the stator. In matrix notation:

$$\mathbf{\Psi_s} = \mathbf{L_{sr}} \mathbf{i_r} \tag{9.9}$$

Taking advantages of methods explained in sections 9.2 and 9.3, by considering the same input of section 9.3 and the same post-process flux computation of section 9.2, stator slot flux linkages due to rotor currents are derived. In particular, few aspects must be remarked.

- The analysis only considers a unit current in the first rotor bar and stator slot 1 flux linkage. This value is a function of rotor position θ_r and therefore a transient simulation is in use.

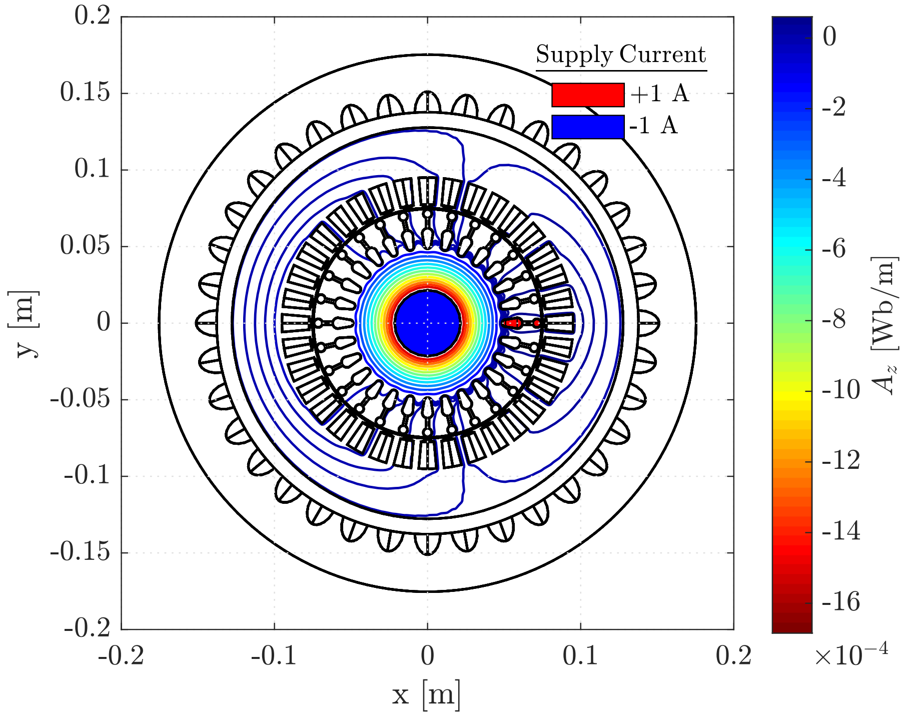

Figure 9.6: A_z contour lines induced by current in rotor bar 1.

- As a consequence, the rotor is imposed to rotate at a fixed speed, which is chosen to be $n = 150\,\mathrm{rpm}$. This value is low, it corresponds to a mechanical frequency $f_m = 2.5\,\mathrm{Hz}$, and it allows, coupled with a simulation time $t_{sim} = 0.8\,\mathrm{s}$, to get flux linkage information more than 11 times per mechanical degree, for a total of 4000 points per revolution. In order to exclude the first instants when the current is not at steady-state and which could result in a wrong value of flux, the actual quantity Ψ_1^s is stored during the second mechanical revolution. Then, discrete points are interpolated to create a continuous function; the method chosen is to use a piece-wise cubic interpolating function.

  Figure 9.7 shows the first element of the first row, i.e. $L_{sr_{1,1}}$ at different rotor positions. In can be inferred, as it should be, that the coupling stator-rotor is higher when the bar is close to the stator coil and it decreases gradually reaching the minimum when the rotor bar is mechanically opposite to the stator coil.

- Once $L_{sr_{1,1}}(\theta_r)$ is obtained, the other elements of the matrix can be readily obtained by means of symmetry considerations.

  In fact, when the rotor bar 1 is in position $\theta_r = 2\pi/Q_s$, stator coil 2 links the same flux that stator coil 1 links when $\theta_r = 0$. This means that $L_{sr_{2,1}}(\theta_r)$ is lagging behind $L_{sr_{1,1}}(\theta_r)$ by $\Delta\theta_r = 2\pi/Q_s$.

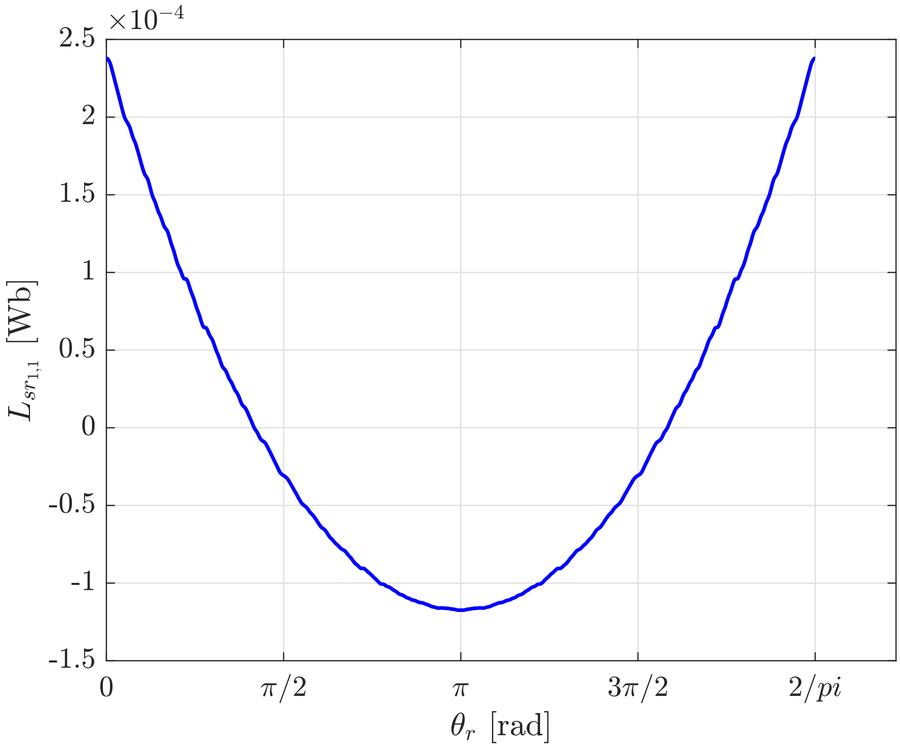

Figure 9.7: $L_{sr_{1,1}}$ versus θ_r.

Equivalently, at standstill rotor, when rotor bar 2 is supplied with unit current, it induces a certain flux linking stator coil 2. This flux has the same value of stator coil 1 flux linkage when rotor is rotated by $-2\pi/Q_r$ (clockwise). In this case, $L_{sr_{1,2}}(\theta_r)$ is the same function as $L_{sr_{1,1}}(\theta_r)$ but phase-shifted by $\Delta\theta_r = 2\pi/Q_r$.

If we rename matrix elements so that $L_{i,j} = L_{sr_{i,j}}$, this symmetry considerations result in (9.10).

$$\mathbf{L_{sr}} = \begin{bmatrix} L_{1,1}\left(\theta_r - 0\frac{2\pi}{Q_s}\right) & L_{1,1}\left(\theta_r + 1\frac{2\pi}{Q_r} - 0\frac{2\pi}{Q_s}\right) & \dots & L_{1,1}\left(\theta_r + (Q_r-1)\frac{2\pi}{Q_r} - 0\frac{2\pi}{Q_s}\right) \\ L_{1,1}\left(\theta_r - 1\frac{2\pi}{Q_s}\right) & L_{1,1}\left(\theta_r + 1\frac{2\pi}{Q_r} - 1\frac{2\pi}{Q_s}\right) & \dots & L_{1,1}\left(\theta_r + (Q_r-1)\frac{2\pi}{Q_r} - 1\frac{2\pi}{Q_s}\right) \\ \vdots & \vdots & \vdots & \vdots \\ L_{1,1}\left(\theta_r - (Q_s-1)\frac{2\pi}{Q_s}\right) & L_{1,1}\left(\theta_r + 1\frac{2\pi}{Q_r} - (Q_s-1)\frac{2\pi}{Q_s}\right) & \dots & L_{1,1}\left(\theta_r + (Q_r-1)\frac{2\pi}{Q_r} - (Q_s-1)\frac{2\pi}{Q_s}\right) \end{bmatrix} \tag{9.10}$$

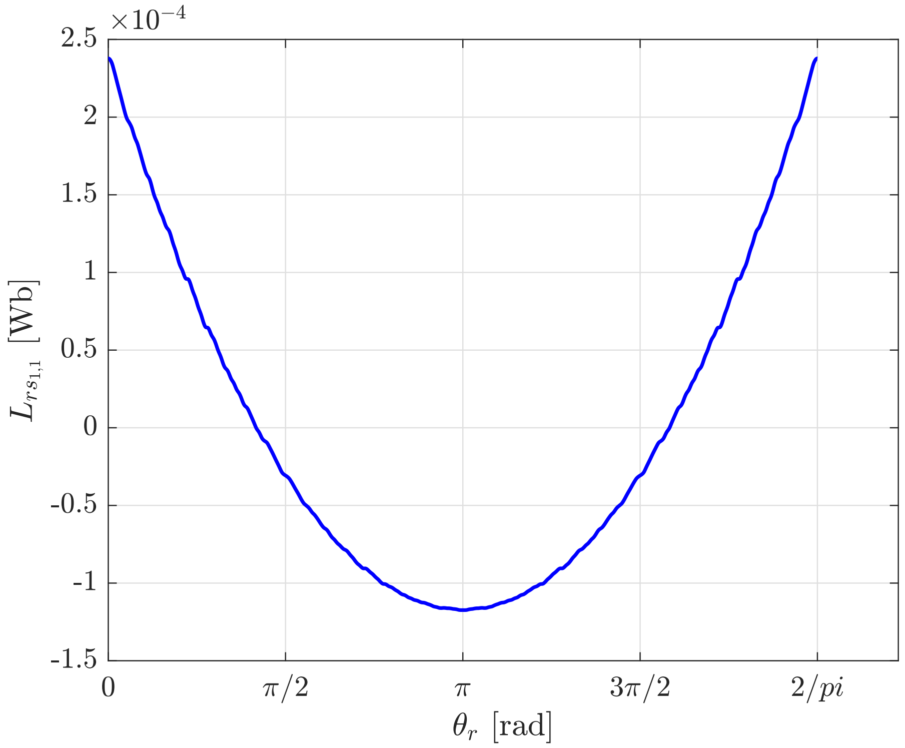

Figure 9.8: $L_{rs_{1,1}}$ versus θ_r.

9.5 ROTOR FLUX LINKAGE DUE TO STATOR CURRENT: L_{rs}

This matrix links rotor bar flux linkages $\mathbf{\Psi_r}$ induced by stator slot currents, $\mathbf{i_s}$. It represents then the connection between the stator and the rotor in the same fashion as $\mathbf{L_{sr}}$. In matrix notation, in this case we can write:

$$\mathbf{\Psi_r} = \mathbf{L_{rs}}\mathbf{i_s} \tag{9.11}$$

Taking advantages of methods explained in sections 9.2 and 9.3, by considering the same input of section 9.2 and the same post-process flux computation of section 9.3, rotor bar flux linkages due to stator currents are derived. Considerations about the method used can be found in section 9.4. Figure 9.8 shows the first element of the first row, i.e. $L_{rs_{1,1}}$ at different rotor positions. It can be inferred what already experienced, as it should be, that the coupling stator-rotor is higher when the bar is close to the stator coil and it decreases gradually reaching the minimum when rotor bar is mechanically opposite to stator coil. Moreover, its trend over time is the same as $L_{sr_{1,1}}$, thus it can be stated that $\mathbf{L_{sr}}$ and $\mathbf{L_{rs}}$ have the same elements on the main diagonal.

Other matrix elements can be inferred from the $L_{rs_{1,1}}$ by means of symmetry considerations. When stator coil 1 is supplied with current, at $\theta_r = 0$ the first rotor bar is in front of the coil and a certain flux links this bar. This value is the same that links rotor bar 2 when $\theta_r = -2\pi/Q_r$ (positive phase-shift, i.e. $L_{rs_{2,1}}(\theta_r)$ is lagging in front of $L_{rs_{1,1}}(\theta_r)$). On the other hand, when stator coil 2 is supplied with current, at rotor rotates, when $\theta_r = 2\pi/Q_S$, rotor bar 1 is linked by the same flux that linked it at $\theta_r = 0$.

In other words, $\mathbf{L_{sr}}$ and $\mathbf{L_{rs}}$ are one the transpose of the other, i.e. $\mathbf{L_{sr}} = \mathbf{L_{rs}}^{T}$.

10

TRANSIENT MODEL

10.1 MATRIX DERIVATIVE

The final step to achieve (9.1) is to perform the derivative of mutual matrices. Regarding this aspect, it is important on a preliminary level to analyse how elements of such matrices behave over time. $\mathbf{L_{rs}}$ will be considered.

MECHANICAL DEPENDENCY Consider for instance the fifteenth element of the first row, $\mathbf{L_{rs_{1,15}}}$ which is connecting the stator current in coil 15 with the flux linkage of the first rotor bar. Figure 10.1 shows in red how this parameter changes at different rotor positions. In blue its derivative is computed. In appendix A it is reported how numerical derivatives with truncation error on the second-order are obtained.

The red-coloured line is the result of the method in section 9.5. As it is noticeable, such a function is not smooth and its derivative can not be considered a straight line, although the function resembles a parabola. This is due to both numerical effects in FE solver and to slot openings effects. Therefore, its derivative is very *noisy* and some actions are needed. One first solution to this problem is to approximate the derivative with its Fourier's series, truncated to a specific harmonic order, which is chosen corresponding to a half of the stator slots $h = Q_s/2$. As already noticed in section 8.1, the derivative resembles a jump-discontinuous function, for which Gibbs phenomenon occurs. Since it would be interesting to preserve the original shape of the function considered, smoothing out the large oscillations is the only action to perform, in this first level of analysis. One ready method already exploited in section 8.1 is the low-pass Gaussian filter.

In fig. 10.1, the result of Gauss-filtering the derivative is visible: the green-coloured line represents the Gauss-filtered function with $\sigma = 20$. This parameter can be tuned ad-hoc and it is related to how strict the filtering action is.

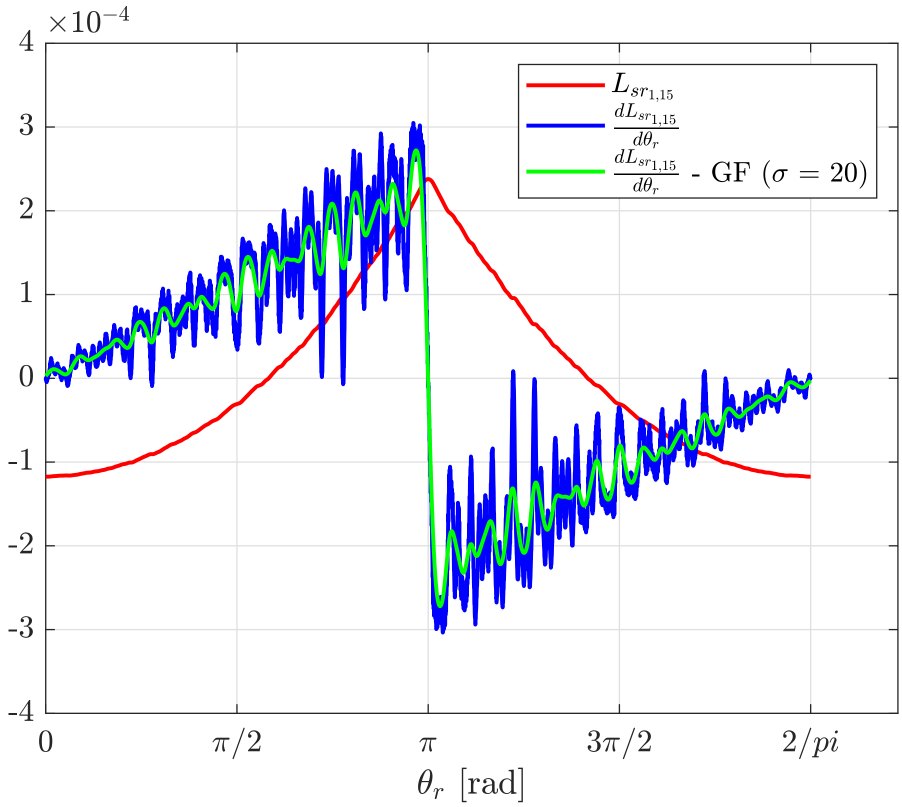

Figure 10.1: Connection between rotor bar 15 and stator coil 1, its derivative and Gauss'filtering of the derivative.

10.2 FEA EQUATION

Once matrix are derived and their derivatives computed, (9.1) can be written and solved both for currents and voltages. It is here reported.

$$\begin{bmatrix} \mathbf{V_s} \\ 0 \end{bmatrix} = \begin{bmatrix} \mathbf{R_s} & \frac{d\mathbf{L_{mut,s-r}}}{dt} \\ \frac{d\mathbf{L_{mut,r-s}}}{dt} & \mathbf{R_r} \end{bmatrix} \begin{bmatrix} \mathbf{i_s} \\ \mathbf{i_r} \end{bmatrix} + \begin{bmatrix} \mathbf{L_s} & \mathbf{L_{mut,s-r}} \\ \mathbf{L_{mut,r-s}} & \mathbf{L_r} \end{bmatrix} \begin{bmatrix} \frac{d\mathbf{i_s}}{dt} \\ \frac{d\mathbf{i_r}}{dt} \end{bmatrix} \tag{10.1}$$

Such system of $Q_r + Q_s$ DAEs can be solved directly if currents are supplied.

If this system is solved for currents given voltages, as it is in reality, a numerical method is needed. The $\theta-$ method is adopted also in this model, and it is valid what already explained in section 8.2

Part III

VALIDATION OF ANALYTICAL METHOD

11

METHODS COMPARISON FOR MATRIX DERIVATION

In this section, comparison of methods is presented. The reference is a FE simulation performed in Comsol Multiphysics environment, with linear materials and same inputs as the analytical ones.

11.1 STATOR SELF CONNECTION: L_s

First, validity of methods to derive $\mathbf{L_s}$ is given. The simulation considers two sub-cases for what regards input current:

- In the first, the easiest case is considered: coil 1 is supplied with a positive unit current (i.e $i_{sc,1} = 1\,A$) and the physically opposite coil, coil 19, with negative unit current. All other stator coils are kept to zero current as are the rotor bars.
- In the second case, a set of sinusoidally distributed currents is given as input to the system. Therefore, setting $I_{rms} = 3\,A$,

$$i_{sc,j} = \sqrt{2}I_{rms}\sin\left(\frac{2\pi}{Q_s}(j-1)\right) \text{ where } j = 1, 2, \dots, Q_s \tag{11.1}$$

The test aims at comparing Ψ_j^s, $j = 1, 2, \dots, Q_s$ given by different methods, in particular:

GEOMETRICAL ANALYTICAL APPROACH: The vector of stator coil flux linkages is given by the linear system $\mathbf{\Psi_s} = \mathbf{L_s i_s}$ in which $\mathbf{L_s}$ is computed as descrived in chapter 5.

FE ANALYTICAL APPROACH: The same of the previous point but with $\mathbf{L_s}$ obtained from section 9.2.

FE SIMULATION: Reference independent FE simulations.

Results are showed in fig. 11.1, respectively in fig. 11.1a for the first sub-case and in fig. 11.1b for the second.

As it is possible to notice, no appreciable difference between the two analytical methods and the FE reference simulation occurs, and this confirms the validity of both derivations of such matrix.

11.2 ROTOR SELF CONNECTION: L_r

Second, methods to derive $\mathbf{L_r}$ are tested. As for $\mathbf{L_s}$, the comparison is carried out by taking into account two sub-cases for what regards the input rotor currents:

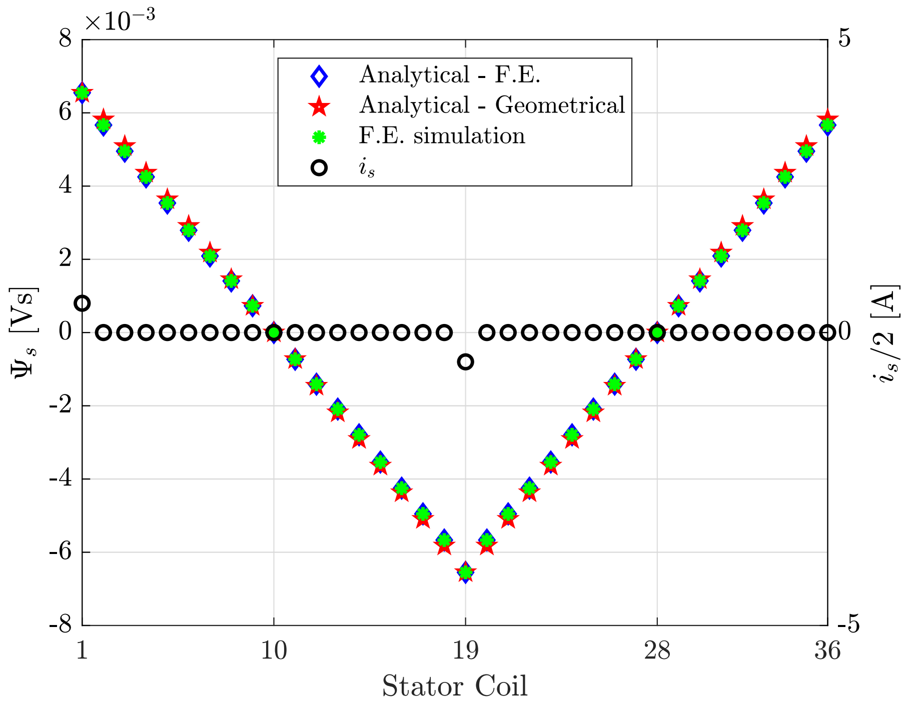

(a) First case: $i_{sc,1} = 1\,A$ and $i_{sc,19} = -1\,A$

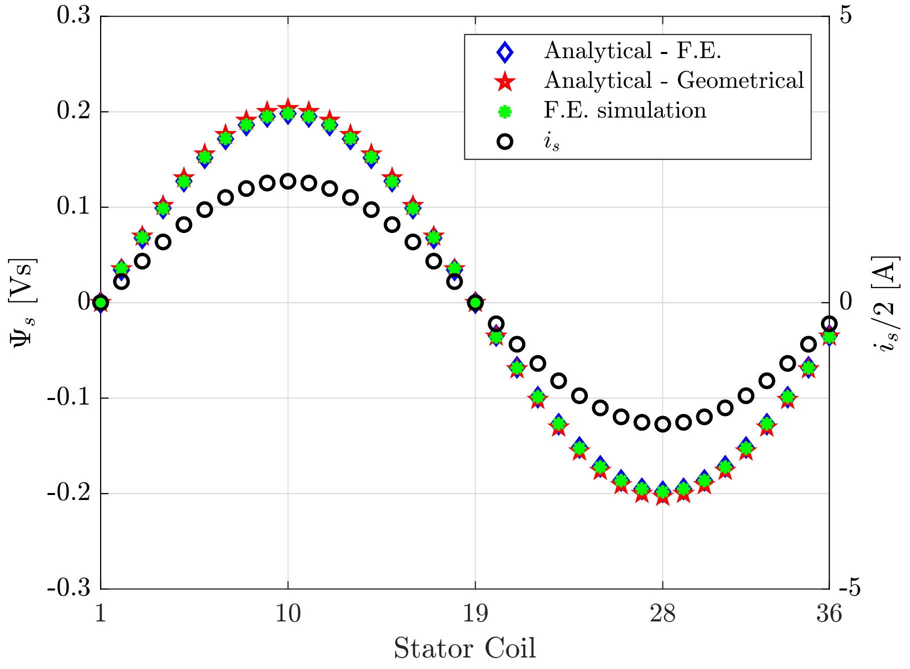

(b) Second case: sinusoidally distributed currents.

Figure 11.1: Comparison of different methods in terms of stator coil flux linkage predictions.

- In the first, rotor bar 1 is supplied with a positive current (i.e $i_{rb,1} = 100\,\mathrm{A}$) and the physically opposite bar, bar 15, with negative current of the same magnitude. All the other rotor bars are kept to zero current as are the rotor bars.
- In the second case, a set of sinusoidally distributed rotor bar currents is given as input to the system. Therefore, setting $I_{peak} = 100\,\mathrm{A}$,

$$i_{rb,j} = I_{peak} \sin\left(\frac{2\pi}{Q_r}(j-1)\right) \text{ where } j = 1, 2, \dots, Q_r \qquad (11.2)$$

In the same fashion of stator self connection, test in this section aims at comparing $\Psi_j^r, j = 1, 2, \dots, Q_r$ given by different methods. In particular:

Geometrical analytical approach: the vector of rotor bar flux linkages is given by the linear system $\mathbf{\Psi_r} = \mathbf{L_r i_r}$ in which $\mathbf{L_r}$ is computed as chapter 6

FE analytical approach: the same of the previous point but with $\mathbf{L_r}$ obtained from section 9.3.

FE simulation: reference independent FE simulations.

Results are showed in fig. 11.2, respectively in fig. 11.2a for the first sub-case and in fig. 11.2b for the second.

As it the previous test, analytical methods seems to have a good agreement with the FE simulation.

Note that a positive current, for instance in the first rotor bar, induces a counter-clockwise rotor flux linkage, which is therefore negative, following the convention.

11.3 MUTUAL CONNECTION ROTOR FLUX DUE TO STATOR CURRENTS: L_{rs}

This section wants to investigate the goodness of $\mathbf{L_{rs}}$ derived by the two methods. Preliminary, some considerations are examined.

- In the first place, $\mathbf{L_{rs}}$ is computed for different rotor positions, as a function of θ_r. This means that transient FE simulations are used in this section.
- Since such time-dependant analyses are invoked and currents are wanted as system inputs, it is not possible from a numerical and physical perspective to impose a non-zero current at time zero without setting the proper initial conditions, out of scope for this work.

  Therefore, a smooth time step is introduced. Such a function is designed to gradually transit from 0 to 1 preserving the first

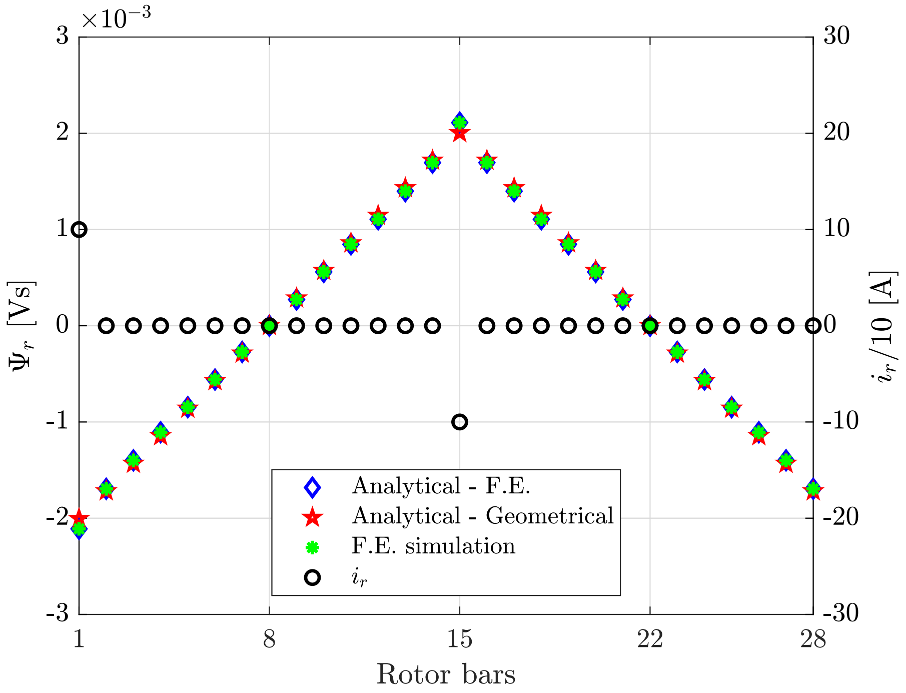

(a) First case: $i_{rb,1} = 100\,A$ and $i_{sc,15} = -100\,A$

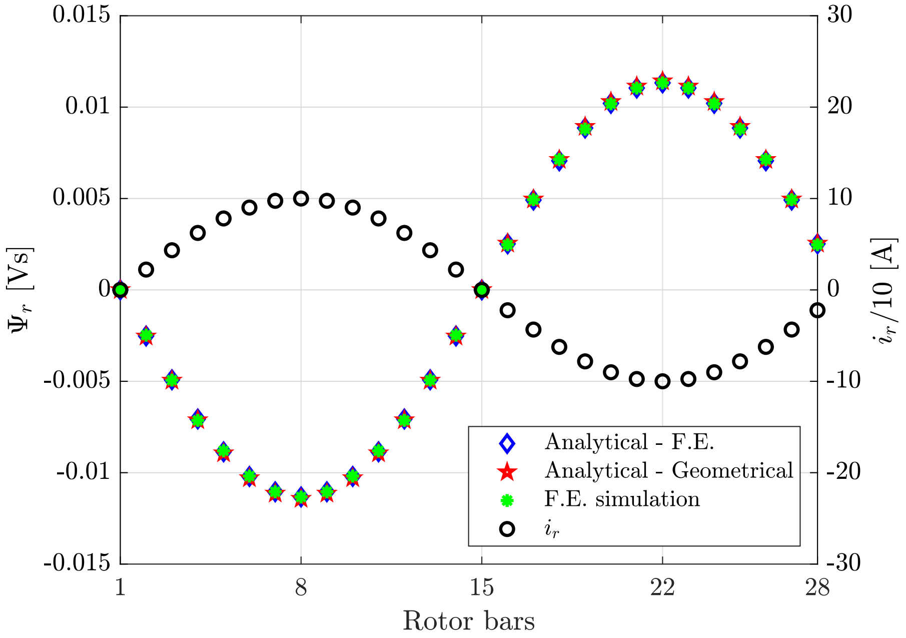

(b) Second case: sinusoidally distributed currents.

Figure 11.2: Comparison of different methods in terms of rotor bar flux linkage predictions.

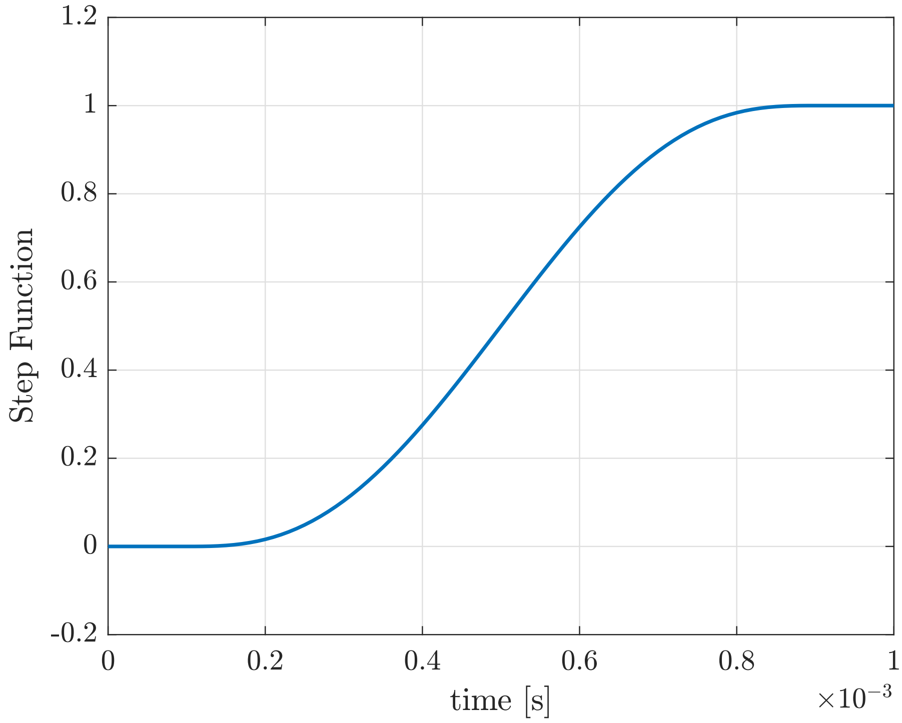

Figure 11.3: Smooth step function.

two time-derivatives. All currents are then multiplied by this function in order to reach their initial values not instantaneously. Such a function is shown in fig. 11.3 and will be referred as step(t).

- Currents are assumed to be sinusoidally changing in time, with synchronous frequency set to $f_s = 50\,\text{Hz}$. Magnitude will be defined later.
- Rotor mechanical speed is set constant in time. In principle, this value does not have primary importance. In the following simulations, the mechanical speed is set to $2400\,\text{rpm}$ so that it takes $0.025\,\text{s}$ to complete one rotation. The simulation time is then twice this value, which is the rotor mechanical period, i.e. $0.05\,\text{s}$, for the first case. For the second, a longer simulation time is chosen to depict one rotor electrical period.
- The time step chosen to present the results is $1 \times 10^{-4}\,\text{s}$, therefore 501 points are considered in the first sub-case, the double in the second.

As done previously in the other validation tests, two sub-cases are provided. Setting $I_{rms} = 3\,\text{A}$,

- in the first, coil 1 is supplied with a sinusoidal current (i.e $i_{sc,1} = 1\,\text{A}$) and the physically opposite coil, coil 19, with the

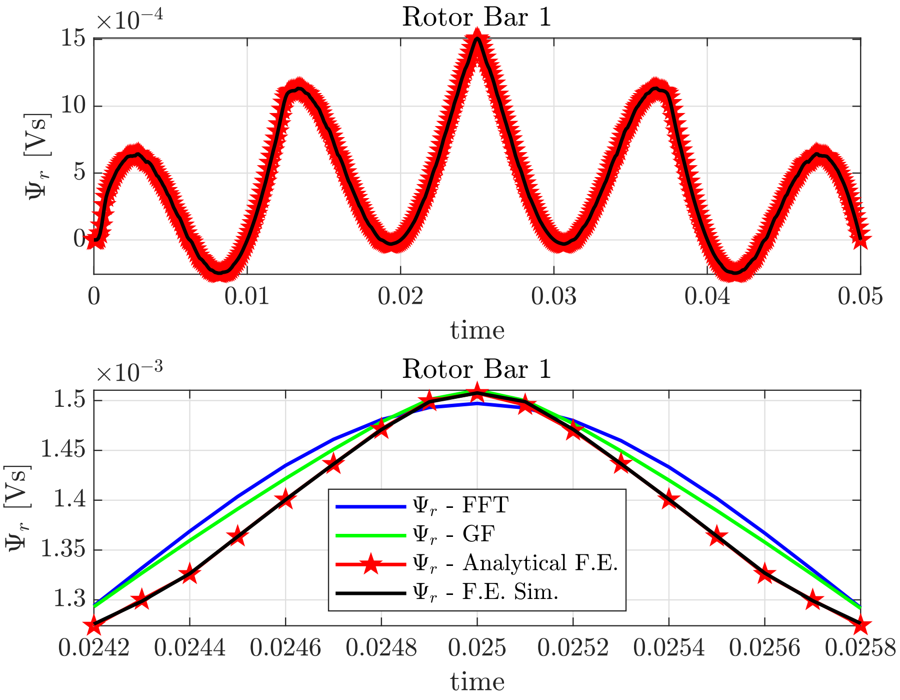

Figure 11.4: Rotor bar 1 magnetic flux linkage comparison for different methods. Below a smaller time window is set to appreciate differences.

negative current. All the other stator coils are kept to zero current as are the rotor bars.

- In the second case, a set of sinusoidally distributed currents is given as input to the system. Therefore,

$$i_{sc,j} = \text{step}(t)\sqrt{2}I_{rms}\sin\left(2\pi f_s t - \frac{2\pi}{Q_s}(j-1)\right),\ j = 1, 2, \dots, Q_s \tag{11.3}$$

The testing quantities are chosen to be:

- Rotor bar 1 flux linkage over time, $\Psi_1^r(t)$.
- Rotor bar 1 induced voltage over time, v_1^r.

The equations describing the system are the following:

$$\mathbf{\Psi_r} = \mathbf{L_{rs}i_s} + \mathbf{L_r i_r} \tag{11.4}$$

$$\mathbf{v_r} = \mathbf{R_r i_r} + \frac{d\mathbf{\Psi_r}}{dt} = \mathbf{R_r i_r} + \frac{d\mathbf{L_{rs}}}{dt}\mathbf{i_s} + \mathbf{L_{rs}}\frac{d\mathbf{i_s}}{dt} + \mathbf{L_r i_r} \tag{11.5}$$

Under the assumption - already introduced - that $\mathbf{i_r} = 0$, (11.4) and (11.5) can be simplified as:

$$\mathbf{\Psi_r} = \mathbf{L_{rs}i_s} \tag{11.6}$$

$$\mathbf{v_r} = \frac{d\mathbf{\Psi_r}}{dt} = \frac{d\mathbf{L_{rs}}}{dt}\mathbf{i_s} + \mathbf{L_{rs}}\frac{d\mathbf{i_s}}{dt} \tag{11.7}$$

Therefore the test aims at verifying the validity of methods to obtain $\mathbf{L_{rs}}$ and also that its derivative is computed correctly.

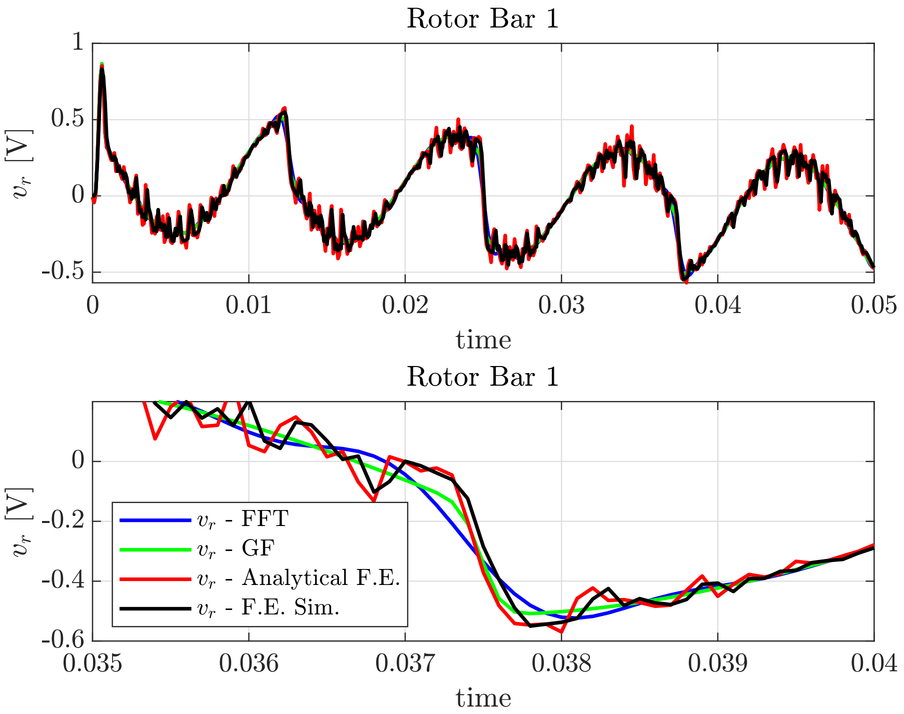

Figure 11.5: Rotor bar 1 induced voltages comparison for different methods. Below a smaller time window is set to appreciate differences.

11.3.1 *Two-coils supplying configuration*

FLUX LINKAGE Referring to the aforementioned first sub-case, (11.6) is solved and rotor bars flux linkages are obtained.

In fig. 11.4 results are given, recalling that:

FFT indicates fluxes obtained by using the Fourier's series of $\mathbf{L_{rs}}$.

GF indicates fluxes obtained by filtering the original $\mathbf{L_{rs}}$ with the Gauss filter.

ANALYTICAL FE refers to fluxes computed with the matrix extracted from FE simulations.

FE SIMULATION is the reference and it is an independent FE simulation where fluxes are directly computed and no matrix operation is carried out.

As it can be observed, fluxes obtained by matrix operations match with the reference, perfectly for what regards the Analytical FE approach. For the others, the GF is overall closer to the actual solution whereas FFT resembles better a sinusoidal shape.

VOLTAGE The last comparison is considering differences in solving voltage equation (11.7), therefore accounting also for time derivative of the matrix under analysis. Referring to the same quantities recalled

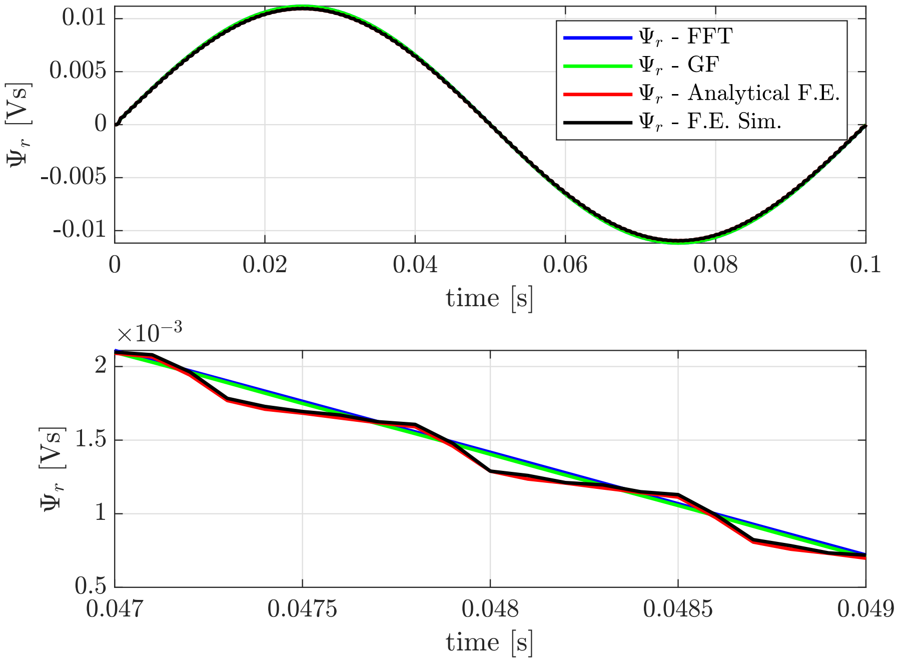

Figure 11.6: Rotor bar 1 induced magnetic fluxes comparison for different methods. Below a smaller time window is set to appreciate differences.

in the previous paragraph, fig. 11.5 shows consistency in the analytical methods based on the geometrical approach, the analytical methods with matrices extracted from FE and the reference simulation.

Therefore, it can be concluded that $\mathbf{L_{rs}}$ is capable of solving electrical equations so that the electrical behaviour of the rotor can be predicted with a satisfactory accuracy.

11.3.2 *Two-poles supplying configuration*

FLUX LINKAGE Referring to the second supplying configuration, i.e. a set of sinusoidally time varying stator currents spacially distributed to resemble a 18-phases - 2-poles configuration, fig. 11.6 shows the results in terms of rotor bar 1 flux linkage. In this configuration, the air-gap magnetic flux density is rotating at synchronous speed (50 Hz) and the rotor is imposed at 40 Hz. By recalling the slip definition [4]:

$$s = \frac{f_s - \frac{p}{2} f_m}{f_s} \tag{11.8}$$

it follows readily that $s = 0.2$. Therefore, the induced quantities on the rotor would change at the slip frequency, which is defined as:

$$f_{slip} = s f_s = 10\,\text{Hz} \tag{11.9}$$

with a rotor time period $T_{slip} = 1/f_{slip} = 0.1\,\text{s}$. A longer simulation is then needed to present at least a rotor electrical period.

Therefore, fig. 11.6 shows the output results in terms of rotor bar induced fluxes, given a supply 18-phases - 2-poles set of sinusoidal currents. In the sub-graph below, a shorter time window is set to allow a better understanding of differences, which are not relevant in practise.

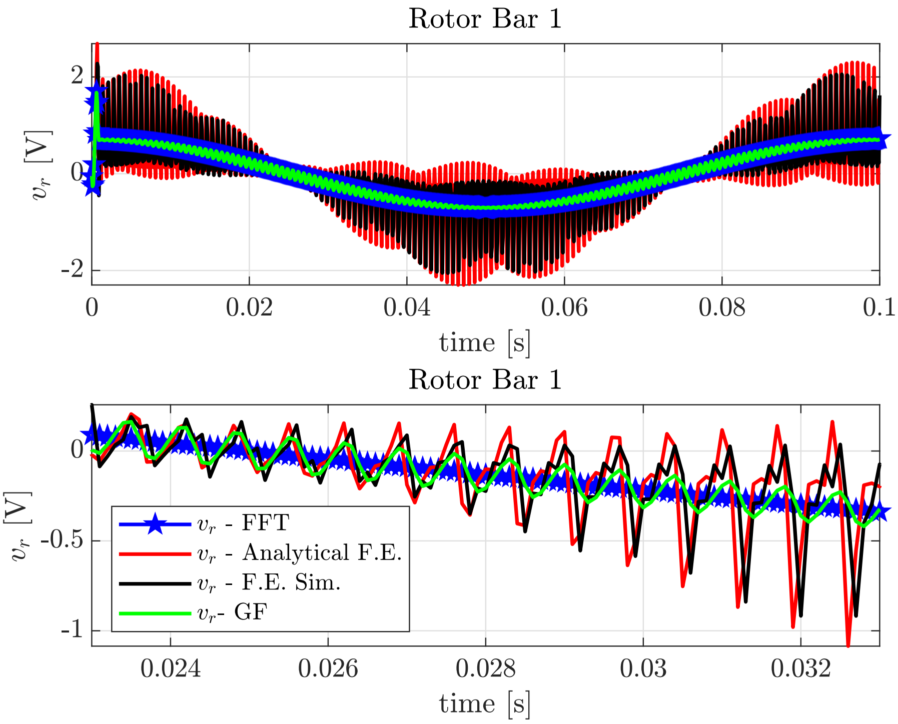

Figure 11.7: Rotor bar 1 induced voltages comparison for different methods, sinusoidally spaced currents. Below a smaller time window is set to appreciate differences.

VOLTAGE Figure 11.7 gives the last test results, rotor bar 1 voltages induced by the sinusoidal set of stator currents. The results are noisy for what regards FE. based approach and the independent FE reference, while the analytical seems to predict better an average behaviour, even if the Gauss-filtered solution has some harmonic content that resembles the real shape.

Overall, it can be concluded also with this set of currents that $\mathbf{L_{rs}}$ is valid and that (11.6) and (11.7) can be used to describe the electrical and magnetic quantities of the system under analysis, even during the initial transient.

11.4 MUTUAL CONNECTION STATOR FLUX DUE TO ROTOR CURRENTS: L_{sr}

Taking advantages of what explained in section 11.3, below two simulations will be analysed in order to verify the validity and to assess the goodness of matrix $\mathbf{L_{sr}}$.

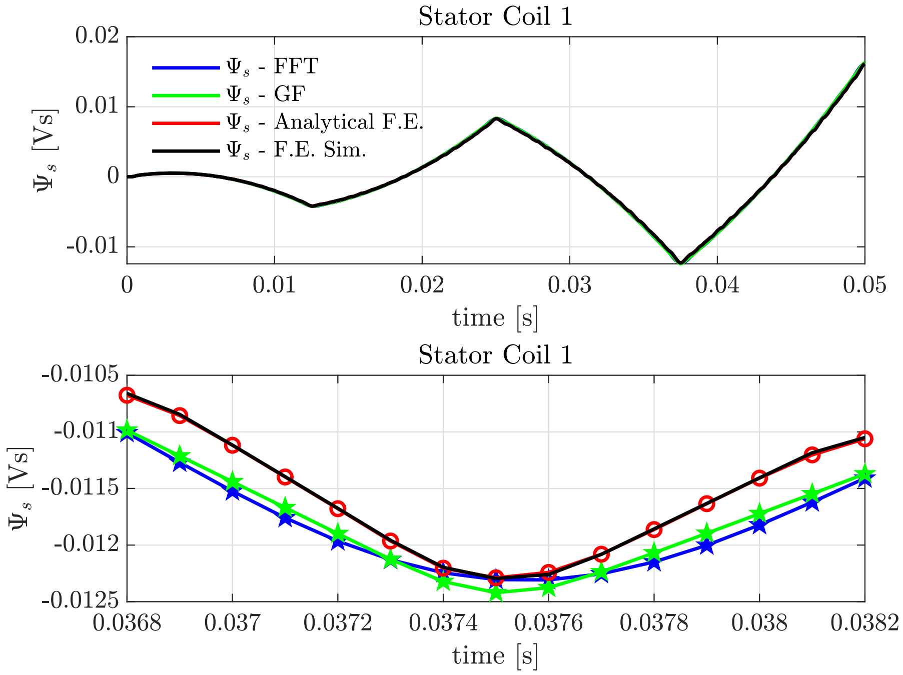

Figure 11.8: Stator coil 1 magnetic flux linkage comparison for different methods. Below a smaller time window is set to appreciate differences.

So, transient simulations will be considered, with different length in the two sub-cases; $\text{step}(t)$ is used to smooth the current from 0 to the initial value, constant rotor speed is set to $2400\,\text{rpm}$, time step is set to 1×10^{-4} s. The two sub-cases are configured as follow:

FIRST SCENARIO: rotor bar 1 is supplied with a sinusoidal current and the spacially opposite bar, rotor bar 15, with the same current but opposite in phase: given $I_{\text{peak}} = 100\,\text{A}$ and $f_r = 1.5\,\text{Hz}$,

$$i_{rb,j} = \begin{cases} \text{step}(t) I_{\text{peak}} \sin\left(2\pi f_r t - \frac{2\pi}{Q_r}(j-1)\right) & \text{for}\, j = 1, 15. \\ 0 & \text{for}\, j = 1, \dots, Q_r \end{cases} \tag{11.10}$$

SECOND SCENARIO: a set of sinusoidal currents are supplied to rotor bars, each with a phase shift to resemble a 2 poles configuration, i.e. each bar has opposite current with regards to the diametrically opposite bar. In equations:

$$i_{rb,j} = \text{step}(t) I_{\text{peak}} \sin\left(2\pi f_r t - \frac{2\pi}{Q_r}(j-1)\right) \;\text{for}\, j = 1, \dots, Q_r \tag{11.11}$$

The testing quantities are chosen to be:

- Stator coil 1 flux linkage over time, $\Psi_1^s(t)$.
- Stator coil 1 induced voltage over time, $v_1^s(t)$.

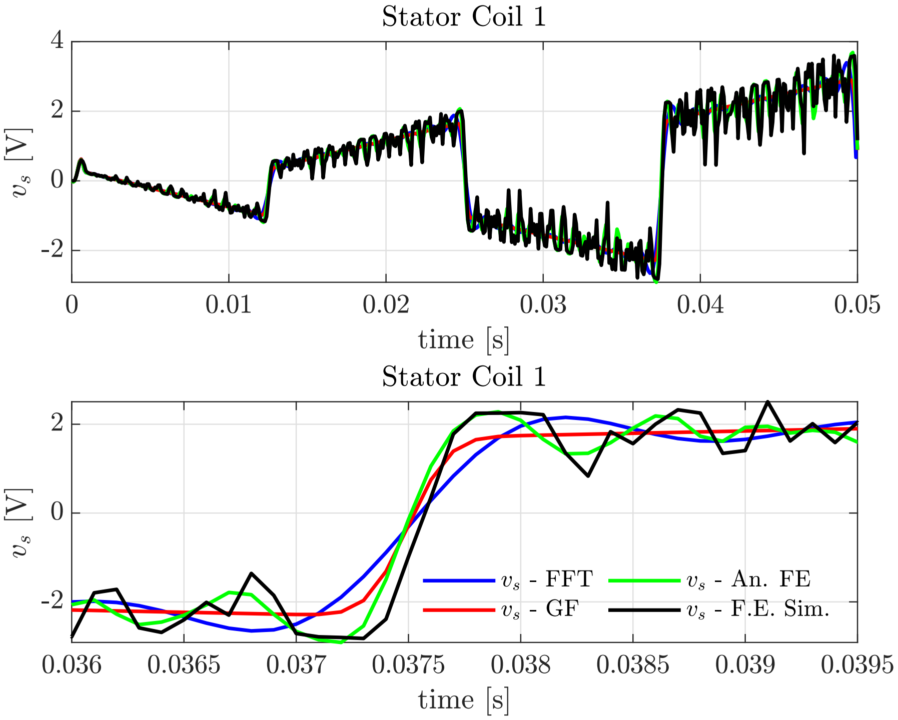

Figure 11.9: Stator coil 1 voltage comparison for different methods. Below a smaller time window is set to appreciate differences.

The equations describing the system are the following:

$$\mathbf{\Psi_s} = \mathbf{L_s i_s} + \mathbf{L_{sr} i_r} \tag{11.12}$$

$$\mathbf{v_s} = \mathbf{R_s i_s} + \frac{d\mathbf{\Psi_s}}{dt} = \mathbf{R_s i_s} + \frac{d\mathbf{L_{sr}}}{dt}\mathbf{i_r} + \mathbf{L_{sr}}\frac{d\mathbf{i_r}}{dt} + \mathbf{L_s i_s} \tag{11.13}$$

Under the assumption - already introduced - that $\mathbf{i_s} = 0$, (11.12) and (11.13) can be simplified as:

$$\mathbf{\Psi_s} = \mathbf{L_{sr} i_r} \tag{11.14}$$

$$\mathbf{v_s} = \frac{d\mathbf{\Psi_s}}{dt} = \frac{d\mathbf{L_{sr}}}{dt}\mathbf{i_r} + \mathbf{L_{sr}}\frac{d\mathbf{i_r}}{dt} \tag{11.15}$$

Therefore, $\mathbf{L_{sr}}$ and its derivative are tested on their capability to predict stator fluxes and voltages imposed rotor currents.

11.4.1 *Two-coils supplying configuration*

Referring to the aforementioned first sub-case, (11.14) is solved and stator coil flux linkages are obtained.

In fig. 11.8 results are given in terms of stator coil flux linkages, whereas in fig. 11.9 a comparison of induced coil voltage is given. No relevant difference is noticeable although it is possible to state that the smoothest results are given by Fourier's series of analytical matrix.

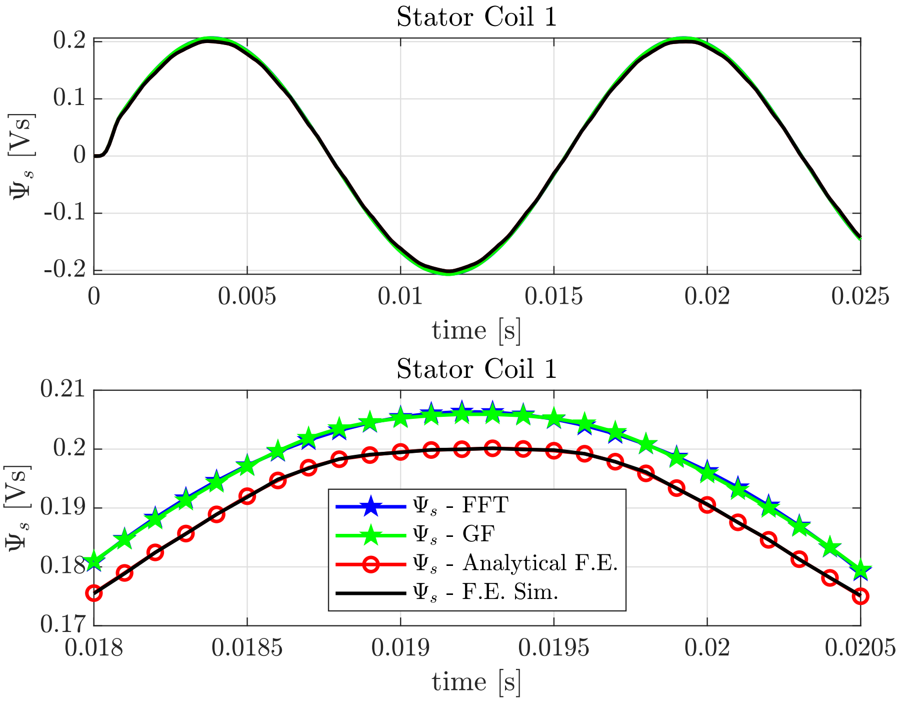

Figure 11.10: Stator coil 1 magnetic flux linkage comparison for different methods. Below a smaller time window is set to appreciate differences. Sinusoidal case.

11.4.2 *Two-poles supplying configuration*

Same considerations apply also to the second sub-case, where a 2-poles set of rotor currents are supplied. Figure 11.10 shows the output results in terms of stator coil induced fluxes. In the sub-graph below, a shorter time window is set to allow a better understanding of differences, which are not relevant in practise. In fact, as already noticed, simulations match in pairs since pure analytical methods are very similar each other, while the one derived by means of matrix extrapolation from FE match perfectly the independent numeric benchmark.

Ultimately, in fig. 11.11 voltage differences are highlighted.

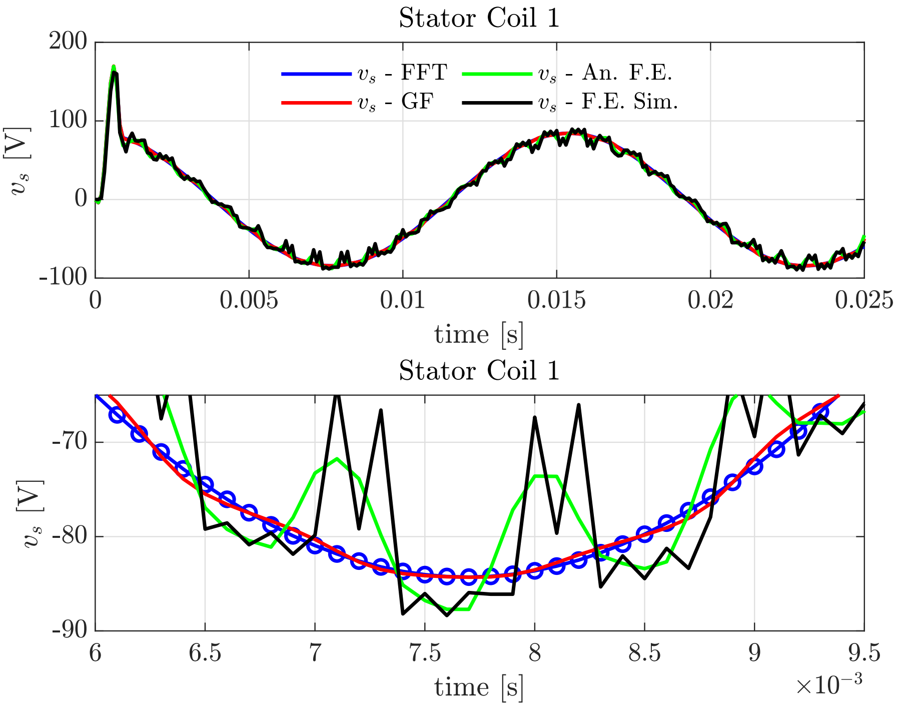

Figure 11.11: Stator coil 1 voltage comparison for different methods. Below a smaller time window is set to appreciate differences. Sinusoidal case.

12

ELECTRICAL AND MECHANICAL VALIDATION OF TRANSIENT MODELS

In this final chapter, previously described methods will be compared in their capabilities to predict stator and rotor currents given a stator voltage supply. Comparison in terms of mechanical torque are also presented and the transient during the pole change is investigated; at the end, some conclusions are drawn.

Purpose of this work is not to comment the goodness of absolute results, but it is rather to compare analytical models to an independent FE simulation. Therefore, analysis on current and torque ripple, harmonic content and other investigations to evaluate results from an absolute perceptive will not be made.

12.1 ELECTRICAL DERIVATION

The equation to solve is the following:

$$\begin{bmatrix} \mathbf{V_s} \\ 0 \end{bmatrix} = \begin{bmatrix} \mathbf{R_s} & \frac{d\mathbf{L_{mut,s-r}}}{dt} \\ \frac{d\mathbf{L_{mut,r-s}}}{dt} & \mathbf{R_r} \end{bmatrix} \begin{bmatrix} \mathbf{i_s} \\ \mathbf{i_r} \end{bmatrix} + \begin{bmatrix} \mathbf{L_s} & \mathbf{L_{mut,s-r}} \\ \mathbf{L_{mut,r-s}} & \mathbf{L_r} \end{bmatrix} \begin{bmatrix} \frac{d\mathbf{i_s}}{dt} \\ \frac{d\mathbf{i_r}}{dt} \end{bmatrix} \tag{12.1}$$

where $\mathbf{V_s}$ is the stator voltage excitation of the system, and $\mathbf{i_s}$ and $\mathbf{i_r}$ the wanted electrical quantities. In following comparisons, stator current in coil 1 ($i_{s,1}$) and rotor current in bar 1 ($i_{r,1}$) as a function of time are taken as a reference.

12.2 MECHANICAL TORQUE

FINITE ELEMENT EXPRESSION In FE environment, Arkkio's expression to compute mechanical torque is adopted [21]. By means of Maxwell's stress tensor, torque is expressed as [16]:

$$T_m = \frac{L_a}{\mu_0} \int_0^{2\pi} r^2 B_\phi B_r d\phi \tag{12.2}$$

in which, if the solution were exact, the torque would not depend on the radius r which varies between r_r and $r_{s,in}$ so, considering $r_\delta = (r_r + r_{s,in})/2$, the following known expression arises:

$$T_m = \frac{L_a r_\delta}{\mu_0} \int_0^{2\pi} B_\phi B_r d\phi \tag{12.3}$$

In an approximate numeric solution, Arkkio found out that the integration path has an effect on the result as high as 50 % from the average value. Therefore, torque should be computed as the average of different torque values computed by integrating at different radius:

$$T_m = \frac{1}{r_{s,in} - r_r} \int_{r_r}^{r_{s,in}} T_m \, dr \tag{12.4}$$

Eventually, (12.5) is obtained. By using this formulation, the result has been proved more reliable than the expression in (12.2)

$$\begin{aligned} T_m &= \frac{L_a}{\mu_0} \int_{r_r}^{r_{s,in}} \int_0^{2\pi} r^2 B_\phi B_r \, d\phi \qquad &(12.5)\\ &\simeq \frac{L_a}{\mu_0 \left(r_{s,in} - r_r\right)} \iint_{S_{avg}} r B_\phi B_r \, d\phi \qquad &(12.6)\\ & &(12.7) \end{aligned}$$

where S_{avg} is the air-gap cross-sectional area.

ANALYTICAL EXPRESSION In the two analytical approaches, torque is computed by means of co-energy approach.

First, an expression of co-energy is found:

$$\begin{aligned} W_{co} &= \int \boldsymbol{\Psi_s}^T d\mathbf{i_s} + \int \boldsymbol{\Psi_r}^T d\mathbf{i_r} \qquad &(12.8)\\ &= \int \left(\mathbf{L_s i_s}\right)^T d\mathbf{i_s} + \int \left(\mathbf{L_{sr} i_r}\right)^T d\mathbf{i_s} + \int \left(\mathbf{L_{rs} i_s}\right)^T d\mathbf{i_r} + \int \left(\mathbf{L_r i_r}\right)^T d\mathbf{i_r} \qquad &(12.9)\\ &= \frac{1}{2}\mathbf{i_s}^T \mathbf{L_s}^T \mathbf{i_s} + \frac{1}{2}\mathbf{i_r}^T \mathbf{L_{sr}}^T \mathbf{i_s} + \frac{1}{2}\mathbf{i_s}^T \mathbf{L_{rs}}^T \mathbf{i_r} + \frac{1}{2}\mathbf{i_r}^T \mathbf{L_r}^T \mathbf{i_r} \qquad &(12.10) \end{aligned}$$

Second, mechanical torque is obtained as derivative of co-energy with respect to rotor angular position; since only mutual matrices depend on rotor position, the following relation can be written:

$$\begin{aligned} T_m &= \frac{\partial W_{co}}{\partial \theta_m} \qquad &(12.11)\\ &= \frac{1}{2}\left(\mathbf{i_r}^T \frac{\partial \mathbf{L_{sr}}^T}{\partial \theta_r} \mathbf{i_s} + \mathbf{i_s}^T \frac{\partial \mathbf{L_{rs}}^T}{\partial \theta_r} \mathbf{i_r}\right) \qquad &(12.12) \end{aligned}$$

12.3 SIMULATIONS

In this section, a comparison of analytical transient models and FE independent simulations is shown. The supplying stator coil voltage can be written as:

$$v_{s,k} = V_s \cos(2\pi f_s t - \phi_k) \tag{12.13}$$

where ϕ_k depends on the coil and supplying configuration adopted. Peak voltage value has been set to 25 V, i.e. $V_s = 25\,\text{V}$, whereas synchronous frequency to industrial frequency, i.e. $f_s = 50\,\text{Hz}$.

Regarding the voltage supplying configuration, only solutions with 1 slot per pole per phase are presented (i.e. 18 phases - 2 poles, 9 phases - 4 poles, 3 phases - 12 poles). In fact, when the number of slot per pole per phase is higher than one, in such slots ideally the same current flows. Nevertheless, a specific coil voltage is needed to achieve equal (or opposite) current in different slots, because the stator flux linkage varies depending on the spacial position considered.

12.3.1 *Linear materials*

Simulations here reported consider ideal linear iron with $\mu_r = 1 \times 10^4$.

12.3.1.1 *Two-poles configuration*

$s = 100\,\%$ In this scenario, the rotor is assumed to be standstill. In principle, mutual matrices are constant over time because θ_r does not change and their derivatives are zero. As a result, starting torque cannot be computed adopting the co-energy approach.

Nevertheless, considering for instance fig. 9.7 and fig. 10.1, the point value of matrix derivatives at $\theta_r = 0$ is known and it is not always zero.

Therefore, instead of deriving a constant matrix and obtaining zero values, the choice adopted is that of evaluating the matrix derivative function at $\theta_r = 0$; this value is then constant because it is derived by evaluating a function always in the same point.

The ultimate result is to decouple matrix parameters and their derivatives, since both of them are constant. This approach allows to match FE simulations.

Figure 12.1 shows the comparison in terms of stator and rotor currents (respectively for stator coil 1 and rotor bar 1) and mechanical torque.

$s = 0\,\%$ Figure 12.2 shows the comparison in terms of stator and rotor currents (respectively for stator coil 1 and rotor bar 1) and mechanical torque. First part of the transient is shown in left graphs, while steady-state behaviour is given in plots on the right. It is possible to notice an overall good agreement between analytical models and FE simulation, since first ones seem to preserve the average value of both currents and torque.

$s = 25\,\%$ This comparison is shown in fig. 12.3. The most evident element in this simulation is that the analytical method shown in blue presents a slight phase delay, i.e. it is lagging behind the numerical-analytical and FE reference. In terms of torque, analytical methods tend to overestimate the result especially during the transient; such difference is reduced at steady-state.

$s = 2.5\,\%$ In fig. 12.4 electrical and torque comparison is provided.

Considering fig. 12.4a, first part of the transient is shown in left graphs, while steady-state behaviour is given in plots on the right. It is possible to notice an overall good agreement between analytical models and FE simulation, since analytical models seem to preserve the low frequency pattern. Considering the mechanical plot in fig. 12.4b, there is a disagreement both in transient and steady-state values, where the FE results are higher than analytical predictions.

12.3.1.2 *Four-poles configuration*

Figure 12.5 shows the comparison regarding a 9-phases 4-poles voltage supplying configuration.

12.3.1.3 *Twelve-poles configuration*

Figure 12.6 presents the comparison regarding a 3-phases 12-poles voltage supplying configuration.

12.3.2 *Pole transition*

Following simulations consider a pole transition, which occurs at $t = 0.4\mathrm{s}$. The supplying voltage frequency changes after the transition so that, keeping the mechanical speed constant, the slip value does not change. Therefore, in following plots supply frequency f_s refers to the two-poles case.

TWO-TO-FOUR POLES This scenario is depicted in fig. 12.7.

TWO-TO-TWELVE POLES This simulation is shown in fig. 12.8

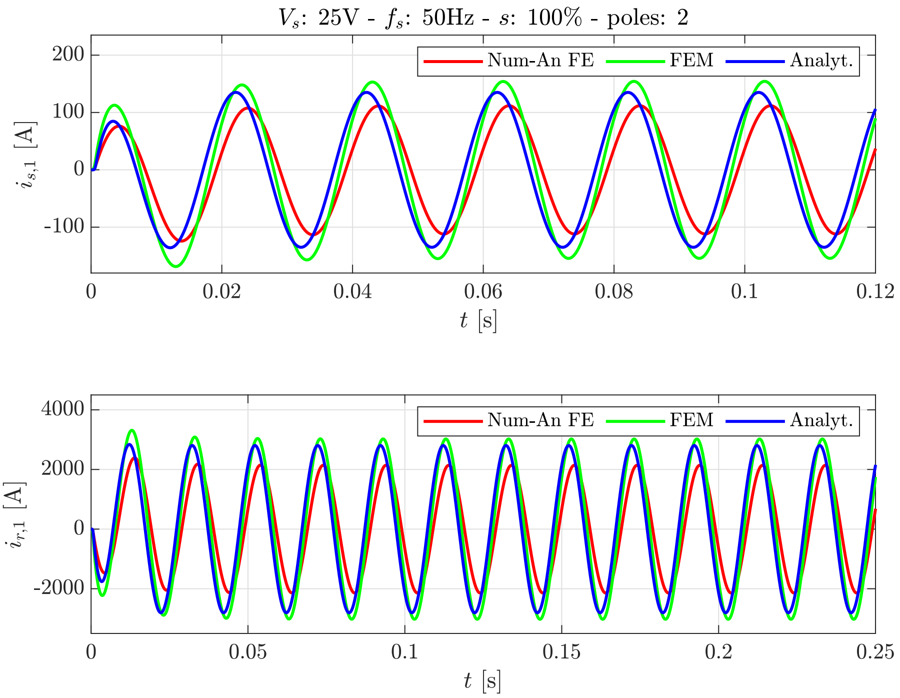

(a) Model comparison in terms of stator and rotor currents.

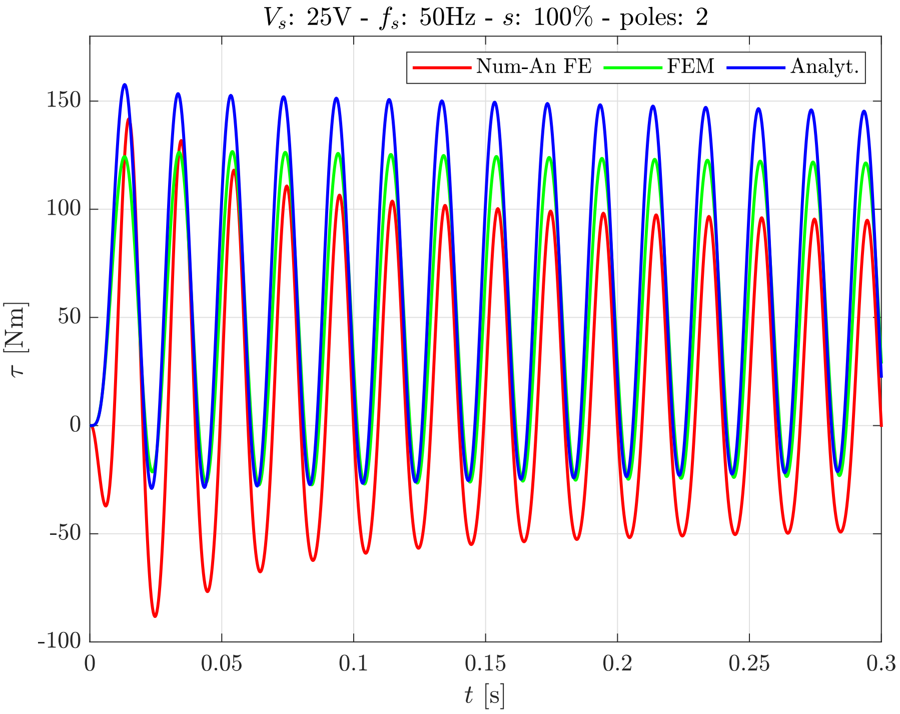

(b) Model comparison in terms of mechanical torque.

Figure 12.1: Electrical and mechanical comparison of models, linear materials, 2-poles, $s = 100\,\%$.

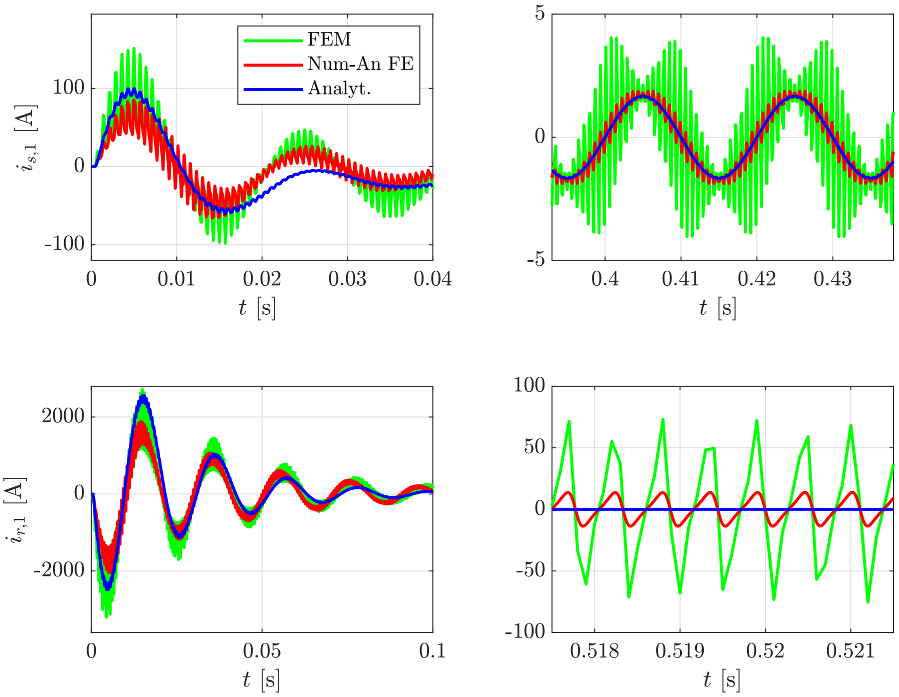

(a) Model comparison in terms of stator and rotor currents, transient and steady-state.

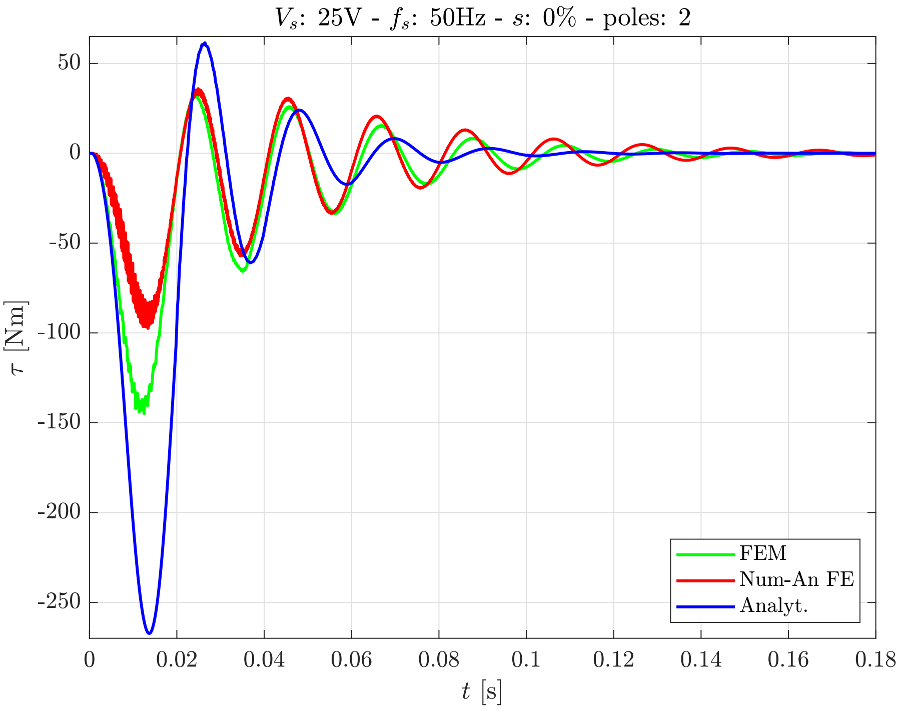

(b) Model comparison in terms of mechanical torque.

Figure 12.2: Electrical and mechanical comparison of models, linear materials, 2-poles, $s = 0\,\%$.

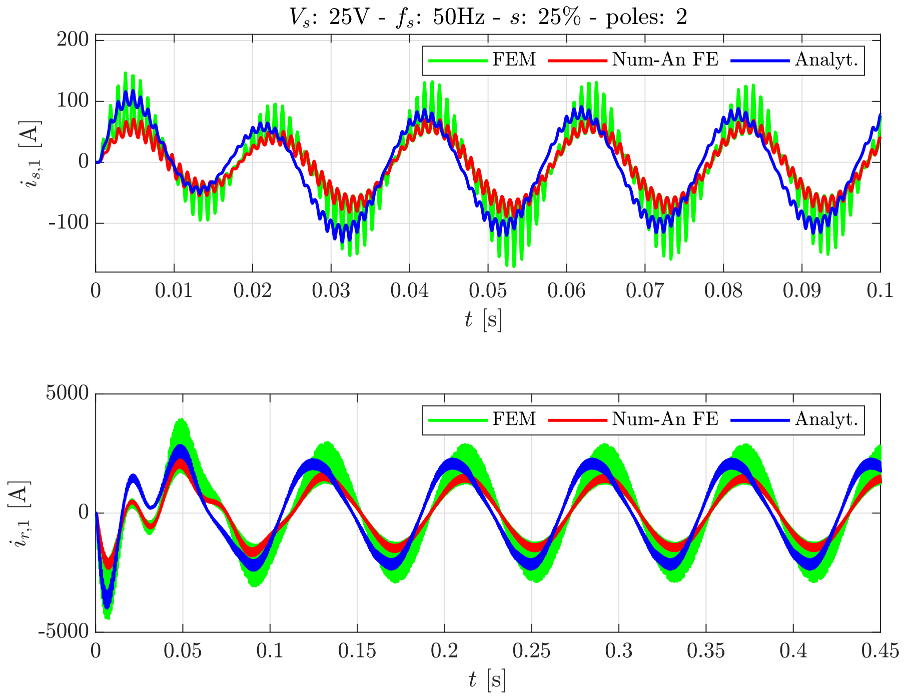

(a) Model comparison in terms of stator and rotor currents.

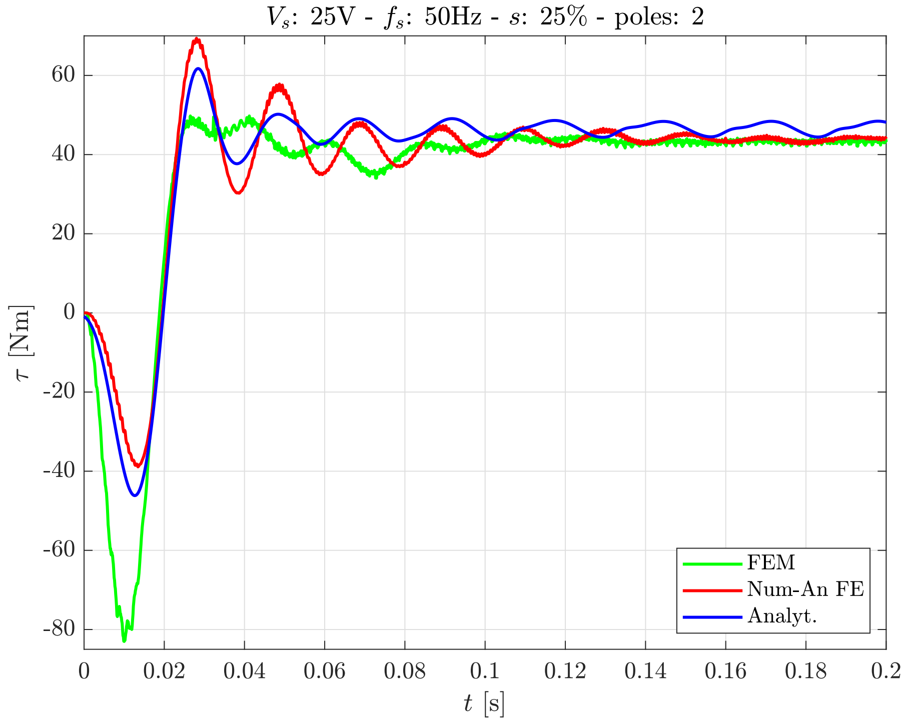

(b) Model comparison in terms of mechanical torque.

Figure 12.3: Electrical and mechanical comparison of models, linear materials, 2-poles, $s = 25\,\%$.

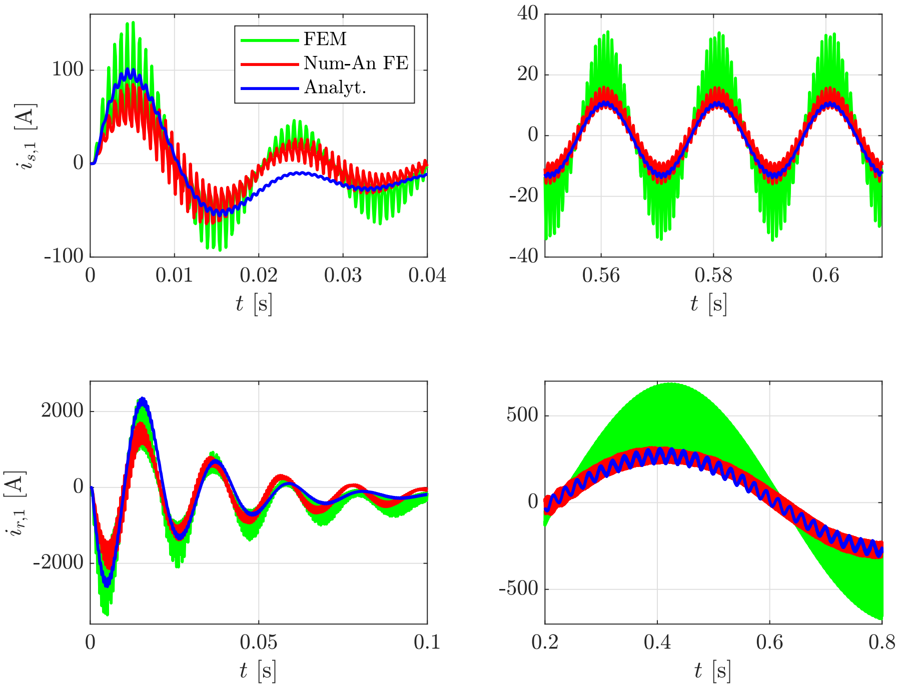

(a) Model comparison in terms of stator and rotor currents.

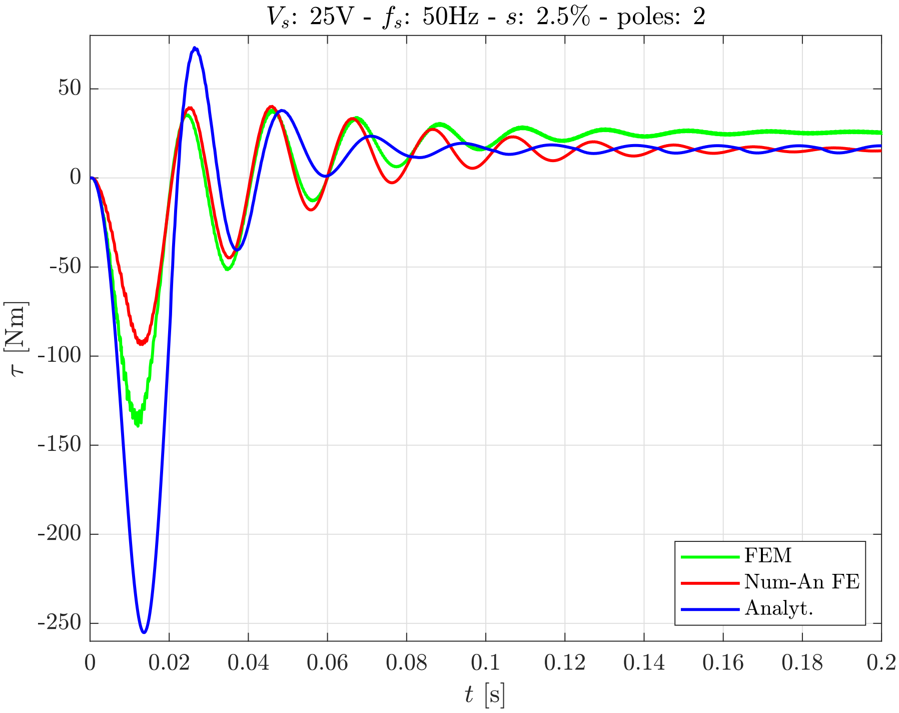

(b) Model comparison in terms of mechanical torque.

Figure 12.4: Electrical and mechanical comparison of models, linear materials, 2-poles, $s = 2.5\,\%$.

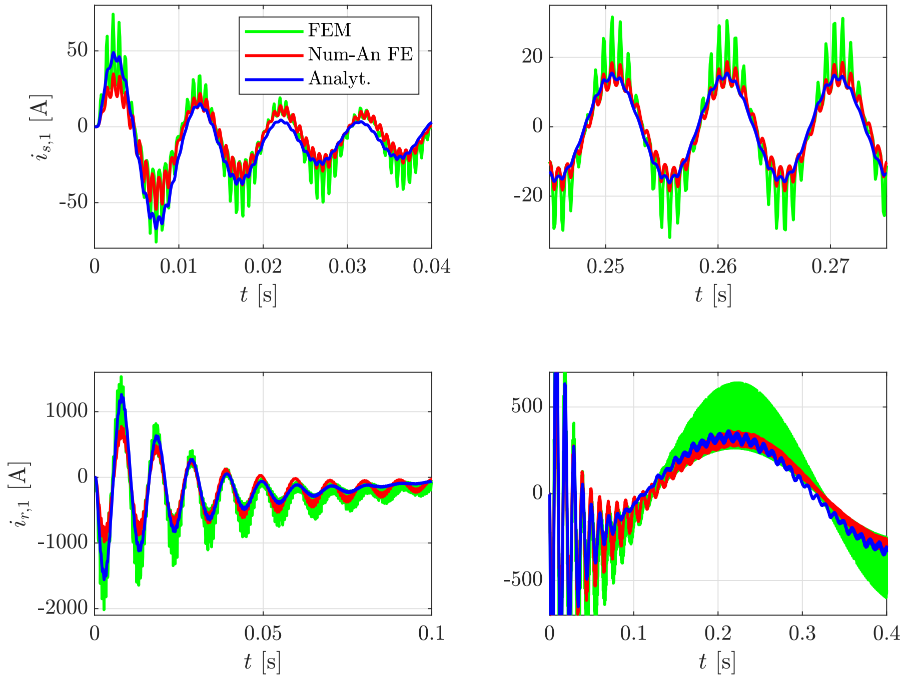

(a) Model comparison in terms of stator and rotor currents.

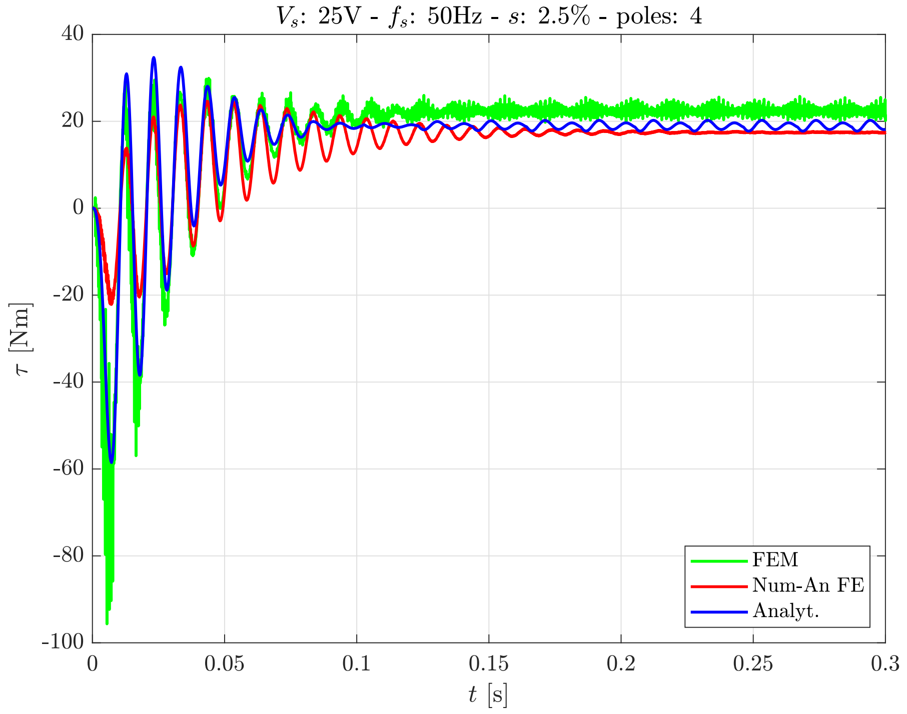

(b) Model comparison in terms of mechanical torque.

Figure 12.5: Electrical and mechanical comparison of models, linear materials, 4-poles, $s = 2.5\,\%$.

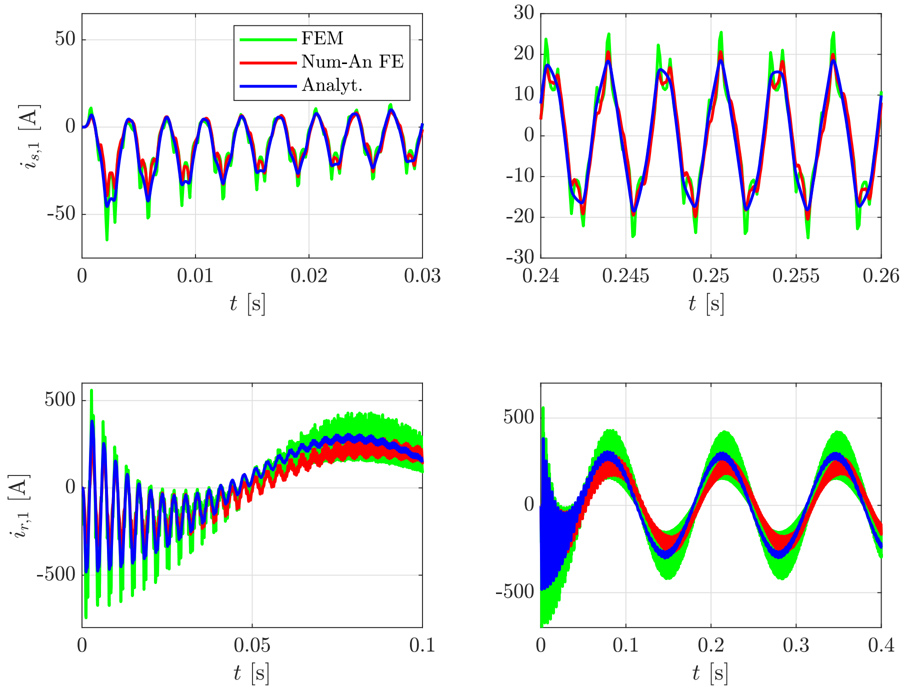

(a) Model comparison in terms of stator and rotor currents.

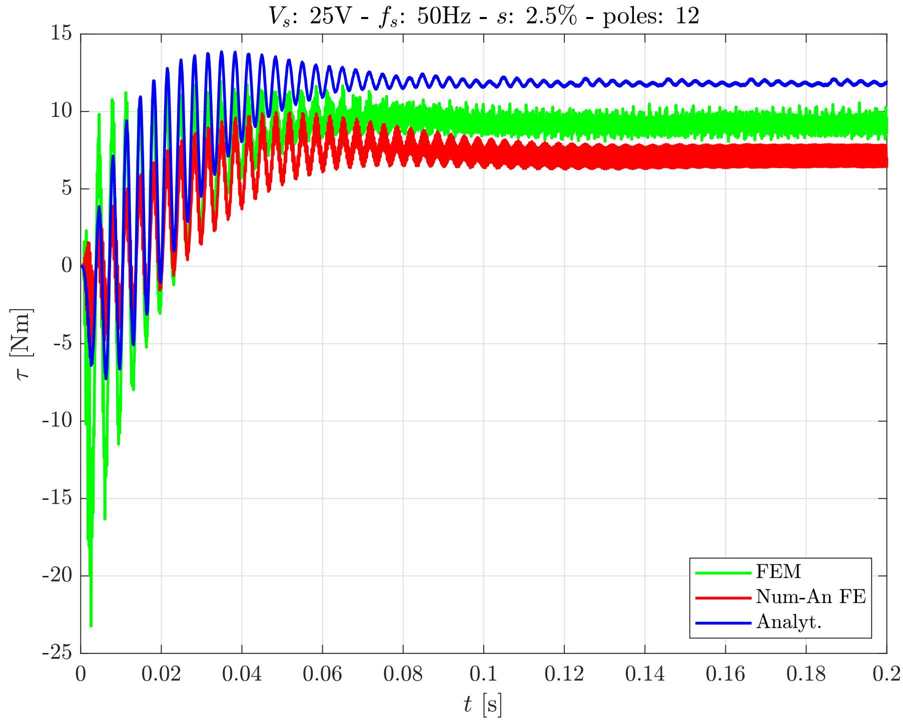

(b) Model comparison in terms of mechanical torque.

Figure 12.6: Electrical and mechanical comparison of models, linear materials, 12-poles, $s = 2.5\,\%$.

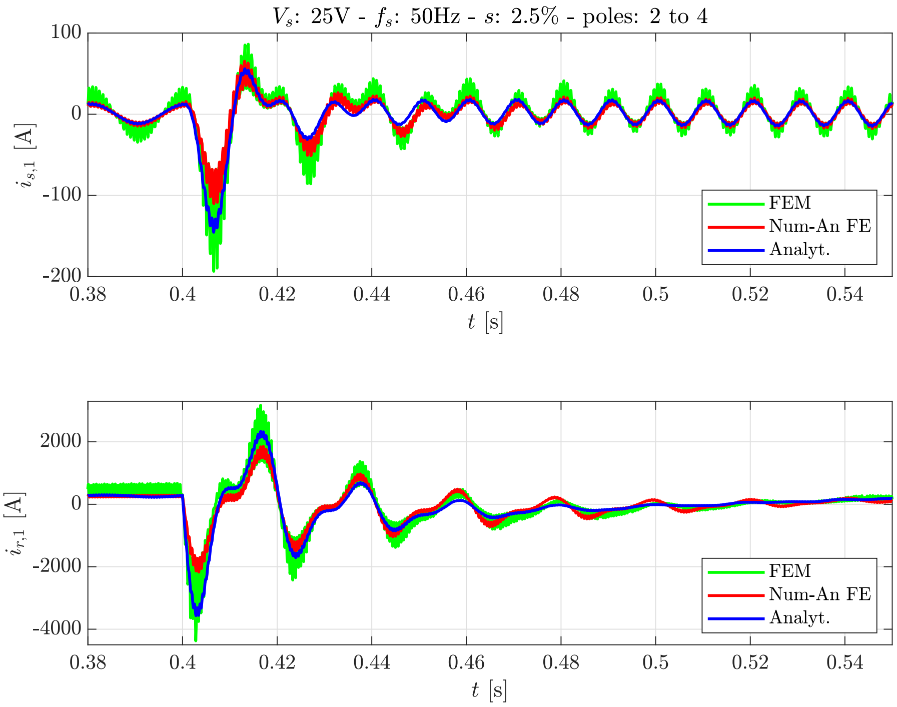

(a) Model comparison in terms of stator and rotor currents.

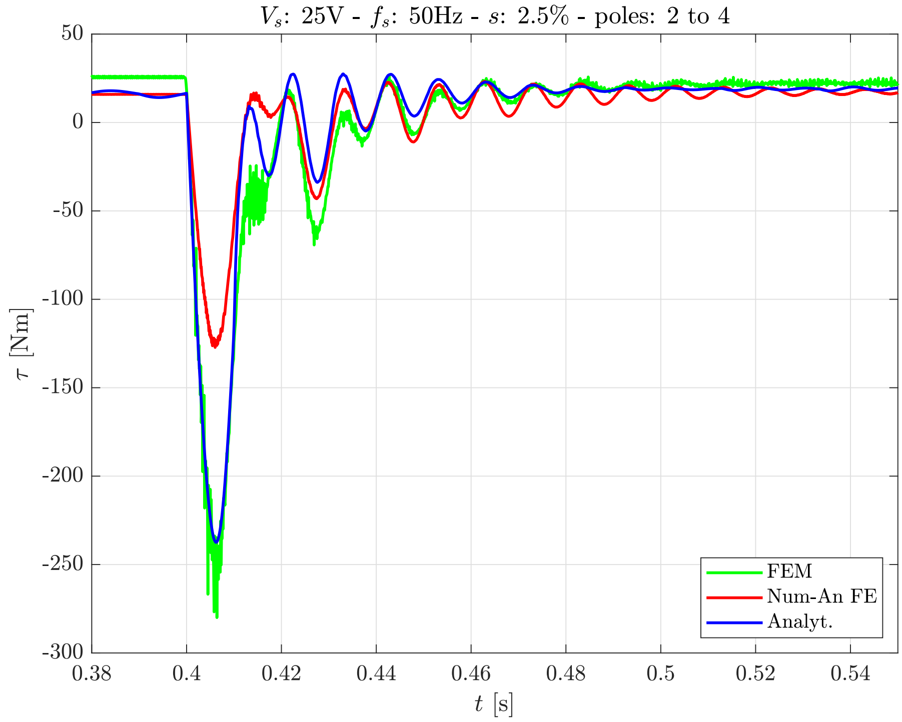

(b) Model comparison in terms of mechanical torque.

Figure 12.7: Electrical and mechanical comparison of models, linear materials, pole transition, $s = 2.5\,\%$.

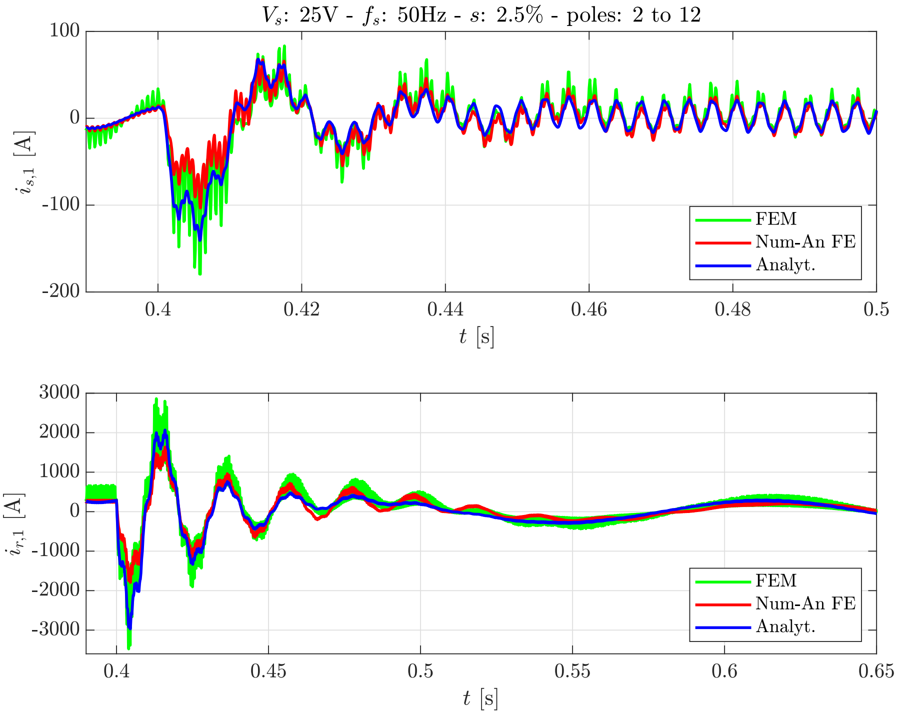

(a) Model comparison in terms of stator and rotor currents.

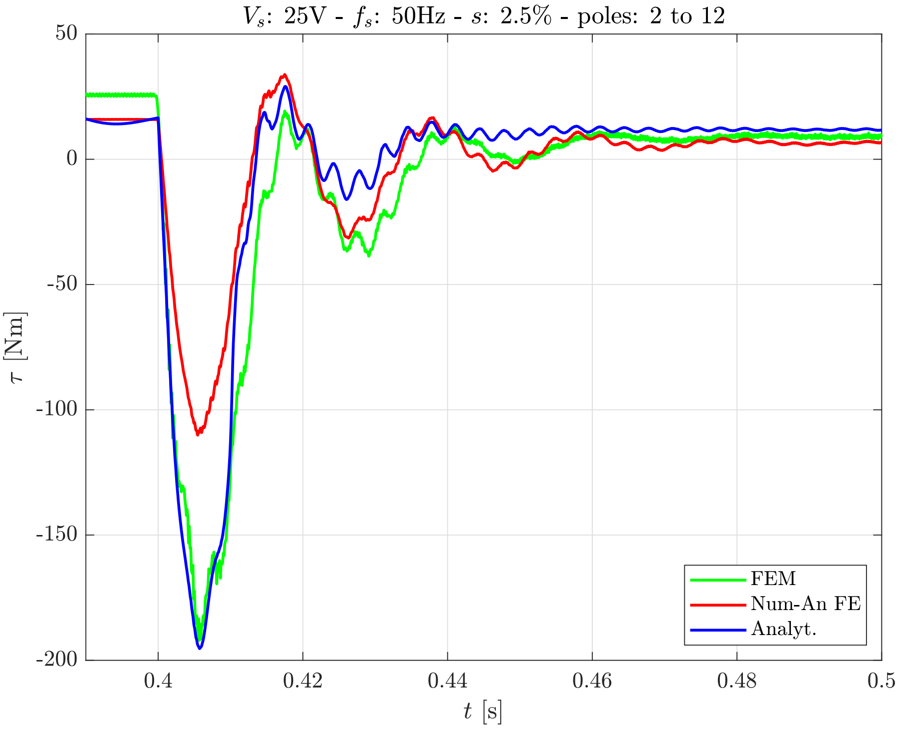

(b) Model comparison in terms of mechanical torque.

Figure 12.8: Electrical and mechanical comparison of models, linear materials, pole transition $s = 2.5\,\%$.

12.3.3 *Non-linear materials*

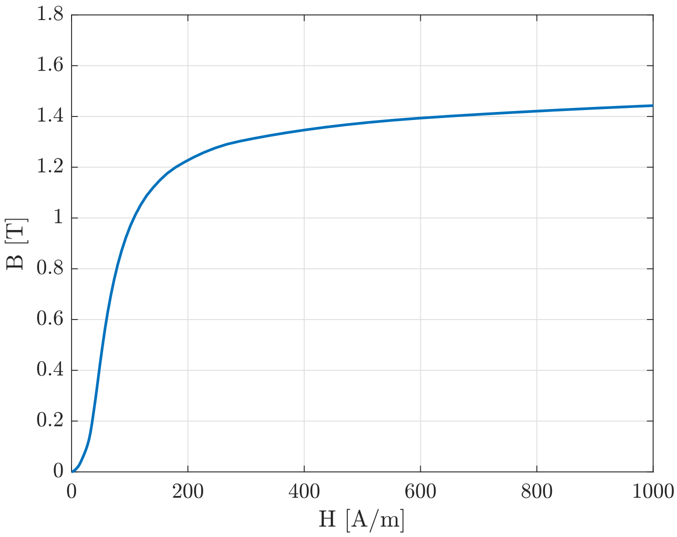

Figure 12.9: $B - H$ curve of lamination material used for non-linear simulations.

Recalling section 9.1.1.2, when considering linear iron in a deep-bar squirrel-cage rotor, it is needed to introduce a fictitious bar opening to avoid high saturation on the iron top part of each bar which prevents the flux from linking the stator. This geometry modification brought to the FE model is an approximation because in reality it is not present, and saturation occurs. In this section, simulations with non linear materials are considered and compared to linear ones. The $B - H$ curve of real iron is depicted in fig. 12.9.

12.3.3.1 *Two-poles configuration*

$s = 25\,\%$ Figure 12.10 compares analytical simulations with non-linear materials FE reference. It can be noticed that torque reference by FE is more noisy than the simulation with linear materials (see fig. 12.3). Moreover, torque spikes during transient are mitigated by considering linear materials. For what regard electrical quantities, no appreciable difference occurs. Following this consideration, the approximation adopted with the fictitious rotor bar opening can be considered valid.

12.3.3.2 *Pole transition*

Figure 12.11 provides the same simulation of the one shown in fig. 12.7 but with non-linear iron. As already noticed, transient peak values are lower in terms of electrical current and analytical models overall provide a good approximation of FE results.

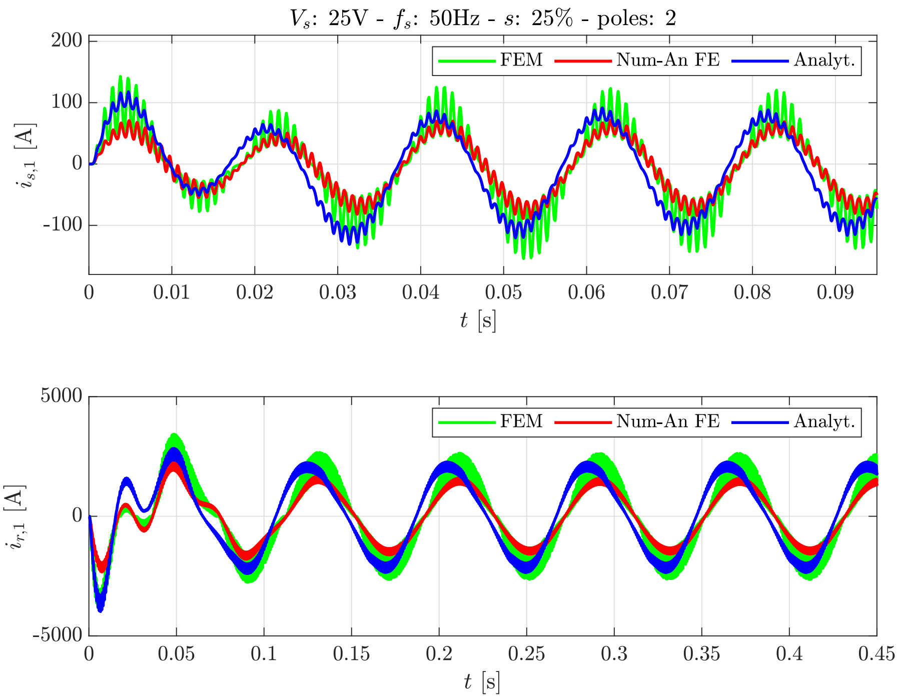

(a) Model comparison in terms of stator and rotor currents.

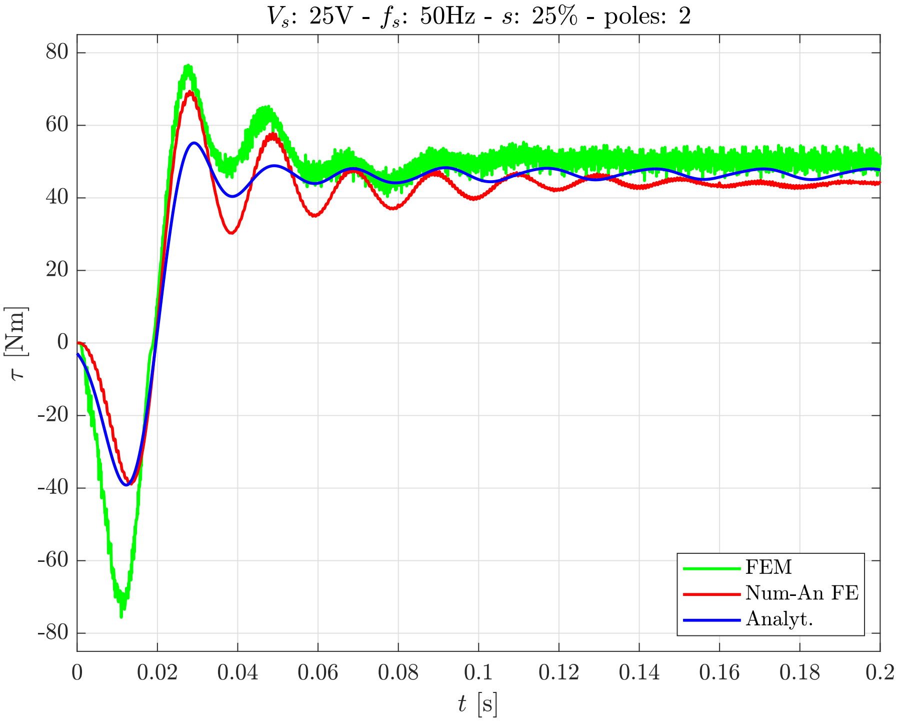

(b) Model comparison in terms of mechanical torque.

Figure 12.10: Electrical and mechanical comparison of models, non-linear materials, $s = 25\,\%$.

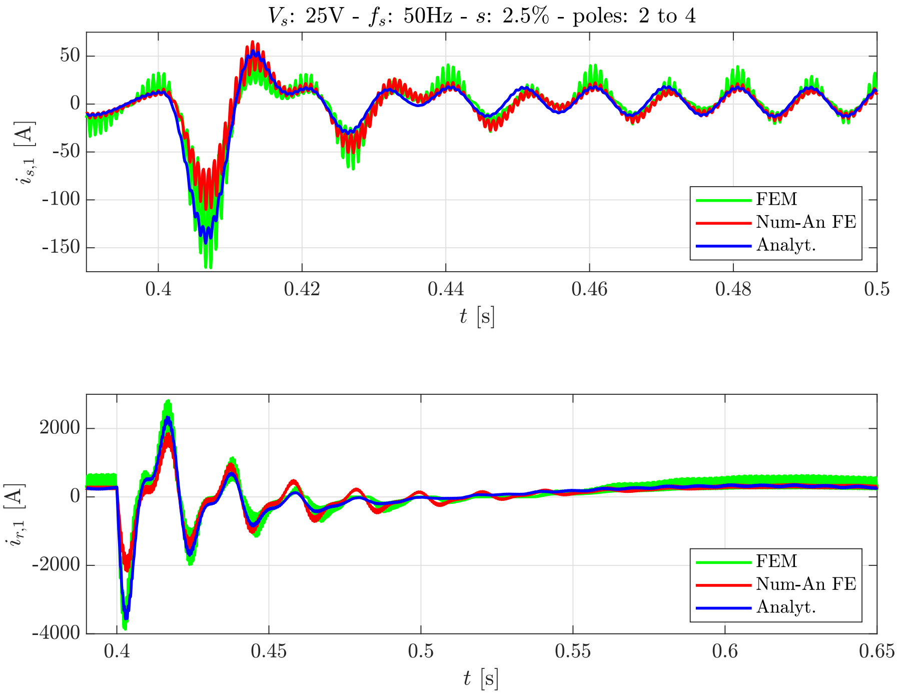

(a) Model comparison in terms of stator and rotor currents.

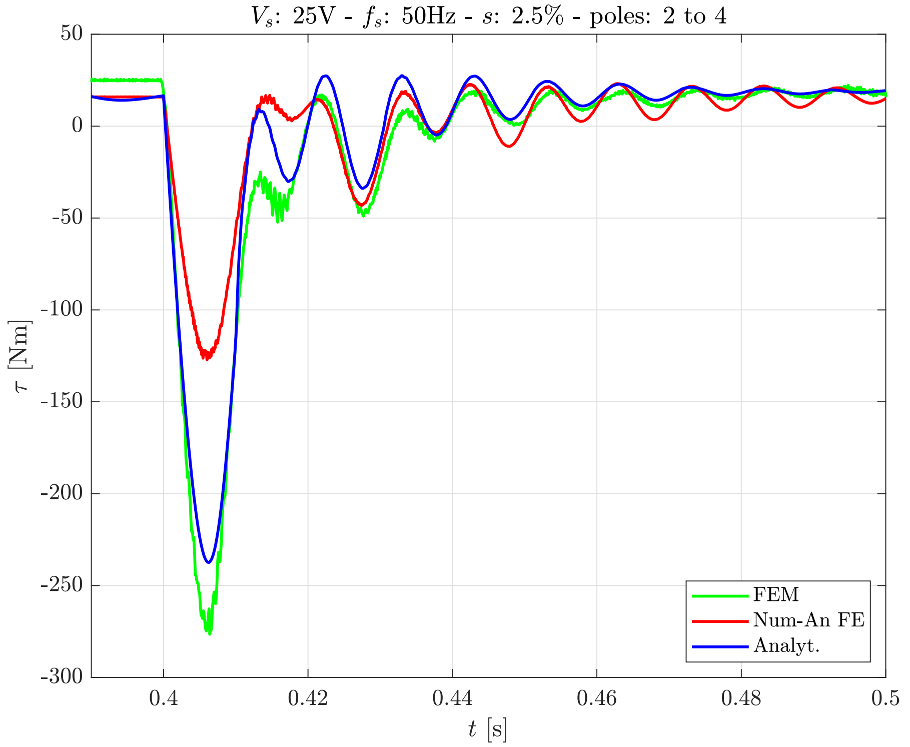

(b) Model comparison in terms of mechanical torque.

Figure 12.11: Electrical and mechanical comparison of models, non-linear materials, $s = 2.5\,\%$.

12.4 CONCLUSIONS

In this work, two models have been derived to study the electrical and mechanical transient behaviour of the WICSC motor. These models have been compared to FE simulations both adopting linear and non-linear materials. It is possible to state that the models are capable of predict qualitatively the time-pattern and could be useful to design a controller for the machine. In particular, the analytical method presents a phase delay in electrical currents that could be addressed in the first place by introducing leakage inductance matrices, since such a model does not consider any non-idealities. Therefore, a future improvement could be to evaluate leakages and incorporate them within the model. The numerical-analytical model derived from FE is accurate in terms of electromagnetic quantity prediction, but it heavily relies on the superposition of effects and value scaling. This is a limit that could be solved by mapping inductance parameters for different values of currents and therefore at different saturation levels.

For what regards torque validation, both methods do not give a precise value although their pattern over time is similar to FE references.

Ultimately, these models as well as the FE simulations need to be validated through practical studies on the real motor.

APPENDIX

A

NUMERICAL DERIVATIVE

Here it is explained how numerical derivatives with second-order truncation error is performed. This will be explained for time-dependent functions but it can be readily generalized for any x-dependent function simply by substituting variable t with the wanted one.

First, the expression of forward difference approximation for the first time derivative is given:

$$f'(t_k) = \frac{df(t)}{dt}\Big|_{t=t_k} = \frac{f(t_{k+1}) - f(t_k)}{t_{k+1} - t_k} \tag{A.1}$$

Second, the Taylor-Maclaurin 2nd-order series expansion of a generic time-dependant function $f(t)$ is expressed, where $\Delta t = t_{k+1} - t_k$.

$$f(t_{k+1}) = f(t_k) + \Delta t f'(t_k) + \frac{\Delta t^2}{2} f''(t_k) \tag{A.2}$$

from which it follows that:

$$f'(t_k) = \frac{f(t_{k+1}) - f(t_k)}{\Delta t} - \frac{\Delta t}{2} f''(t_k) \tag{A.3}$$

Applying (A.1) at the second time derivative, the following expression results:

$$f''(t_k) = \frac{f(t_{k+2}) - 2f(t_{k+1}) + f(t_k)}{\Delta t^2} \tag{A.4}$$

By substituting (A.4) in (A.3), the final expression in (A.5) for the first time derivative with truncation error on the order of Δt^2 is found. Such expression is the three-points forward difference approximation of the first time derivative.

$$f''(t_k) = \frac{-f(t_{k+2}) + 4f(t_{k+1}) - 3f(t_k)}{2\Delta t} \tag{A.5}$$

B

AIR-GAP TO YOKE FLUX RELATION

B.1 EQUIVALENT ELECTRICAL CIRCUIT METHOD

The main goal of this appendix is to derive the magnetic flux in the stator yoke driven by a certain magnetic flux density distribution in the air-gap.

Consider the circuit depicted in fig. B.1. It represents the equivalent electrical circuit of the magnetic simplified circuit of the multiphase induction motor (where R stands for the magnetic reluctance) that we need to solve.

Its inputs are the air-gap fluxes $\Phi_{\delta,j}$ with $j = 1, 2, 3, 4.$ - previously obtained by the input currents - and which are represented by current generators in the equivalent electrical circuit.

The outputs we aim at are the stator yoke fluxes Φ_k with $k = 1, 2, 3, 4.$

Note that, for seek of simplicity:

- R_1 represents the equivalent leakage reluctance which corresponds to the parallel path the air-gap flux could follow instead to flow in the stator core. We will call this *leakage reluctance*.
- R_2 represents the reluctance of the portion of stator core between two stator coils. This will be called *core reluctance*.

In order to solve the circuit, here are the logical steps to follow:

1. We add the air-gap reluctance merely to be able to solve the circuit. In fact, without R_1, this circuit cannot be solved as it is since some electrical quantities are undefined (e.g. the voltage between node 1 and 5) and furthermore the superposition of effects cannot be applied.
2. We write the netlist of the circuit to use the nodal analysis (tableau analysis) in order to determine the solutions. The general equation to solve is: $\mathbf{Tx} = \mathbf{s}$ where $\mathbf{T}$ is the tableau matrix, $\mathbf{x}$ is the array of unknowns (current in each edge, voltage across each edge, electric potential in each node apart the grounded one, that is chosen to be node 5). Finally, $\mathbf{s}$ is the vector of sources, that are the 4 current generators.
3. Once the general solution $\mathbf{s}$ is found, we may compute the $\mathbf{s}_\infty = \lim_{(R_1,R_2)\to(\infty,0)} \mathbf{s}$ i.e. the limit of the solution for the leakage reluctance going to infinite and the core reluctance going to zero. In the same manner, $\mathbf{T}_\infty$ could be inferred. This is a subcase, and could be neglected if the reluctances are computed.

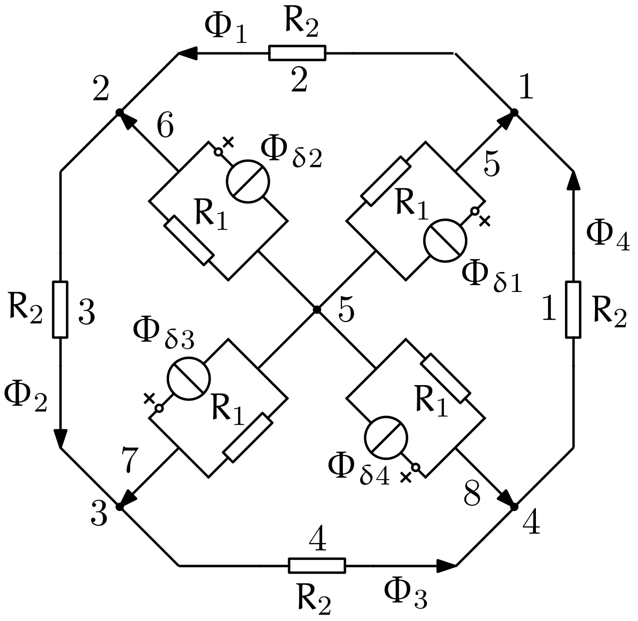

Figure B.1: Equivalent circuit for $Q_s = 4$.

4. Proceeding with the at-the-limit approach, we try to find the sub-matrix of $\mathbf{M} \triangleq \mathbf{T}_{\infty}^{-1}$ that gives the relation between inputs and outputs: $\boldsymbol{\Phi} = \mathbf{T}_{\infty}^{-1}\boldsymbol{\Phi}_{\delta}$.

B.2 NETLIST

Again, for seek of simplicity, we rename the variables so that:

$$\Phi_{\delta 1} = I_6 \tag{B.1}$$

$$\Phi_{\delta 2} = I_8 \tag{B.2}$$

$$\Phi_{\delta 3} = I_{10} \tag{B.3}$$

$$\Phi_{\delta 4} = I_{12} \tag{B.4}$$

$$\tag{B.5}$$

being 6 the edge corresponding to $\Phi_{\delta 1}$ and so on.

Having accepted this, table B.1 describes the complete netlist, where the typology could either be current generators I or resistance R.

B.3 TABLEAU ANALYSIS

We now write the tableau equation: $\mathbf{Tx} = \mathbf{s}$, that can be further expressed as:

$$\begin{bmatrix} \mathbf{A}_{n-1\times e} & 0_{n-1\times e} & 0_{n-1\times n-1} \\ 0_{e\times e} & -\mathbf{Id}_{e\times e} & \mathbf{A^T}_{e\times n-1} \\ \mathbf{R}_{e\times e} & \mathbf{G}_{e\times e} & 0_{e\times n-1} \end{bmatrix} \begin{bmatrix} \mathbf{i}_{e\times 1} \\ \mathbf{v}_{e\times 1} \\ \mathbf{p}_{n-1\times 1} \end{bmatrix} = \begin{bmatrix} 0_{n-1\times 1} \\ 0_{e\times 1} \\ \mathbf{s}_{e\times 1} \end{bmatrix} \tag{B.6}$$

Table B.1: Netlist of the equivalent circuit.

Edge	Node out	Node in	Type	Value
1	1	2	R	R_2
2	2	3	R	R_2
3	3	4	R	R_2
4	4	1	R	R_2
5	1	5	R	R_1
6	5	1	I	I_6
7	2	5	R	R_1
8	5	2	I	I_8
9	3	5	R	R_1
10	5	3	I	I_{10}
11	4	5	R	R_1
12	5	4	I	I_{12}

Note that the first line represents the KCL for the linear independent $n-1$ nodes, the second the KVL for e edges, and the third represents the topological equation $Ri + Gv = 0$ where the conductance approach is adopted (i.e. $1i_k - G_k v_k = 0$ instead of $R_k i_k - 1v_k = 0$).

Therefore, all legit equations are applied and further equations such as the KCL at node 5 are simply a linear combination of the other independent ones.

B.4 AT-THE-LIMIT SOLUTION

By solving (B.6) (e.g by using matrix inversion), the complete set of solutions is obtained. It is not reported here due to its long expression.

Computing the limit, $\mathbf{s}_\infty$ can be derived. Limiting the solution to the first four currents (i.e. Φ_k, $k = 1, 2, 3, 4.$), we can write in matrix form:

$$\begin{bmatrix} i_1 \\ i_2 \\ i_3 \\ i_4 \end{bmatrix} = \begin{bmatrix} -\frac{3}{8} & -\frac{1}{8} & \frac{1}{8} & \frac{3}{8} \\ \frac{3}{8} & -\frac{3}{8} & -\frac{1}{8} & \frac{1}{8} \\ \frac{1}{8} & \frac{3}{8} & -\frac{3}{8} & -\frac{1}{8} \\ -\frac{1}{8} & \frac{1}{8} & \frac{3}{8} & -\frac{3}{8} \end{bmatrix} \begin{bmatrix} I_6 \\ I_8 \\ I_{10} \\ I_{12} \end{bmatrix} \tag{B.7}$$

This matrix cannot be inverted, but the aimed relation is found.

This dissertation has been carried out for $Q_s = 4$ but it can be generalised for any number of stator slots.

We could further say that $I_{12} = -I_6 - I_8 - I_{10}$ and then we could rewrite the matrix of (B.7) by legitimately subtracting at each element the last element belonging to the same row. We then obtain:

$$\begin{bmatrix} i_1 \\ i_2 \\ i_3 \\ i_4 \end{bmatrix} = \begin{bmatrix} -\frac{3}{4} & -\frac{1}{2} & -\frac{1}{4} \\ \frac{1}{4} & -\frac{1}{2} & -\frac{1}{4} \\ \frac{1}{4} & \frac{1}{2} & -\frac{1}{4} \\ \frac{1}{4} & \frac{1}{2} & \frac{3}{4} \end{bmatrix} \begin{bmatrix} I_6 \\ I_8 \\ I_{10} \end{bmatrix} \tag{B.8}$$

We also know that $i_1 + i_2 + i_3 + i_4 = 0$ which follows that, by calling A the matrix in (B.8) and $a_{i,j}$ its component:

$$a_{4,k} = -a_{1,k} - a_{2,k} - a_{3,k} \text{ for } k = 1, 2, 3 \tag{B.9}$$

that can be readily verified.

We now reduce the matrix in a 3×3 equivalent one by neglecting the last equation, although i_4 is a linear combination of i_1, i_2, i_3, and each of these quantities is a linear combination of I_6, I_8, I_{10} so ultimately it is possible to write i_4 as a linear combination of the input currents/fluxes, which is - in fact - the fourth row. Replacing then the fictitious currents with the magnetic fluxes, we can write:

$$\begin{bmatrix} \Phi_1 \\ \Phi_2 \\ \Phi_3 \end{bmatrix} = \begin{bmatrix} -\frac{3}{4} & -\frac{1}{2} & -\frac{1}{4} \\ \frac{1}{4} & -\frac{1}{2} & -\frac{1}{4} \\ \frac{1}{4} & \frac{1}{2} & -\frac{1}{4} \end{bmatrix} \begin{bmatrix} \Phi_{\delta 1} \\ \Phi_{\delta 2} \\ \Phi_{\delta 3} \end{bmatrix} \tag{B.10}$$

where Φ_4 can be easily derived from $\Phi_4 = -\Phi_1 - \Phi_2 - \Phi_3$, and the set of air-gap fluxes inputs is now generic and not bound by any condition.

Ultimately, such reduced matrix can be inverted, and we obtain:

$$\begin{bmatrix} -\frac{3}{4} & -\frac{1}{2} & -\frac{1}{4} \\ \frac{1}{4} & -\frac{1}{2} & -\frac{1}{4} \\ \frac{1}{4} & \frac{1}{2} & -\frac{1}{4} \end{bmatrix}^{-1} = \begin{bmatrix} -1 & 1 & 0 \\ 0 & -1 & 1 \\ -1 & -1 & -2 \end{bmatrix} \tag{B.11}$$

so that:

$$\begin{bmatrix} \Phi_{\delta 1} \\ \Phi_{\delta 2} \\ \Phi_{\delta 3} \end{bmatrix} = \begin{bmatrix} -1 & 1 & 0 \\ 0 & -1 & 1 \\ -1 & -1 & -2 \end{bmatrix} \begin{bmatrix} \Phi_1 \\ \Phi_2 \\ \Phi_3 \end{bmatrix} \tag{B.12}$$

Recalling (B.9), we can further state that:

$$\begin{bmatrix} \Phi_{\delta 1} \\ \Phi_{\delta 2} \\ \Phi_{\delta 3} \\ \Phi_{\delta 4} \end{bmatrix} = \begin{bmatrix} -1 & 1 & 0 \\ 0 & -1 & 1 \\ -1 & -1 & -2 \\ 2 & 1 & 1 \end{bmatrix} \begin{bmatrix} \Phi_1 \\ \Phi_2 \\ \phi_3 \end{bmatrix} \tag{B.13}$$

Matrix in (B.13) will be later developed, discussed and compared.

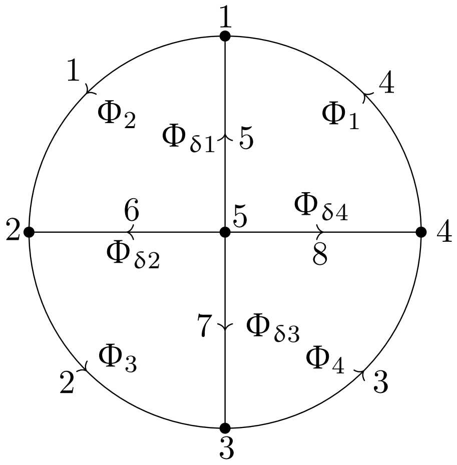

Figure B.2: Equivalent simplified circuit graph for $Q_s = 4$.

B.5 GRAPH-THEORY-BASED APPROACH

B.5.1 *Equivalent simplified circuit graph*

Consider fig. B.2. It represents the schematic graph of the equivalent magnetic circuit of fig. B.1 and that is described in the previous section.

In this reasoning, the *incidence matrix* $\mathbf{A}$ of a *directed graph* is defined as a $n \times e$ matrix - where n is the number of nodes of the graph and e its number of edges - that has for each column a $+1$ in the row corresponding to the node from which that edge is going outward, and a -1 in the terminal vertex of the edge.

For the circuit in fig. B.2 we get that:

$$\mathbf{A}_{5\times 8} = \begin{bmatrix} 1 & 0 & 0 & -1 & -1 & 0 & 0 & 0 \\ -1 & 1 & 0 & 0 & 0 & -1 & 0 & 0 \\ 0 & -1 & 1 & 0 & 0 & 0 & -1 & 0 \\ 0 & 0 & -1 & 1 & 0 & 0 & 0 & -1 \\ 0 & 0 & 0 & 0 & 1 & 1 & 1 & 1 \end{bmatrix} \tag{B.14}$$

Defining $\mathbf{i} \triangleq [i_1, i_2, i_3, i_4, i_5, i_6, i_7, i_8]^T$ as the array of currents in each edge, we can readily write the KCL in matrix form taking advantage of the incidence matrix:

$$\mathbf{A}_{n\times e}\mathbf{i}_{e\times 1} = 0_{e\times 1} \tag{B.15}$$

which can be expansed as:

$$\begin{cases} i_2 - i_1 - i_5 = 0 \\ -i_2 + i_3 - i_6 = 0 \\ -i_3 + i_4 - i_7 = 0 \\ -i_4 + i_1 - i_8 = 0 \\ i_5 + i_6 + i_7 + i_8 = 0 \end{cases} \tag{B.16}$$

From circuit theory, it is known that only $n-1$ KCL are linearly independent, which means the *reduced incidence matrix* has to be considered from now on. This matrix is simply $\mathbf{A}_{n \times e}$ erasing one row, and it can be denoted as $\mathbf{A}_{n-1 \times e}$. We decide erase the last row, that is a condition on the sum of magnetic fluxes in the air-gap, i.e. (5.4).

Therefore, by using the reduced incidence matrix, we can easily write (B.16) without the last row, and that can be rearranged[1] as:

$$\begin{bmatrix} -1 & 1 & 0 & 0 \\ 0 & -1 & 1 & 0 \\ 0 & 0 & -1 & 1 \\ 1 & 0 & 0 & -1 \end{bmatrix} \begin{bmatrix} i_1 \\ i_2 \\ i_3 \\ i_4 \end{bmatrix} = \begin{bmatrix} i_5 \\ i_6 \\ i_7 \\ i_8 \end{bmatrix} \tag{B.17}$$

This resulting matrix is not invertible. Nevertheless, we already found an expression that gives $[i_1, i_2, i_3, i_4]^T$ as a linear combination of $[i_5, i_6, i_7, i_8]^T$. By noticing that, in (B.7), $[I_6, I_8, I_{10}, I_{12}]^T$ is exactly what we called $[i_5, i_6, i_7, i_8]^T$, we can write:

$$\begin{bmatrix} i_1 \\ i_2 \\ i_3 \\ i_4 \end{bmatrix} = \begin{bmatrix} -\frac{3}{8} & -\frac{1}{8} & \frac{1}{8} & \frac{3}{8} \\ \frac{3}{8} & -\frac{3}{8} & -\frac{1}{8} & \frac{1}{8} \\ \frac{1}{8} & \frac{3}{8} & -\frac{3}{8} & -\frac{1}{8} \\ -\frac{1}{8} & \frac{1}{8} & \frac{3}{8} & -\frac{3}{8} \end{bmatrix} \begin{bmatrix} i_5 \\ i_6 \\ i_7 \\ i_8 \end{bmatrix} \tag{B.18}$$

or, by replacing fictitious currents with the actual fluxes, as:

$$\begin{bmatrix} \Phi_1 \\ \Phi_2 \\ \Phi_3 \\ \Phi_4 \end{bmatrix} = \begin{bmatrix} -\frac{3}{8} & -\frac{1}{8} & \frac{1}{8} & \frac{3}{8} \\ \frac{3}{8} & -\frac{3}{8} & -\frac{1}{8} & \frac{1}{8} \\ \frac{1}{8} & \frac{3}{8} & -\frac{3}{8} & -\frac{1}{8} \\ -\frac{1}{8} & \frac{1}{8} & \frac{3}{8} & -\frac{3}{8} \end{bmatrix} \begin{bmatrix} \Phi_{\delta,1} \\ \Phi_{\delta,2} \\ \Phi_{\delta,3} \\ \Phi_{\delta,4} \end{bmatrix} \tag{B.19}$$

Now recall (B.13) and compare it to (B.17), which can be rewritten as:

$$\begin{bmatrix} -1 & 1 & 0 & 0 \\ 0 & -1 & 1 & 0 \\ 0 & 0 & -1 & 1 \\ 1 & 0 & 0 & -1 \end{bmatrix} \begin{bmatrix} \Phi_1 \\ \Phi_2 \\ \Phi_3 \\ \Phi_4 \end{bmatrix} = \begin{bmatrix} \Phi_{\delta,1} \\ \Phi_{\delta,2} \\ \Phi_{\delta,3} \\ \Phi_{\delta,4} \end{bmatrix} \tag{B.20}$$

---

[1] Note that it is simply another manner of expressing the KCL.

Be noticing that $\Phi_{\delta,4} = -\Phi_{\delta,1} - \Phi_{\delta,2} - \Phi_{\delta,3}$, it is straightforward to prove they lead to the same equations, in fact, both methods are equivalent. The mathematical connection between (B.17) and (B.19) is investigated in the next section.

B.6 THE PSEUDO-INVERSE

Considering now only the magnetic equivalent model, we write (B.17), or (B.20) as $\mathbf{M\Phi} = \mathbf{\Phi}_\delta$ and (B.19) as $\mathbf{\Phi} = \mathbf{N\Phi}_\delta$.

There are two other condition embedded, that is:

- The sum of magnetic fluxes in each portion of yoke is zero, which comes from the Hopkinson's Law $n_s \sum_{j=1}^{Q_s} i_{s,j} = R \sum_{j=1}^{Q_s} \Psi_{s,j}$ where it is assumed the core reluctance R not to be identically zero. This means $\sum_{j=1}^{Q_s} \Phi_{s,j} = 0$.
- The sum of air-gap fluxes is zero because of Gauss'Law, i.e. $\sum_{j=1}^{Q_s} \Phi_{\delta,j} = 0$.

Equation $\mathbf{M\Phi} = \mathbf{\Phi}_\delta$ can be expressed as $\mathbf{Ax} = \mathbf{b}$ following classical linear algebra theory. Rouché–Capelli theorem states that a system of linear equations with n variables has a solution if and only if the rank of its coefficient matrix $\mathbf{A}$ is equal to the rank of its augmented matrix $\mathbf{A}|\mathbf{b}$. In our case, this happens only because of the second embedded condition, which is always true, and which allows to conclude that (B.17) has a solution of dimension $n - \text{rank}(\mathbf{A})$, which in our case corresponds to a dimension 1. So far, second embedded condition has been used.

By recalling the first embedded condition, it is possible to reduce the dimension of the system. In fact, such condition can be expressed - by row-echelon reducing the matrix and recalling $\Phi_{s,4} = -\Phi_{s,1} - \Phi_{s,2} - \Phi_{s,3}$ - as:

$$\begin{bmatrix} 2 & 1 & 1 \\ 1 & 2 & 1 \\ 1 & 1 & 2 \end{bmatrix} \begin{bmatrix} \Phi_1 \\ \Phi_2 \\ \Phi_3 \end{bmatrix} = - \begin{bmatrix} \Phi_{\delta,1} \\ \Phi_{\delta,2} \\ \Phi_{\delta,3} \end{bmatrix} \begin{bmatrix} 1 & 1 & 1 \\ 0 & 1 & 1 \\ 0 & 0 & 1 \end{bmatrix} \tag{B.21}$$

which, solved by matrix inversion and multiplication, is the same expression found in (B.10).

It is interesting to see if there is a way to easily pass from (B.20) as $\mathbf{M\Phi} = \mathbf{\Phi}_\delta$ to (B.19) as $\mathbf{\Phi} = \mathbf{N\Phi}_\delta$. It can be proved that $\mathbf{M}$ is the Moore-Penrose inverse or pseudo-inverse of $\mathbf{N}$.

Consider the following linear-algebra theorem: [22–24]:

Theorem B.6.1. *The complete set of solutions to* $\mathbf{Ax} = \mathbf{b}$ *is given by* $\mathbf{z} = \mathbf{A}^\dagger\mathbf{b} + \left(\mathbf{I} - \mathbf{A}^\dagger\mathbf{A}\right)\mathbf{w}$ *as* $\mathbf{w}$, *an arbitrary n-dimensional vector, varies over all possible values.*

where $\mathbf{A}$ is an $m \times n$ matrix of coefficients, $\mathbf{b}$ is an w-dimensional vector of constants and $\mathbf{x}$ is a n-dimensional vector of unknowns, $\mathbf{A}^\dagger$ is the Moore-Penrose inverse or pseudo-inverse or generalised inverse of $\mathbf{A}$, $\mathbf{I}$ is the identity matrix.

In our specific case, it can be proved that the condition imposing zero-sum of yoke fluxes $\sum_{j=1}^{Q_s} \Phi_{s,j} = 0$ provokes that $\mathbf{w}$ must result in a zero-sum vector, and therefore $\left(\mathbf{I} - \mathbf{A}^\dagger \mathbf{A}\right) \mathbf{w}$ is zero.

As a consequence, the complete set of equations to $\mathbf{A}\mathbf{x} = \mathbf{b}$ is given by $\mathbf{z} = \mathbf{A}^\dagger \mathbf{b}$.

RIASSUNTO IN LINGUA ITALIANA

Lo scopo di questo lavoro è derivare due modelli per lo studio del transitorio di un motore a induzione multifase WICSC (Wound Independently-Controlled Stator Coils) ad avvolgimenti "Gramme type winding" basato sul brevetto tedesco di motore ISCAD (Intelligent Stator Cage Drive), da cui il motore WICSC si discosta per operatività in un range di tensione maggiore a favore di correnti nominali inferiori. Questo motore, sviluppato nel Dipartimento di *Electrical Machines and Drives* del KTH - Royal Institute of Technology, Stoccolma (Svezia) ha il fine di costituire un prototipo di ricerca circa le potenzialità di operare il cambio dinamico di fase e poli in termini di miglioramento delle performance.

Il primo modello, denominato "analitico", si basa sull'analisi di natura elettromagnetica e matematico/algebrica del problema, mentre il secondo, definito "numerico-analitico FE (Finite Element)" si concentra sull'estrazione di informazioni concentrate dall'analisi agli elementi finiti del motore in oggetto. Entrambi dunque puntano sull'estrazione di parametri con cui definire un sistema di equazioni differenziali atto a descrivere il comportamento elettrico della macchina.

In primo luogo, entrambi i modelli vengono derivati e si evidenzia come ciascun singolo parametro sia ottenuto. In secondo luogo, ciascun elemento viene validato per mezzo di simulazioni indipendenti agli elementi finiti; tale verifica investiga la bontà di predire grandezze magnetiche e tensioni. Complessivamente, si dimostra che i risultati possono essere considerati buoni, specialmente per il modello di natura numerico-analitico FE. Terzo e ultimo stadio è quello di comparare la risoluzione delle equazioni elettriche e giudicare la capacità dei modelli di predire le correnti elettriche e la coppia meccanica. In questo livello, si mostrano diverse configurazioni di poli e fasi, e si analizza infine il transitorio durante il cambio di numero di poli.

Per quanto concerne queste simulazioni, in merito alle correnti si osserva che i modelli riescono a predire i risultati agli elementi finiti, specie nell'andamento a bassa frequenza e con più accuratezza dopo l'estinzione del transitorio, mentre vi sono differenze più marcate riguardo i valori di coppia meccanica. Nel suo complesso, entrambi i modelli possono essere utili nel simulare il comportamento della macchine al fine di progettare il controllo di corrente e velocità.

BIBLIOGRAPHY

[1] Katherine Brown. *NASA, NOAA to Announce 2019 Global Temperatures, Climate Conditions*. und. Text. Jan. 2020. URL: `http://www.nasa.gov/press-release/nasa-noaa-to-announce-2019-global-temperatures-climate-conditions` (visited on 02/26/2020).

[2] Katherine Brown. *NASA, NOAA Analyses Reveal 2019 Second Warmest Year on Record*. und. Text. Jan. 2020. URL: `http://www.nasa.gov/press-release/nasa-noaa-analyses-reveal-2019-second-warmest-year-on-record` (visited on 02/26/2020).

[3] R. N Colvile, E. J Hutchinson, J. S Mindell, and R. F Warren. "The transport sector as a source of air pollution." In: *Atmospheric Environment* 35.9 (Mar. 2001), pp. 1537–1565. ISSN: 1352-2310. DOI: `10.1016/S1352-2310(00)00551-3`. URL: `http://www.sciencedirect.com/science/article/pii/S1352231000005513`.

[4] Konstantina Bitsi, Oskar Wallmark, and Sjoerd Bosga. "An Induction Machine with Wound Independently-Controlled Stator Coils." In: *2019 22nd International Conference on Electrical Machines and Systems (ICEMS)*. IEEE, 2019, pp. 1–5.

[5] Vitor Monteiro, Jose Afonso, Joao Ferreira, and Joao Afonso. "Vehicle Electrification: New Challenges and Opportunities for Smart Grids." en. In: *Energies* 12.1 (Dec. 2018), p. 118. ISSN: 1996-1073. DOI: `10.3390/en12010118`. URL: `http://www.mdpi.com/1996-1073/12/1/118` (visited on 02/26/2020).

[6] C. P. Gor, V. A. Shah, and M. P. Gor. "Electric vehicle drive selection related issues." In: *2016 International Conference on Signal Processing, Communication, Power and Embedded System (SCOPES)*. Oct. 2016, pp. 74–79. DOI: `10.1109/SCOPES.2016.7955554`.

[7] Nicola Bianchi, Silverio Bolognani, Enrico Carraro, Mose Castiello, and Emanuele Fornasiero. "Electric Vehicle Traction Based on Synchronous Reluctance Motors." In: *IEEE Transactions on Industry Applications* 52.6 (Nov. 2016), pp. 4762–4769. ISSN: 0093-9994, 1939-9367. DOI: `10.1109/TIA.2016.2599850`. URL: `http://ieeexplore.ieee.org/document/7542569/` (visited on 02/26/2020).

[8] Wally Rippel. *Induction Versus DC Brushless Motors*. sv-SE. Jan. 2007. URL: `https://www.tesla.com/sv_SE/blog/induction-versus-dc-brushless-motors` (visited on 02/26/2020).

[9] E. Levi, R. Bojoi, F. Profumo, H. A. Toliyat, and S. Williamson. "Multiphase induction motor drives - a technology status review." In: *IET Electric Power Applications* 1.4 (July 2007), pp. 489–516. ISSN: 1751-8679. DOI: `10.1049/iet-epa:20060342`.

[10] G. K Singh. “Multi-phase induction machine drive research—a survey.” In: *Electric Power Systems Research* 61.2 (Mar. 2002), pp. 139–147. ISSN: 0378-7796. DOI: `10.1016/S0378-7796(02)00007-X`. URL: `http://www.sciencedirect.com/science/article/pii/S037877960200007X`.

[11] K. Wang, Z. Q. Zhu, and G. Ombach. “Torque Improvement of Five-Phase Surface-Mounted Permanent Magnet Machine Using Third-Order Harmonic.” In: *IEEE Transactions on Energy Conversion* 29.3 (Sept. 2014), pp. 735–747. ISSN: 1558-0059. DOI: `10.1109/TEC.2014.2326521`.

[12] Stephan Runde, Andreas Baumgardt, Oleg Moros, Benjamin Rubey, and Dieter Gerling. “ISCAD - Design, Control and Car Integration of a 48 Volt High Performance Drive.” In: *China Electrotechnical Society Transactions on Electrical Machines and Systems* 3.2 (June 2019), pp. 117–123. ISSN: 20963564. DOI: `10.30941/CESTEMS.2019.00017`. URL: `http://www.cestems.org/uploads/20190625/15614290954126.pdf` (visited on 02/28/2020).

[13] Gurakuq Dajaku and Dieter Gerling. “Low costs and high efficiency asynchronous machine with stator cage winding.” In: *2014 IEEE International Electric Vehicle Conference (IEVC)*. IEEE, 2014, pp. 1–6.

[14] Florian Bachheibl and Dieter Gerling. “High-current, low-voltage power net.” In: *2014 IEEE International Electric Vehicle Conference (IEVC)*. IEEE, 2014, pp. 1–6.

[15] T. A. Lipo. *Introduction to AC machine design*. IEEE Press series on power engineering. OCLC: on1011688030. Hoboken, New Jersey: IEEE Press/Wiley, 2017. ISBN: 978-1-119-35216-7.

[16] Oskar Wallmark. *AC Machine Analysis - Fundamental Theory*. 2019.

[17] H. S Carslaw. *Introduction to the theory of Fourier’s series and integrals*. English. OCLC: 1706901. New York: Dover Publications, 1930. ISBN: 978-0-486-60048-2.

[18] Esam M. A. Hussein. “9 - Preprocessing of Measurements.” en. In: *Computed Radiation Imaging*. Ed. by Esam M. A. Hussein. London: Elsevier, Jan. 2011, pp. 97–123. ISBN: 978-0-12-387777-2. DOI: `10.1016/B978-0-12-387777-2.00009-4`. URL: `http://www.sciencedirect.com/science/article/pii/B9780123877772000094`.

[19] Katz Itamar. *Gaussian Filter on a vector in Matlab*. 2011. URL: `https://stackoverflow.com/questions/6992213/gaussian-filter-on-a-vector-in-matlab` (visited on 02/26/2020).

[20] István Faragó. “Convergence and stability constant of the theta-method.” In: *Applications of Mathematics 2013* (2013), pp. 42–51.

[21] Antero Arkkio. *Analysis of induction motors based on the numerical solution of the magnetic field and circuit equations*. en. Helsinki University of Technology, Dec. 1987. ISBN: 978-951-22-6076-8. URL: https://aaltodoc.aalto.fi:443/handle/123456789/2158 (visited on 02/06/2020).

[22] R. B. Bapat. “Moore-penrose inverse of the incidence matrix of a tree.” In: *Linear and Multilinear Algebra* 42.2 (Jan. 1997). Publisher: Taylor & Francis _eprint: https://doi.org/10.1080/03081089708818496, pp. 159–167. ISSN: 0308-1087. DOI: 10.1080/03081089708818496. URL: https://doi.org/10.1080/03081089708818496 (visited on 03/16/2020).

[23] M. James. “The generalised inverse.” en. In: *The Mathematical Gazette* 62.420 (June 1978). Publisher: Cambridge University Press, pp. 109–114. ISSN: 0025-5572, 2056-6328. DOI: 10.1017/S0025557200086460. URL: https://www.cambridge.org/core/journals/mathematical-gazette/article/generalised-inverse/8B58A1EC63AD8C38BE2AB74A5175028F (visited on 03/16/2020).

[24] Edward T. Wong. “2. Generalised inverses as linear transformations.” en. In: *The Mathematical Gazette* 63.425 (Oct. 1979). Publisher: Cambridge University Press, pp. 176–181. ISSN: 0025-5572, 2056-6328. DOI: 10.2307/3617889. URL: https://www.cambridge.org/core/journals/mathematical-gazette/article/2-generalised-inverses-as-linear-transformations/F9E88819B070EA1BA326A92F2F7B91DE (visited on 03/16/2020).